A STUDY OF PICOSECOND, HIGH-VOLTAGE PHOTOCONDUCTIVE SWITCHING USING ELECTRO-OPTIC DIAGNOSTICS AND COMPUTER-AIDED ANALYSIS

by

Lawrence Eric Kingsley

Submitted in Partial Fulfillment
of the
Requirements for the Degree

DOCTOR OF PHILOSOPHY

Supervised by
Prof. Adrian C. Melissinos
Dr. William R. Donaldson
Department of Physics and Astronomy
Laboratory for Laser Energetics

University of Rochester
Rochester, New York

1991

For my father, Karl

I wish he had lived to see it.

CURRICULUM VITAE

Lawrence Eric Kingsley is a native of Rochester, New York. He graduated in 1978 from Greece Arcadia High School with a New York State Regents Diploma. From 1979 to 1983, he attended Clarkson College of Technology in Potsdam, New York and was granted the B.S. with Great Distinction. His degree was in physics. In the fall of 1983, he entered the Ph.D. program in the Department of Physics and Astronomy at the University of Rochester. For the first two years of graduate study he held a teaching fellowship with the Department of Physics and Astronomy, receiving his M.A. in 1985. Since that time, he has been a fellow of the Laboratory for Laser Energetics, where he has performed his Ph.D. thesis research under the supervision of Dr. A.C. Melissinos and Dr. W.R. Donaldson.

ACKNOWLEDGMENTS

The author acknowledges the deep debt of gratitude owed to Dr. William Donaldson and Dr. Adrian Melissinos for supervising his research and teaching him how to be a scientist. He apologizes for all the headaches he has given them. He would also like to thank Dr. Gerard Mourou for his support and advice, and Dr. H. Gove, Dr. Y. Gao, and Dr. D. Meyerhofer for serving on his advisory committee.

The author received assistance from innumerable people in performing his research and preparing this dissertation and would particularily like to thank: Mrs. Betty Cook, Ms. Rose Peet, and Ms. Jean Steve, for indispensible logistic support; Ms. Ladonna Black, Ms. Antonia Sweet, Ms. Diane Hixson, and Ms. Millie Grassi for assistance in preparing the manuscript illustrations; and Mr. Pierre Bassaras, for his major role in the design, construction, and characterization of the coaxial silicon switch. He would also like take this oppurtunity to thank his colleagues, Mr. Charles Bamber, Dr. Steven H. Batha, Mr. David Brown, and Dr. Eric Lincke, for their help and advice, both professional and personal. Of course, none of this would have been possible without the love and support of the author's wife, Alison.

Gallium Arsenide samples were provided by G. Loubriel at Sandia National Laboratory and M. Weiner, A. Kim, and R. Zeto at the U.S. Army Electronics Technology and Device Laboratory.

This work was supported by the SDIO/IST through the Office of Naval Research under contract N00014-86-K-0583, by the United States Air Force Office of Scientific Research under contracts AFOSR-84-017S and AFSOR-87-0328, and by the Laser Fusion Feasibility Project at the Laboratory for Laser Energetics.

ABSTRACT

This dissertation documents advances in the field of ultrafast, high-voltage, semiconductor photoconductive switching. New developments in experimental diagnostics and theoretical device simulation are presented.

The output waveform of a laser-activated silicon photoconductive switch in a coaxial circuit was measured for bias voltages up to 20 kV. The switch was activated with a ~150 ps laser pulse. The waveform was characterized on a nanosecond timescale with capacitive probes. Electro-optic sampling, which utilizes the Pockels effect to probe electric fields, was used to measure the switched voltage rise time on a multipicosecond timescale. Rise time degradation with decreasing applied optical energy, variation of switching risetime and efficiency with applied bias voltage, and voltage overshoot were observed.

A unique, two-dimensional, electro-optic imaging system was used to investigate the dynamic behavior of the electric field in both bulk and planar high-voltage GaAs photoconductive switches during switch operation. The electro-optic imaging system is capable of producing two-dimensional maps of the surface field between the electrodes of a semiconductor device with temporal resolution of ~150 ps and spatial resolution of ~3 μm. The bulk switches were illuminated through their opposing mesh electrodes, and electric field profiles were obtained for different illumination schemes at different bias voltages up to 10 kV. Switching speed and efficiency were seen to depend on illumination configuration and applied bias voltage. The surface electric field above the planar GaAs switches was monitored while the switches were in lock-on mode, whereby a switch under high voltage bias remains conductive for a time inconsistant with the normal carrier recombination

time. In the lock-on mode, high-field domains were seen to form at the switch cathode. Evidence for current channeling and field oscillation was also obtained. The GaAs switch field profiles are in contrast to Si switch field profiles which display the expected behavior.

A computer-assisted model cabable of simulating realistic high-voltage photoconductive switches was developed. The model is based on the numerical solution of the semiconductor drift-diffusion equations with the appropriate boundary conditions to represent a high-speed photoconductor in an external circuit. High-field effects such as non-linear carrier mobility are included in the model. Observed switch behavior is in partial agreement with simulation.

TABLE OF CONTENTS

DEDICATION ii
CURRICULUM VITAE iii
ACKNOWLEDGMENTS iv
ABSTRACT v
TABLE OF CONTENTS vii
LIST OF TABLES x
LIST OF FIGURES xi

CHAPTER 1. INTRODUCTION 1
I. MOTIVATION 1
II. PHOTOCONDUCTIVE SWITCH OPERATION AND DESIGN 5
1. BASIC OPERATIONAL PRINCIPLES 6
A. Photoexcitation 6
B. Recombination 10
C. Switch Resistance and Carrier Mobility 11
2. PRACTICAL PHOTOCONDUCTIVE SWITCHES 19
A. Material Requirements 19
B. Contact Requirements 20
C. External Circuit 21
D. Switch Breakdown 24
E. Optical Pulse Requirements 25
F. Switch Diagnostics 27
CHAPTER 1. REFERENCES 31

CHAPTER 2. CHARACTERIZING THE OPERATION OF A COAXIAL SILICON SWITCH 35
I. SWITCHING CIRCUIT 35
1. HIGH VOLTAGE PULSER 35
2. TRANSMISSION LINE & ASSOCIATED COMPONENTS 37

3. CAPACITIVE PROBES 40
A. Design 40
B. Switching Data and Analysis 45
II. ELECTRO-OPTIC SAMPLING 48
1. BASIC PRINCIPLES OF ELECTRO-OPTIC SAMPLING..... 48
A. Physical Origin 48
B. Electro-Optic Field Measurement 52
2. ELECTRO-OPTIC RISE TIME MEASUREMENT 58
A. Experimental Arrangement 58
B. Experimental Results and Discussion 60
CHAPTER 2. REFERENCES 67

CHAPTER 3. TWO-DIMENSIONAL IMAGING SYSTEM 69
I. EARLY WORK: STATIC 2-D AND DYNAMIC 1-D IMAGING..... 70
1. STATIC 2-D IMAGING SYSTEM AND SELECTED RESULTS 70
2. DYNAMIC 1-D IMAGING SYSTEM AND RESULTS..... 72
3. ANALYSIS OF EARLY EXPERIMENTS 76
II. 2-D ELECTRO-OPTIC SAMPLING 82
1. SYSTEM 82
2. IMAGING OF PHOTOCONDUCTIVITY IN SILICON 92
CHAPTER 3. REFERENCES 99

CHAPTER 4. ELECTRO-OPTIC IMAGING OF HIGH-FIELD PHOTOCONDUCTIVITY IN GaAs 100
I. BULK SWITCH OPERATION 100
1. IMAGING DATA 100
2. DISCUSSION OF BULK SWITCH DATA 110
II. PLANAR SWITCH STUDY 115
1. MOTIVATION 115
2. PLANAR SWITCH DATA AND DISCUSSION 118
CHAPTER 4. REFERENCES 126

CHAPTER 5. COMPUTER-AIDED ANALYSIS OF PHOTOCONDUCTIVE SWITCHING 128
I. MODEL FORMULATION 128
1. SEMICONDUCTOR DEVICE EQUATIONS 130
A. Maxwell's Equations 130
C. Carrier Continuity Relations 133
2. MODEL EQUATIONS 134
A. Carrier Generation Functions 137
B. Reduction Function 41
C. Carrier Mobility 141
3. BOUNDARY AND INITIAL VALUES 141
A. Carrier Densities 144
B. Electric Potential 144
II. NUMERICAL SOLUTION METHOD 147
III. COMPUTATIONAL RESULTS 148
1. GALLIUM ARSENIDE SWITCHING 149
A. Coplanar Switches 149
B. Bulk Switches 156
2. SILICON SWITCHES 159
CHAPTER 5. REFERENCES 163

CHAPTER 6. SUMMARY 165

APPENDIX A. LASER SYSTEM 167
APPENDIX A. REFERENCES 173

LIST OF TABLES

Table	Title	Page
1.1	Physical Properties of Si and GaAs	14
2.1	Si Switch Electro-Optic Risetime Measurement Results	63
5.1	One-Dimensional Drift-Diffusion Equations	135
5.2	Model Impact Ionization Parameters	139
5.3	Model Mobility Functions	142

LIST OF FIGURES

Figure	Caption	Page
Fig.1.1	Generic semiconductor photoconductor in a circuit. The semiconductor is connected to the circuit through metallic contacts. V is the bias voltage..The source impedance is Z_s. The load impedance is Z_L. Switch dimensions l, w, and d range from microns to centimeters depending on application.	2
Fig.1.2	Observation of nanosecond and picosecond photoconductivity in Cr:GaAs in 1972 by Jayarman and Lee. (a) Oscilliscope trace of Q-switched nanosecond laser pulse (upper trace) and corresponding photoconductivity, (b) Oscilliscope trace of picosecond mode-locked laser pulse train, (c) Picosecond photoconductivity excited by laser pulse train shown in (b). (after ref.[1])	4
Fig.1.3	The process of photogeneration showing intrinsic (band-to-band), extrinsic (trap assisted), and two-photon photoexcitation. The incident photon energy is hν. E_c is the conduction band energy. E_v is the valence band energy. (after ref.[17])	8
Fig.1.4	Optically excited transitions in a photoconductor: (a) and (b) direct transitions; (c) indirect, phonon assisted transition. (after ref.[17])	8
Fig.1.5	Optical transmission data for Si and GaAs. Percent transmission is plotted versus wavelength for (a) Si and (b) GaAs. The sharp transmission cutoff at about 870 nm observed for GaAs, indicative of direct optical transitions, contrasts with the diffuse edge seen in the Si data.	9
Fig.1.6	Decay of electrical conductivity of a Si photoconductive switch after illumination by a 100 ps laser pulse. The conductivity was probed with an electrical pulse at various times after illumination. The voltage switched as a function of electrical pulse delay is plotted. τ was measured to be 73 μsec.	12

Fig.1.7	Measured value of the carrier drift velocity versus electric field for high purity Ge, Si, and GaAs. For Ge and Si, the carrier velocity increases linearly with electric field until the velocity saturates. In GaAs, carrier velocity increases linearly with field until about 3.2 kV/cm and then decreases with increasing field.	17
Fig.1.8	Three different geometries for photoconductive switches. (a) Coaxial geometry where the semiconductor element has replaced a portion of the center conductor, (b) stripline geometry where the switch bridges a gap in a stripline on a dielectric material, (c) stripline geometry where the stripline is directly on the semiconductor substrate. (after ref.[11])	23
Fig.1.9	Low-voltage switching in Si monitored directly across the load resitor. A ~200 ps, λ=1064 nm laser pulse was used to excite the switch (a) Analog oscilliscope trace of switched voltage pulse. The risetime is scope limited to 1 ns. (b) Tektronix sampling scope trace showing ~200 ps risetime. (c) Sampling scope trace of the output of a diode used to monitor the exciting laser pulse.	29
Fig.1.10	Photoconductive switching in Si monitored at the bias electrode with a capacitive probe. The switch was pulse-biased at -1 kV. When the switch is activated by the ~200 ps, 1064 nm laser pulse the bias pulse is switched to ground. Traces shown for (a) 50 ns/div, and (b) 500 ps/div.	30
Fig.2.1	Schematic of high-power switching circuit. (a) Entire circuit showing major circuit components. (b) Switchholder detail.	36
Fig.2.2	High-voltage thyratron bias pulser output voltage measured with internal resistive probe.	38
Fig.2.3	Equivalent switching circuit.	38
Fig.2.4	Switchholder mechanical detail showing switch, electrodes, connectors, and electro-optic sampling crystal.	41
Fig.2.5	Load termination detail. The overall length of the resistor housing is 1.5 ft. This drawing does not show capacitive probes.	42
Fig.2.6	Capacitive probe assembly sketch. The probe is a modified BNC connector.	42

Fig.2.7 Typical output pulse from the capacitive probe. The area under the trace is proportional to the signal voltage. 44

Fig.2.8 Capacitive probe calibration curves for the load probe for high voltage calibration. 44

Fig.2.9 Switched voltage waveforms at a constant bias of 12 kV for variuos optical energies measured with capacitive probe. (a) 25 μJ; (b) 75 μJ; (c) 150 μJ. The temporal resolution is ~1 ns. 46

Fig.2.10 Switched voltage waveforms at a constant optical energy of 150 μJ for various bias voltages measured with capacitive probe. (a) 1.1 kV; (b) 5.1 kV; (c) 12 kV. The temporal resolution is ~1 ns. 46

Fig.2.11 Propagation of an optical wave in a birefringent crystal. The index ellipsoid is shown. The cross section of the ellipse in the xy plane is a circle: the z-axis is the crystal axis. The optical wave propagates along the x-axis. The plane cross section in the zy plane is an ellipse: E_z and E_y will experience different indices of refraction, n_e (extraordinary index) and n_o (ordinary index) respectively. 50

Fig.2.12 a) Electric field, probe beam, and crystal alignment for producing electro-optic effect in $LiTaO_3$. This is called the transverse sampling geometry. b) The change in the indicatrix of the $LiTaO_3$ crystal induced by the applied electric field. 53

Fig.2.13 Set-up for electro-optically measuring an electric field. The electro-optic crystal is placed between two crossed polarizers. The applied electric field modulates the probe beam intensity measured at the detector. 53

Fig.2.14 Response of electro-optic intensity modulator to applied voltage. The curve is given by Eqs.(2.3) & (2.4). The curve is quasi-linear at $V_{\pi/2}$. The regions of 5% and 1% deviation from linear response are indicated. In these regions the intensity change is essentially proportional to the applied voltage. 56

Fig.2.15 Basic principles of electro-optic sampling. Optical pulse train repeatedly samples photogenerated electrical pulse train in electro-optic modulator. Optical and electrical pulses are in complete synchronization: there is no jitter. Optical delay can be inserted in either the pump or probe beam. 56

Fig.2.16	Entire switching and electro-optic sampling set-up in schematic	59
Fig.2.17	Modulation of optical probe pulse due to applied electric field. Oscilliscope trace of probe pulse measured with a diode detector is shown. Lower trace is pulse with bias voltage off; upper trace with bias voltage on. The applied voltage was ~4 kV.	61
Fig.2.18	Switched voltage waveforms measured electro-optically. Data taken for optical energies of 116, 67, and 45 μJ for bias voltages of a) 13 kV and b) 19 kV.	62
Fig.3.1	Arrangement of $LiTaO_3$ crystal in surface field above semiconductor surface.	71
Fig.3.2	Surface field probe utilizing pinpoint, cw electro-optic sampling.	71
Fig.3.3	Profile of electrically induced birefringence along center line between Al contact pads on Si measured using cw probe. The electric field calculated from the induced birefringence is also given.	73
Fig.3.4	Two dimensional map of electrically induced birefringence obtained by translating switch beneath sampling probe point.	73
Fig.3.5	Schematic of 1-D, dynamic electro-optic sampling system.	75
Fig.3.6	Time evolution of electric field profile above a Si switch after application of step function bias. The contact gap was 2 mm, the bias was 1 kV.	77
Fig.3.7	Variables and geometry for conformal mapping of electric field distribution of: a) parallel electrodes, to b) coplanar electrodes.	77
Fig.3.8	Field profile directly at surface obtained from conformal map.	79
Fig.3.9	Field profile after integrating over crystal thickness, perpendicular to electrode plane. Upper curve has been integrated over all field lines. Lower curve is result of integral over 1/2 field lines. Note loss of detail compared to Fig.3.8 as crystal becomes thicker.	79
Fig.3.10	Detail of electro-optic probe set-up to measure electric field above photoconductive switch of surface device type.	83

Fig.3.11 Detail of electro-optic probe set-up to measure electric field of GaAs bulk photoconductive switch. 84

Fig.3.12 Results of DC calibration of electro-optic imaging system showing least squares fit of the experimental transmission curve to Eq.(3.5) for one image pixel. 87

Fig.3.13 Transmission function for different pixels corresponding to various positions in the e-o crystal. The active region is the area between the electrodes Note the spatial variation in the e-o properties of the crystal, i.e. V_π is a function of sampled position. 87

Fig.3.14 The complete electro-optic imaging system. 89

Fig.3.15 Collapse of electric field above IR illuminated surface type Si switch. Lineouts from raw electro-optic images taken through center of switch perpendicular to contact edge for various times (0 ps is before IR pump pulse). The switch was biased at 5.8 kV across a 4 mm contact gap. Note the spatially uniform collapse of the field. This data was taken before the imaging system development was complete and lacks later improvements in system calibration. 93

Fig.3.16 Effect of non-uniform illumination on the electric field above Si surface type switch. Raw electro-optic images shown before and 1 ns after illumination by 40 μm spot of IR energy at switch center. Switch wasbiased at 3 kV across 3 mm contact gap. Note local collapse of electric field near switch center. 94

Fig.3.17 512 x 512 gray-scale images of the electric field above a Si photoconductive switch obtained with 2-D e-o imaging system. The electrodes were coplanar and the contact gap was 4 mm. Bias was 6 kV. High field is white, zero field is black. Image shown for a) before pump pulse, and b) 1650 ps after pump pulse. Note reduction in field strength following pump illumination. 96

Fig.3.18 Electric field profiles along a line perpendicular to the contact pads on Si switch obtained from images like those in Fig.3.17 by averaging all 512 pixels along a line parallel to the pads. Note uniform collapse of field from pre-pump to 1000 ps after pump. The field remains collapsed out to the limit of this measurment, 2000 ps after pump. 98

Fig.4.1 Bulk GaAs switch with mesh electrodes on opposite faces. The switch has been halved and a $LiTaO_3$ crystal is in place to measure the surface electric field between the contacts. The $LiTaO_3$ crystal has an anti-reflection (AR) coating for both 532 nm and 1064 nm light on the top surface. The bottom surface has a high-reflection (HR) coating for 532 nm and an AR coating for 1064 nm. 102

Fig.4.2 The electro-optic image of the surface electric field on a GaAs switch 800 ps after illumination by a 200 ps IR pulse through both of its electrodes. The left side of the image corresponds to negative high voltage electrode. The active area is 6 mm by 10 mm and the field enhancements are located behind the solid portion of the high voltage contact. 104

Fig.4.3 Temporal evolution of electric field above 6 mm thick bulk GaAs switch illuminated by 200 ps IR pulse through both contacts. Switch biased at 5 kV. Images processed and scaled to equivalent electrode voltage (EEV). The active area of the image is 6 mm by 1 cm. The collapse of electro-optic field proceeds from the essentially uniform profile shown in (a). 106

Fig.4.4 Same conditions as in Fig.4.3 except switch biased at 9 kV. The incomplete collapse of field is evidenced by ~5 kV/cm field remaining across switch after 1000 ps. 104

Fig.4.5 Temporal evolution of electric field above 6 mm thick bulk GaAs switch for different illumination conditions. Switch biased at 8 kV. Lineouts taken through center of processed electro-optic image at different times after illumination with 200 ps IR pulse. Greater efficiency and speed are obtained for illumination through both contacts. 108

Fig.4.6 The electro-optic efficiency for a 6 mm bulk GaAs photoconductive switch illuminated through both contacts as a function of time. The efficiency decreased with increasing field. 111

Fig.4.7 The electro-optic efficiency of a GaAs photoconductive switch illuminated through only the high voltage contact; (a) 3.8 mJ/cm^2 (b) 2.1 mJ/cm^2. 111

Fig.4.8 The load current versus bias voltage for various IR pump energies; (a) bias up to 5 kV; (b) bias up to 9 kV. 114

Fig.4.9 Switched output waveform of planar GaAs switch monitored at the load using current probe for (a) -2.5 kV bias, just at lock-on threshold; and (b) -3.0 kV, above lock-on threshold. 119

Fig.4.10 Average electric field above active area of planar switch as a function of time at -2.5 kV bias voltage, just below lock-on threshold for this sample. Each data point in this plot is an average over all pixels in the active region of the electro-optic field image. 121

Fig.4.11 Average field versus time , as in Fig.4.11, at bias of -6 kV, above lock-on threshold. 121

Fig.4.12 Electric field spatial profiles above planar switch along a line between the swictch contacts at different times during switch operation. This plot was obtained from the full electro-optic image by averaging over 100 pixels along a direction parallel to the contact edge. The switch bias was -2.5 kV (10 kV/cm). 0 ps is just before pump pulse arrival. Note field enhancement at contact edges at 0.0 cm and .25 cm. 123

Fig.4.13 Electric field profiles at different times, as in Fig.4.12, switch bias -6 kV (24 kV/cm). Note high-field domain extending from cathode. 123

Fig.4.14 Electro-optic images at different times during planar switch operation. The images have been processed so that white corresponds to field >16 kV/cm and black is < 16kV/cm. Time is relative to pump pulse arrival. The image progresses from complete switching in (a), to formation of high-field domain (b), to channels of low field (c). The contact layout is also shown, (d). 124

Fig.5.1 Photoconductive switch and external circuit as modeled in computer simulation. Model variables, parameters, and illumination schemes shown. 136

Fig.5.2 Plot of the impact ionization coefficient functions for Si and GaAs used in the switch simulation model. 140

Fig.5.3 Plot of electron drift velocitiy for GaAs and Si versus electric field using the mobilty expressions from the simulation model. 143

Fig.5.4	Calculated spatial profile of electric field in GaAs switch biased at -1 kV at different times during switch operation. The electric field displays uniform collapse and recovery at this bias voltage.	150
Fig.5.5	Electric field spatial profiles for GaAs switch: (a) calculated profile for -3 kV bias; (b) profile obtained with e-o imaging system for -2.5 kV bias.	151
Fig.5.6	GaAs switch electric field spatial profiles for -6 kV bias: (a) calculated profile ; (b) measured profile. Note the high field region near the cathode in both (a) and (b).	152
Fig.5.7	Calculated Electric field profile at -6 kV bias as in Fig.5.6(a) with emphasis on early collapse of field. Note the field collapses most rapdily in the switch center.	154
Fig.5.8	Simulated GaAs switch output waveform at -6 kV bias. The average electron density in the switch is also shown.	154
Fig.5.9	Calculated electron density spatial profilein GaAs switch at different times during switch operation. Note the propagating density disturbance for times ≥ 1400 ps moving from the cathode on the right.	155
Fig.5.10	Calculated electric field profile at various times during operation of a GaAs Gunn diode as reported by Ohtomo. Time increases with each successive lineout, numbered from 1 to 10. Note the high-field domain forming at the cathode at the left. (after ref.[20])	155
Fig.5.11	Electric field profiles during bulk switch operation with illumination through the ground contact at x=0: (a) simulation profiles; (b) experimental profiles. In each case, the field can be seen to collapse from the ground side, forming a peak at th opposite contact.	157
Fig.5.12	Calculated electric field profiles for Si switch at bias of -20 kV. The field collapse is uniform. Switch recovery is not seen due to long recombination time of Si.	160

Fig.5.13 Calculated Si switch output waveform at -10 kV bias. Note the decrease in switch efficiency and increase in switch risetime for decreasing optical energy. Compare to experimentally obtained results in Chapter 2. 160

Fig.A.1 Schematic of laser system consisting of Nd:YAG regenerative amplifier seeded by a Nd:YAG oscillator. This set-up is also used without the use of the optical fiber. 168

Fig.A.2 Regenerative amplifier timing sequence. (P=polarizer; QW= quarter waveplate; PC=Pockels cell; GW=glass wedge.) a) Regenerative amplifier layout. b) Before injection, the input pulses pass through the laser rod and exits the cavity before extracting any significant energy. c) At injection time, quarter-wave voltage is abruptly applied to the Pockels cell. The one pulse in transit between the Pockels cell and the opposite back mirror is trapped and regeneratively amplified. d) At the peak pulse energy, the Pockels cell is boosted to half-wave voltage and the pulse is cavity dumped .(after ref.[6]) 170

Fig.A.3 Regenerative amplifier pulse pulse trains measured with fast photodiode a) Leakage through end mirror showing pulse buildup inside amplifier cavity. The seperation of pulses is the round trip time in the amplifier cavity, 10 ns. The temporal envelope is Q-switch buildup and decay time. b) Same as in a), but with cavity dumping. c) Output pulse after external switchout; d) Amplified pulse before external switchout on expanded scale with prepulses evident. The main pulse is off-scale. 172

CHAPTER 1

INTRODUCTION

I.MOTIVATION

Photoconductive semiconductor switches have become increasingly useful for the optical generation and control of electrical signals. The basic design and operation of a photoconductor is simple: the conductance between two terminals on a piece of semiconductor material is modulated by the absorption of optical radiation in the gap between the electrodes. This creates mobile electron-hole pairs free to carry current under the influence of a bias voltage applied to the terminals. Before illumination with light, the photoconductor is "off", i.e., the gap conductance is low and little current flows between the electrodes. After illumination, the switch is "on", the gap has become conductive and current can flow from electrode to electrode. A schematic of a circuit containing a photoconductor is shown in Fig.1.1.

Photoconductors are particularily useful as photodetectors. Fluctuations in the incident optical energy can be converted into electrical signals via variations in the electrode gap conductance. A change in the gap conductance can be used to signal the absorption of light in the gap. A single photon or a flux of photons can be detected. Temporal information about an incident light pulse can be obtained by monitoring the time evolution of the gap conductance.

Another major application of photoconductors is as extremely fast closing switches. If a short-pulse laser is used to excite a photoconductive switch, the transition time from off- to on-state, or switch risetime will be quite sharp.

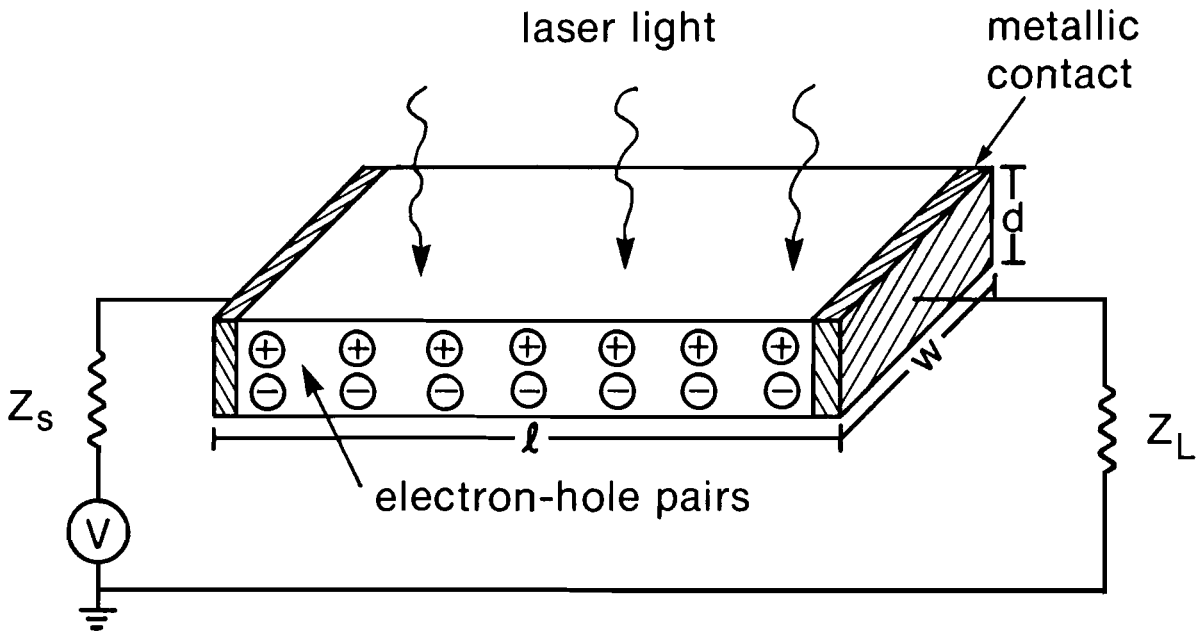

Fig.1.1 Generic semiconductor photoconductor in a circuit. The semiconductor is connected to the circuit through metallic contacts. V is the bias voltage. The source impedance is Z_s. The load impedance is Z_L. Switch dimensions l, w, and d range from microns to centimeters depending on application.

Essentially, it will be equal to the laser pulse width. Picosecond laser induced photoconductivity in Cr:GaAs was first reported by Jayaraman and Lee in 1972 [1]. Fig. 1.2 illustrates their results. Auston first demonstrated picosecond switching using Si, in 1975 [2], which made possible the operation of ultrafast (subnanosecond) optoelectronic switches, sometimes called "Auston" switches. Subpicosecond switch rise times have since been demonstrated [3].

An extremely attractive feature of photoconductive switches is that they can be used at fairly high voltages (multikilovolts) [4,5]. The speed and high voltage handling capability of photoconductive switches is superior to that of any other device [6]. A 100 kilovolt, 80 MW, laser activated photoconductive power switch has been successfully operated [7]. Photoconductive switches are particularily useful for applications that require precise timing of high-voltage electrical signals with optical signals. High-power electrical pulses with picosecond rise times can be generated that are synchronous to picosecond optical pulses. The first applications of high-power, picosecond, photoconductive switching were for use in the laser fusion facility at the Laboratory for Laser Energetics (LLE) of the University of Rochester. A completely optoelectronic prepulse suppression scheme based on photoconductive switches [8] was used with LLE's OMEGA laser system. Other early applications of high-speed, high-power photoconductive switches include Pockels cells [9], Kerr cells [10], streak cameras [11], microwave pulse generation [12], and active laser mode locking [13]. An innovative linear accelerator design that utilizes ultrafast, photoconductive switching is currently under investigation at LLE [14].

Despite the utility and relative simplicity of photoconductive switches, high-voltage operation of photoconductive switches is not completely understood. A study of photoconductive switches applied to the generation of ultrafast, high-power

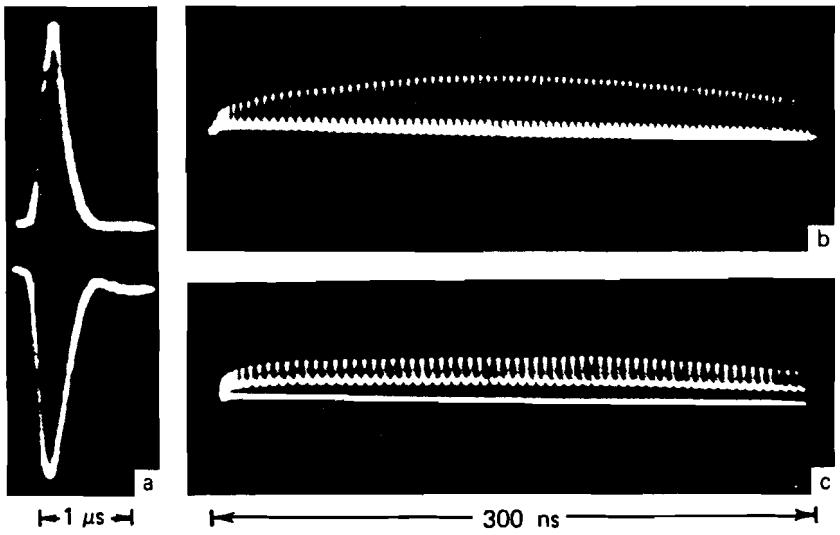

Fig.1.2 Observation of nanosecond and picosecond photoconductivity in Cr:GaAs in 1972 by Jayarman and Lee. (a) Oscilloscope trace of Q-switched nanosecond laser pulse (upper trace) and corresponding photoconductivity, (b) Oscilloscope trace of picosecond mode-locked laser pulse train, (c) Picosecond photoconductivity excited by laser pulse train shown in (b). (after ref.[1])

electrical pulses is the subject of this dissertation. The objectives of this study were: a) to develop reliable ultrafast high-voltage photoconductive switches; b) to develop diagnostics for characterizing high-voltage switch operation; c) to study photoconductive switches during operation in order to obtain a better understanding of the physics of photoconductivity under high bias conditions; d) to develop a consistent theoretical model of high-bias photoconductivity.

This chapter provides an overview of the fundamentals of semiconductor photoconductive switches and describes methods and techniques used to generate very high voltage pulses with picosecond rise times. In Chapter 2 the development of a robust, high-voltage silicon photoconductive switch and associated equipment is reviewed and the concept of electro-optic sampling will be introduced and the use of electro-optic probes in characterizing the operation of the Si switch will be discussed. Chapter 3 will discuss the evolution of electro-optic diagnostics for observing high-power photoconductive switch operation which has culminated in the development of a novel electro-optic imaging system [15]; this system can obtain two-dimensional images of the surface electric field between the electrodes of a photoconductive switch with picosecond temporal resolution. The application of this system to the study of high-field effects in high-power GaAs photoconductive switches [16], the primary focus of this work, will be covered in Chapter 4. A computer model of the photoconductive process, will be presented in Chapter 5.

II. PHOTOCONDUCTIVE SWITCH OPERATION AND DESIGN

The ideal high-power photoconductive switch would be made of material with infinite resistivity in the off-state and zero resistivity in the on-state. Ideal ohmic contacts would be made to this material, i.e., contacts with no resistance and which

present no barrier to carrier flow into or out of the switch so that the switch can then be regarded as a junctionless device. The electrodes would be connected to an external circuit with infinite bandwidth to support the high speed signals generated by the switch after excitation by an ideal laser pulse of zero pulse width. This ideal situation is not obtained with any real switch, however. Photoconductive switch performance will depend on material parameters, device geometry, contact properties, external circuit parameters, and laser pulse characteristics. This section will review the fundamentals and basic design of high-voltage switches and discuss the underlying physics of their operation. The difficulties associated with characterizing the behavior of photoconductive switches under high bias conditions will be presented, as will some of the interesting physics of semiconductors under high field conditions.

1. BASIC OPERATIONAL PRINCIPLES

In a generic photoconductor three basic processes take place: (1) carrier generation by incident light, (2) carrier transport and/or multiplication by whatever current-gain mechanism may be present, and (3) interaction of current with the external circuit to provide the output signal [17].

A. Photoexcitation

The incident light is absorbed in the semiconductor material, exciting electrons into the conduction band. The photoexcitation can result from absorption of a photon with energy equal to or greater than the band gap energy for a band-to -band (intrinsic) transition. Alternatively, the electron can be excited into the conduction band from an energy level in the energy gap by the absorption of sub-bandgap level optical illumination for an extrinsic transition. Also, two-photon absorption of sub-

bandgap illumination can excite an electron into the conduction band from the valence band directly. Picosecond two-photon absorption was first reported by Jayarman and Lee in 1972 [1]. The creation of an electron-hole pair is often the result of the excitation process, resulting in bipolar conduction. Optical excitation can also result in unipolar conduction. The process of photogeneration is shown schematically in Fig.1.3

Fig.1.3 shows a very simple semiconductor energy band structure. In reality, the band structure is more complicated, with peaks and valleys in the band edges. For Si and Ge the conduction band minimum does not lie directly opposite the valence band maximum at **k**=0; in this case a transition from the valence band to the conduction band requires the assistance of a phonon to conserve crystal momentum. This is called an indirect transition. Direct transitions are.possible in GaAs. Direct and indirect transitions are represented schematically in Fig.1.4. Direct semiconductors are characterized by a sharp wavelength cutoff in the optical absorption spectra at the wavelength corresponding to the band-gap energy, E_g. This wavelength is given by

$$\lambda_c = \frac{hc}{E_g} \tag{1.1}$$

For GaAs, E_g is 1.42 eV and, λ_c, given by eq.(1.1) is 876 nm. Indirect semiconductors have a less well defined cutoff wavelength due to the phonon energy spectrum.

Optical absorption data for GaAs and Si measured with a spectrophotometer are shown in Fig.1.5. The sharp cutoff evident in the GaAs data, Fig.1.5(b), provides evidence that GaAs undergoes direct transitions while the diffuse edge seen in the Si data, Fig.1.5(a), indicates that transitions in Si are indirect.

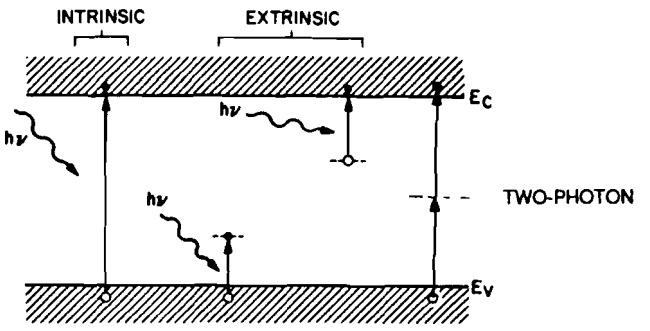

Fig.1.3 The process of photogeneration showing intrinsic (band-to-band), extrinsic (trap assisted), and two-photon photoexcitation. The incident photon energy is hν. E_c is the conduction band energy. E_v is the valence band energy. (after ref.[18])

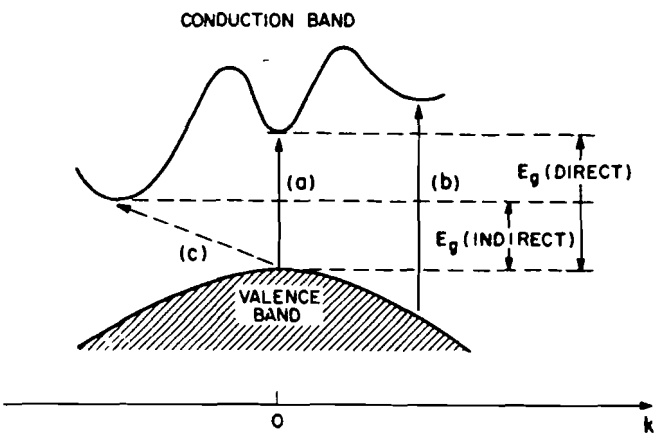

Fig.1.4 Optically excited transitions in a photoconductor: (a) and (b) direct transitions; (c) indirect, phonon assisted transition. (after ref.[19])

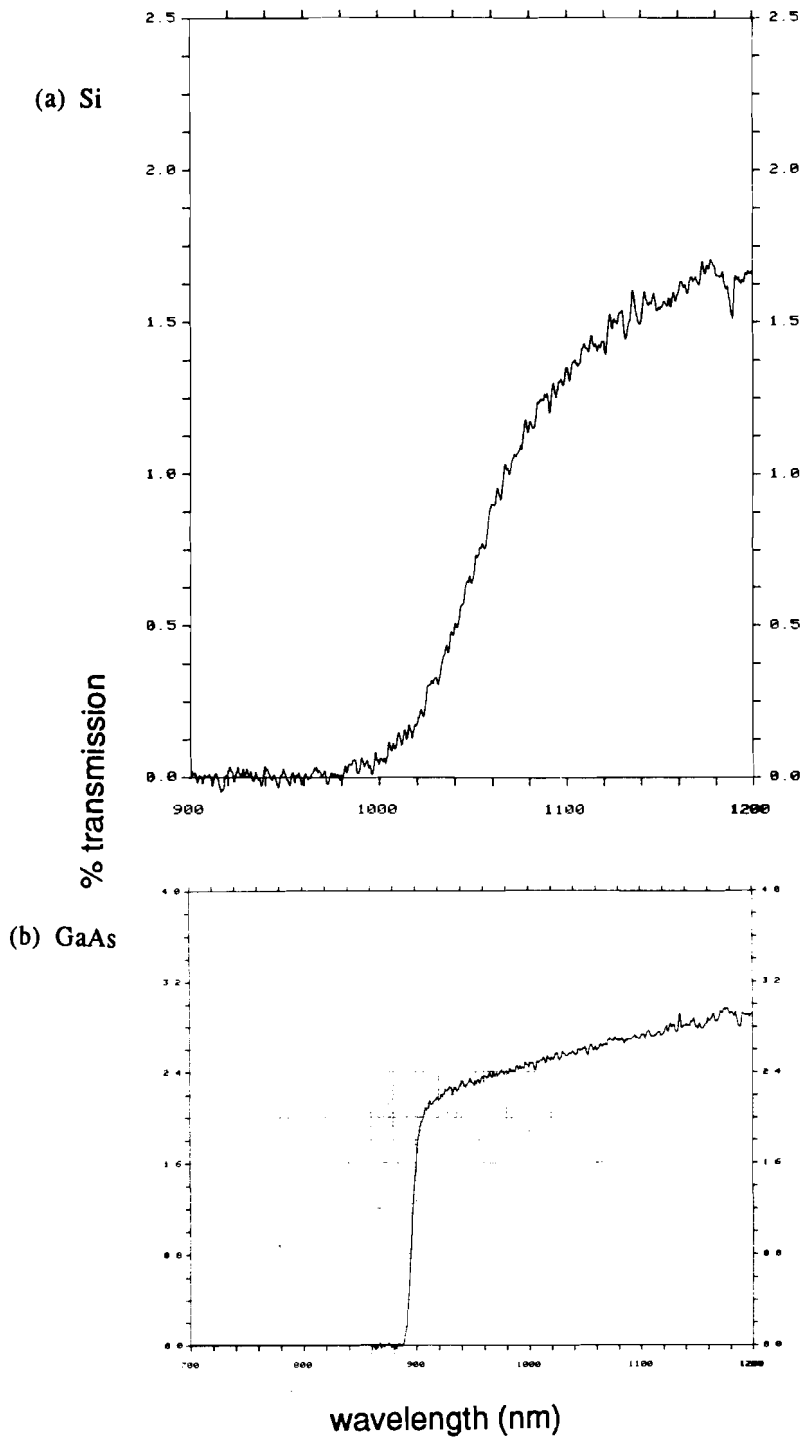

Fig.1.5 Optical transmission data for Si and GaAs. Percent transmission is plotted versus wavelength for (a) Si and (b) GaAs. The sharp transmission cutoff at about 870 nm observed for GaAs, indicative of direct optical transitions, contrasts with the diffuse edge seen in the Si data.

The absorption of a photon and the subsequent generation of an electron-hole pair is an intrinsically fast process. For most high-mobility semiconductors the quantum efficiency of this process is essentially 100%. This is determined by the probability that the electron-hole pair will escape its mutual Coulomb field. The process is limited by the uncertainty principle and the requirement that the frequency spectrum of the optical pulse fall within the absorption bands corresponding to the electron transitions from bound to free states [20]. Therefore, photogeneration proceeds on a femtosecond time scale. No intrinsic limit exists for the response of a photoconductor for any practical application. The limits arising in practice will be discussed later.

B. Recombination

Electron-hole pairs, once photogenerated, will undergo transport in the bias field and either recombine or leave the device via an electrode. Recombination, which is much slower than optical generation, involves establishing a quasi-equilibrium with the semiconductor lattice and produces a relatively long lasting current waveform. Recombination can be viewed as the reverse of carrier generation, which was depicted in Fig.1.3, and involves either an intrinsic, interband transition, or the capture of an electron or hole in a mid-gap energy level (a "trap"). Calculation of the recombination rate can become complicated, but, in general, the photogenerated current will decay exponentially with a characteristic lifetime, τ. As a first approximation, the carrier recombination rate is n/τ, where n is the carrier density. There is a great deal of physics hidden in the parameter τ, for holes and electrons may each decay with separate rates, more than one decay mechanism may be involved, and carriers may undergo scattering before recombination or exiting the device. τ is an important parameter for it gives a measure of the duration of photoinduced conductivity, i.e.,

how long the switch will remain closed. The carrier lifetime varies from semiconductor to semiconductor, and for a given material can be decreased by introducing traps to act as recombination centers. Direct semiconductors tend to have shorter carrier lifetimes than indirect semiconductors. Intrinsic Si has a carrier lifetime of several microseconds, while the lifetime of carriers in GaAs is less than one nanosecond, with values reported as short as 100-200 picoseconds. The results of a measurement of the decay time of the electrical photoconductivity in Si performed at LLE are shown in Fig.1.6. The decay time was measured to be 73 microseconds. In Fig.1.2, the response of a GaAs switch to a train of picosecond pulses was shown. This data indicates that the lifetime of the photoconductivity must be less than the spacing between pulses. Jayarman and Lee calculated the lifetime to be 1/10 ns [1]. From a practical standpoint, electrical pulses can only be generated with a maximum duration of the order of the carrier lifetime. This should preclude the use of short lifetime materials like GaAs for production of electrical pulses > 1 ns, although GaAs switches have been observed to remain conductive for as long as the external circuit can supply current when under high bias (> 4 kV/cm). This anomalous behavior of GaAs has been given the name "lock-on" (because the switch locks into the conductive state) [21]. It will be discussed in more detail in later chapters.

C. Switch Resistance and Carrier Mobility

The off-state resistance of a photoconductive switch is determined by the bulk resistivity, ρ, of the switch material. Typically, photoconductive switches are made of semi-insulating material for high off-state resistance. Referring to the simplified photoconductive switch shown in Fig.1.1, the switch resistance, R_S, is given by

$$R_S = \frac{\ell \rho}{A} \tag{1.2}$$

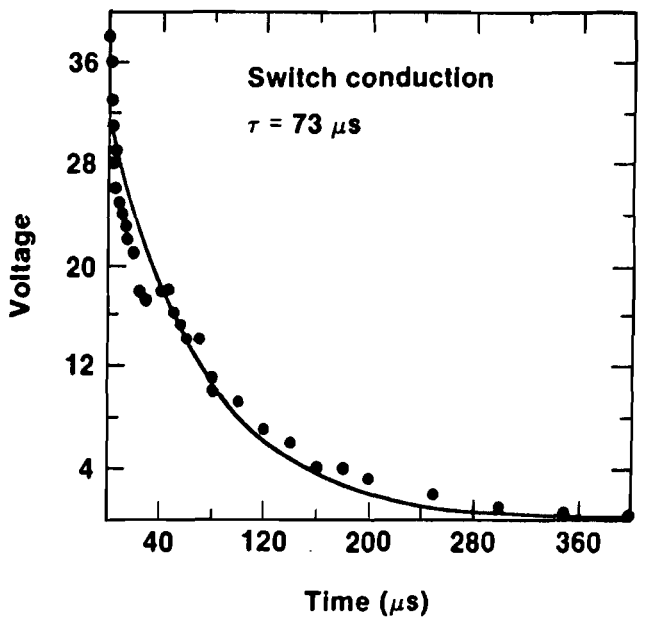

Fig.1.6 Decay of electrical conductivity of a Si photoconductive switch after illumination by a 100 ps laser pulse. The conductivity was probed with an electrical pulse at various times after illumination. The voltage switched as a function of electrical pulse delay is plotted. τ was measured to be 73 μsec.

where ℓ is the distance between electrodes, and A is the area of the photoconducting volume. For most practical switches, R_S is $10^5\ \Omega$-$10^6\ \Omega$ in the off-state. High resistance is desired so that the off-state, or "dark" current, is small. This dark current occurs because even though R_S is large, it is still finite, so a bias voltage placed across the switch will cause a current to flow even when the switch is not illuminated. Several semiconductors have been investigated for use as high-voltage photoconductive switches, among these are Si [5], GaAs [22], Fe:InP [23], GaP [24], $CdS_{0.5}Se_{0.5}$ [25], and diamond [26]. The most popular materials are Si and GaAs, and this work will deal only with Si and GaAs switches. Some pertinent physical properties of Si and GaAs are listed in Table 1.1.

GaAs is particularily suited for high-voltage applications due to its high resistivity ($\rho > 10^8\ \Omega$-cm). It is less susceptible to thermal runaway than Si ($\rho \sim 10^5\ \Omega$-cm) and other less resistive materials. Thermal stability is an important consideration at the high fields to which switches are exposed in pulsed-power applications, where field strengths of 1-50 kV/cm are typical. At such field strengths, the small number of thermally generated carriers, which are always present, can be accelerated to high enough energies to create more carriers through impact ionization. This can lead to a catastrophic breakdown across the switch, similar to the formation of a spark in a gas. The switch will then become activated prior to the arrival of the laser pulse. Joule heating created by the high bias can thermally generate more carriers and hasten the onset of avalanche breakdown. A second, non-destructive process, thermal runaway, can also occur when the thermally generated current heats the switch through electron-phonon collisions, thermally generating more current, etc., until the switch is completely conductive. High dark resistivity decreases the dark current and the effect of Joule heating. Joule heating can also be minimized by decreasing the time the

Table 1.1

Physical Properties of Si and GaAs

Silicon	
Sum of electron and hole mobilities (300 K)	1925 cm^2/Vs
Carrier lifetime	1 ns- 1 ms
Intrinsic resistivity at 300 K	0.23 MΩ cm
Dark current heating (10 MV/m, 300 K)	2 kW/cm^3
Absorption depth (1.06 μm light)	1 mm
GaAs	
Sum of electron and hole mobilities (300 K)	9300 cm^2/Vs
Carrier lifetime	0.1 ns- a few ns
Intrinsic resistivity at 300 K	10^8 MΩ cm
Dark current heating (10 MV/m, 300 K)	0.2 kW/cm^3
Absorption depth (1.06 μm light)	varies with impurity concentration

(after ref.[27])

switch is exposed to high voltage before activation. DC biasing at high voltages is avoided. The duration of the bias pulse must be less than the thermal instability build-up time [28]. Mathur *et. al.* showed that a 3 mm cube of GaAs could be DC biased at 15 kV without breakdown [25]. In contrast, a 2 mm Si gap can hold off multi-kilovolt bias voltage for only tens of microseconds [5].

The conductivity, $\sigma = 1/\rho$, is given by

$$\sigma = (ne\mu_e) + (pe\mu_h) \tag{1.3}$$

where n and p are the electron and hole density, respectively; e is the electronic charge; and μ_e and μ_h are the electron and hole mobility, respectively. These carrier densities are the photogenerated, or excess, densities, plus the equilibrium values. The photogenerated densities are generally orders of magnitude greater than the equilibrium densities. If the incident photons create electron hole pairs, n = p , thus, the conductivity can be written in terms of an effective mobility, μ , which is the sum of the electron and hole mobilities,

$$\sigma = ne(\mu_e + \mu_h) = \mu ne \quad . \tag{1.4}$$

The mobility, μ , is defined as the proportionality constant between the carrier drift velocity and the electric field, E.

$$v_d = \mu E \, . \tag{1.5}$$

Various mechanisms affect the carrier mobility and, in general, the mobility is a function of the effective carrier mass and the temperature. For low electric fields, μ is a constant, but at high electric fields (> 1 kV/cm) the behavior of μ can be more complicated. Fig.1.7 shows measured values of the carrier velocity versus electric field for high purity Ge, Si, and GaAs. For Si and Ge, the carrier velocity increases linearly with electric field, obeying Eq.(1.5), until a saturation velocity, v_s, is

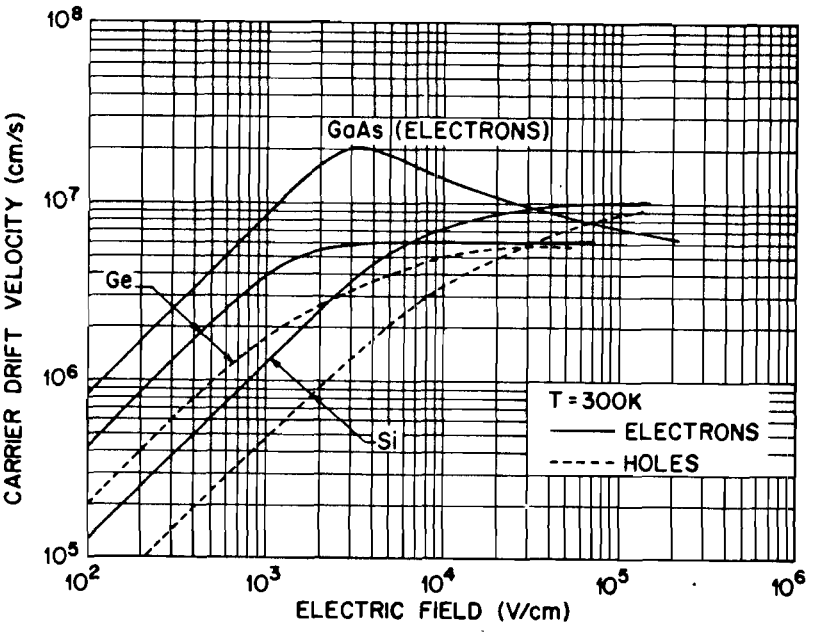

Fig.1.7 Measured value of the carrier drift velocity versus electric field for high purity Ge, Si, and GaAs. For Ge and Si, the carrier velocity increases linearly with electric field until the velocity saturates. In GaAs, carrier velocity increases linearly with field until about 3.2 kV/cm and then decreases with increasing field.(after ref.[29])

reached. v_s equals about 6×10^6 cm/s for Ge, and 1×10^7 cm/s for Si. For GaAs, v_d increases linearly with electric field for fields up to about 3.2 kV/cm, but decreases with increasing field for greater fields. This is due to the field induced transfer of electrons from the high-mobility conduction band valley centered at **k**=0 (Γ point) to higher energy, low-mobility satellite valleys (L and X). The decrease in velocity results from a combination of an increase in the electron effective mass and an increase in the density of electron states from the low-energy valley to the high-energy valley. This decrease in the carrier velocity with increasing field results in an effective increase in the bulk switch resistance with increasing field, often called "negative differential resistivity" (NDR). NDR is commonly refered to as the "Gunn effect", after J.B.Gunn, who first observed manifestations of NDR in 1963 [30]. The mechanism for NDR was first proposed independently by Ridley and Watkins [31], and by Hilsum [32]. NDR will be discussed in more detail in later chapters, as the observed behavior of GaAs photoconductive switches operating at high bias voltages may be partially explained by the onset of NDR at high fields.

The on-state switch resistance can be written

$$R_S = \frac{\ell}{\sigma A} = \frac{\ell}{n\mu e A} = \frac{\ell^2}{N\mu e} \tag{1.6}$$

where N equals the total number of photogenerated carriers [33]. N is proportional to the absorbed optical energy, E_{opt} , and is given by

$$N = 2\,\frac{E_{opt}}{E_\gamma} \tag{1.7}$$

where E_γ is the energy per photon of the incident optical pulse. The factor of two is included as each photon produces an electron-hole pair. As a typical example, consider a 1 cm cube GaAs power switch which is in a circuit as in Fig. 1.1. The

switch is illuminated uniformly with 100 μJ of infared optical energy ($E_\gamma = 1.17$ eV) for $n \sim 10^{14}$ cm^{-3}. From Table 1.1, $\mu = 9300$ cm^2/Vs, so

$$R_s = \frac{1\ cm^2}{2\ e\ (\frac{100\mu J}{1.17eV})\ (9330\ cm^2/V\text{-}sec)} \sim .6\ \Omega\ .$$

The off-state resistance of this switch would be $10^8\ \Omega$. The switch undergoes a tremendous change in resistance from the off- to the on- state, being essentially transformed into a quasi-metallic state. The switch resistance is then negligible as compared to any other impedance in the circuit, and, as a circuit element, behaves like a connecting wire. This transformation will take place on a time scale comparable to the pulse width of the incident laser pulse, which with the advent of high-power, short-pulse lasers can be on the picosecond time scale. When the switch becomes conductive, the electric field across the switch collapses and the voltage across the switch drops. If R_s drops to a value much less than the load resistance, Z_L, the bias voltage will appear across the load. The voltage switched to the load, V_L, for the circuit shown in Fig.1.1, is

$$V_L = \frac{Z_L}{Z_s + Z_L + R_s} V_{bias} \tag{1.8}$$

To switch the maximum voltage to the load, R_s is made as small as possible. From Eq(1.6), R_s scales inversely with the carrier density and linearly with the gap length squared. In general, ℓ is made as small as possible to minimize the required E_{opt}, and E_{opt} is as large as possible to minimize R_s. R_s is a function of time, decreasing rapidly during the absorption of the incident light pulse and then returning relatively slowly to its off-state value. During this transition period, the electric field in the switch and the voltage across the switch undergo great variation. The carrier mobility, μ, being a function of the electric field, varies rapidly in time, as well.

There is no simple analysis that yields a complete description of the rapid spatial and temporal variation of the switch electric field, potential, mobility, and carrier density, except for the low-field, or constant μ regime [34].

2. PRACTICAL PHOTOCONDUCTIVE SWITCHES

The photoconductive switch, although a relatively simple device, does require special engineering considerations to be used in a circuit. These issues will be reviewed in this section.

A. Material Requirements

Many of the material requirements for photoconductive switches have already been discussed. Desirable material properties include high dark resistivity, for low dark current and reduced off-state heating; and high carrier mobility, for increased conductivity for a given photogenerated carrier density. It is also important that good ohmic contacts can be made to the material.

While no material is perfect, GaAs and Si provide reasonable compromises, and are the primary semiconductors used in high-power switches. GaAs and Si material for use in photoconductive switches is, in general, readily available. Photoconductive switching, being a bulk process, does not depend on any particular doping profile, but only on the bulk properties of the material. While intrinsic Si and GaAs work well as photoconductors, for particular applications, dopants can be added to Si or GaAs. For example, Au-doped Si has a recombination time (~50 ns) considerably less than intrinsic Si (~μsec) and can hold off a kilovolt DC bias at liquid-nitrogen temperature [35] . In general, however, adding dopants to Si will decrease the already low room temperature resistivity, and the highest purity intrinsic Si is used for the highest resistivity possible. Cr is a typical dopant for GaAs.

Doping GaAs with Cr pins the Fermi level at the middle of the band gap which increases the bulk resistivity over intinsic GaAs. Cr-doping of GaAs also decreases the carrier lifetime as the Cr traps act as recombination centers. Cr:GaAs is a particularily popular photoconductive switch material, but intrinsic GaAs is more efficient due to its increased mobility.

B. Contact Requirements

One of the main difficulties in constructing a reliable photoconductive switch is in making connections to the external circuit. The importance of making good electrical connection to the semiconductor material must be emphasized. While illumination will reduce the bulk resistance, it will not reduce any contact resistance present. Ohmic contacts with negligible contact resistance must be applied to the switch. This can present a technological problem, as a Schottky barrier usually forms along the metal/semiconductor interface of semi-insulating materials. This produces non-ohmic behavior and can introduce a photovoltaic response in addition to the photoconductive response [20]. In the study of photoconductivity, contact effects must be negligible compared to the effect of interest. Also, any residual resistance in the contact can contribute to Joule heating in the switch, which may ultimately lead to switch failure. If the switch is pulse-biased, resistance in the contact will present a discontinuity to the charging pulse which will generate reflections and lower the switch efficiency [36].

To produce good contacts, some care must be taken. It is difficult to apply metallic contacts to intrinsic Si, as any dopants introduced into the material during contact application will increase the switch conductivity. Various methods for placing ohmic contacts on intrinsic Si have been investigated at LLE [36].

First, metallic contacts are applied to the Si substrate by vapor deposition. The electrode pattern is made either by using a mechanical mask during the metal deposition process, or using a photolithographic process, typical of integrated circuit manufacture. Al and Au have been tried as the contact metal on Si. Aluminum has been found to be poor choice for the contact metal due to migration of the Al into the Si after long-term switch use. Gold has been found to provide a good contact to Si. Metal thicknesses are typically several thousand angstroms. Contact pads have typical dimensions on the order of millimeters, depending on application. The contact pad can be annealed by scanning a tightly focused laser beam across the entire contact pad, providing localized heating, or the contacts can be sintered in an oven.

Various formulae have been tried for producing ohmic contacts on GaAs [37]. One particular scheme, after much experimentation, has proven to produce good contacts. It involves depositing Ni:AuGe contacts on the GaAs substrate and then sintering the contacts in an oven. A very thin (~100 Å) layer of Ni is first deposited on the substrate. This is followed by a relatively thick (~1000 Å) layer of AuGe alloy. A photolithographic technique is used to pattern the contacts. The contacts are then sintered at ~450° C for ~10 minutes. This process of making ohmic contacts, briefly described here, has been detailed by Meyer [38] .

Attempts have also been made to improve contact performance by doping the area directly underneath the contact, producing a thin n^+ or p^+ region. This improves the transition from the contact to the bulk.

C. External Circuit

A good metallic contact on the semiconductor does not insure optimum switch performance. The external circuit may greatly affect switch performance. The circuit geometry in which the photoconductive switch is used limits the pulse rise time even

if the switch closes in zero time [7] . An important consideration is the bandwidth of the external electrical circuit. With switching times of 1 to 100 ps, the switched pulse will have bandwidths of 3 to 300 GHz. It is important that the external electrical circuit support these signal frequencies. To accurately measure switch performance, the switching circuit should have a bandwidth greater than the effective bandwidth of the switched signal so that circuit limitations do not mask true switch behavior. Practical switches are connected to some kind of transmission line with a large acceptance bandwidth. The connection of the switch electrode must be mechanically sound and blend smoothly into the external circuit. Striplines can be fabricated directly on the semiconductor substrate itself, using one of the proven techniques for making contacts discussed earlier. Alternatively, the switch can bridge a gap in a stripline on a dielectric substrate. The switch can also be placed in a coaxial transmission line, replacing a section of the center conductor. Various switch geometries are shown in Fig.1.8

Fabricating high bandwidth circuits is a well understood problem. The difficulty in producing photoconductive switching circuits is the high voltage associated with the switched signals. High bandwidth is generally associated with compact structures. Compact structures are not generally associated with high power applications. The switching circuit must be robust enough to handle multikilovolt pulses and yet be electrically clean so as not to degrade switch performance. The compactness of the circuit is constrained by the need to keep electrical field strenghs less than the breakdown level [6] . This problem with electrical breakdown extends to all parts of the electrical circuit. Charging and load resistors, cables, etc., must all be able to withstand high voltage. The associated high-voltage bias pulser must also

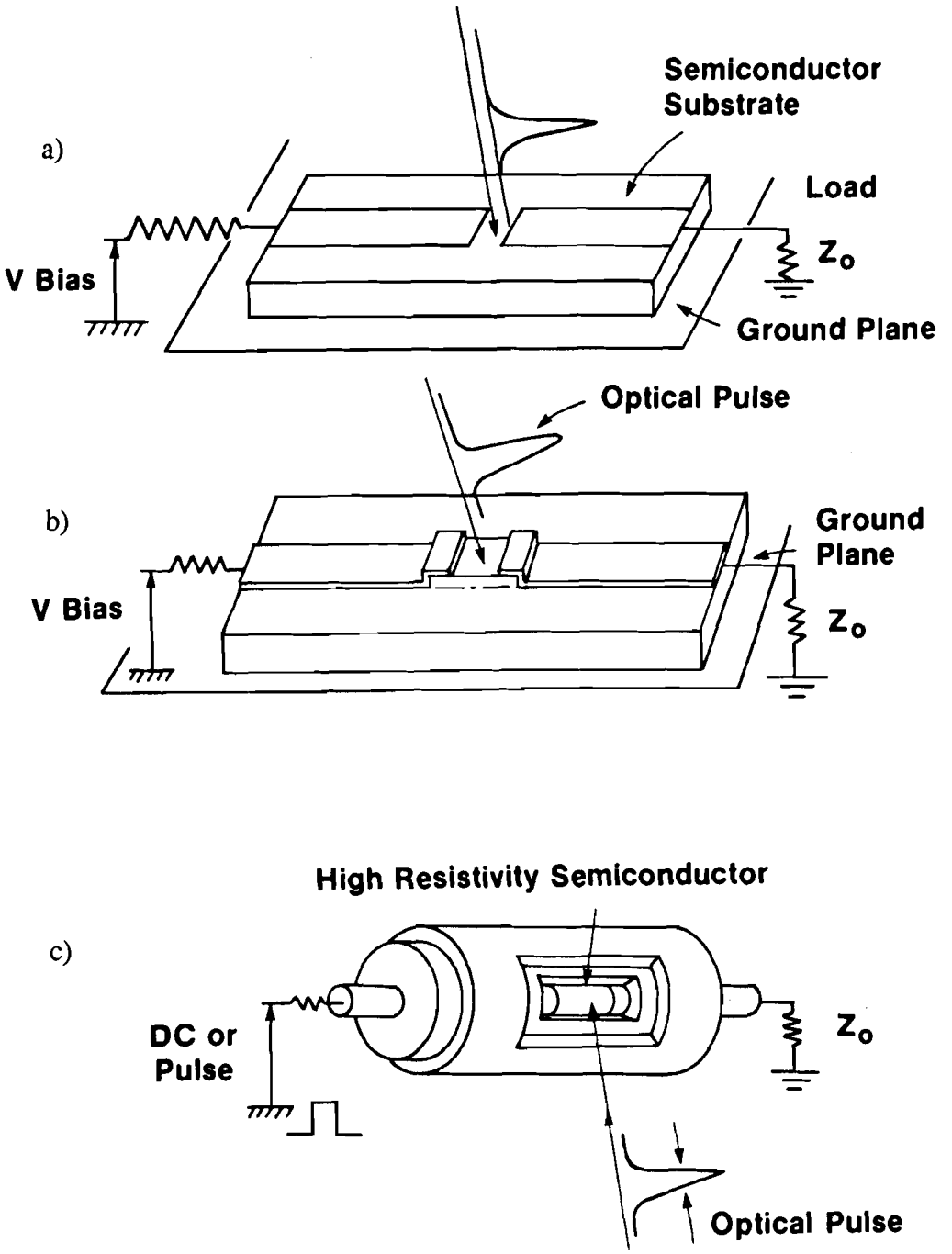

Fig.1.8 Three different geometries for photoconductive switches. (a) stripline geometry where the stripline is directly on the semiconductor substrate, (b) stripline geometry where the switch bridges a gap in a stripline on a dielectric material, (c) Coaxial geometry where the semiconductor element has replaced a portion of the center conductor. (after ref.11)

be of appropriate design. Circuits designed for high-voltage switching are generally large and rugged.

The minimum circuit limited rise time is determined by the characteristic rise time of the switch geometry. For a switch embedded in a transmission line, as in Fig.1.8, the rise time of the switch, τ_r, will be limited to

$$\tau_r = \sqrt{\varepsilon_r}\,\frac{\ell}{c} \tag{1.17}$$

where ε_r is the relative permittivity of the dielectric in the stripline. Before illumination, the switch has a high, yet finite, resistance, and there is a voltage gradient across the switch from the bias side to the load side. In effect, a voltage "ramp" is "frozen" into the switch, which will be released upon illumination. Eq.(1.17) can be heuristically interpreted as being the time time required for this "frozen ramp" to transit the switch gap. For the 1 cm cube of GaAs from earlier examples, τ_r is ~120 ps. There will also be some intrinsic geometric limitation imposed by the capacitance of the switch contacts, C. This limitation is the time constant R_sC, R_s being the on-state resistance of the switch. For most switches, C < 1 pF and R_s is several ohms, so R_sC is typically on the order of femtoseconds or picoseconds and does not place a practical limit on switch rise time. For a well designed circuit, the turn-on time is dominated by the optical pulse duration.

D. Switch Breakdown

The parameter ℓ, the electrode separation distance, appears in Eq.(1.17) and Eq.(1.6). Both equations indicate that ℓ should be minimized. Small ℓ is desired to decrease the volume of semiconductor that must be optically excited and, thus, increase the photogenerated carrier density for a given optical pulse, and to achieve the fastest possible switch rise time. ℓ must also satisfy the relationship

$$V_{bias} < \ell E_{br} \tag{1.18}$$

where E_{br} is the bulk dielectric breakdown field strength of the semiconductor. A typical value for E_{br} would be 100 kV/cm or less. In a test done at LLE, a 1/2 mm of Cr:GaAs could withstand a pulse-bias field of 184 kV/cm at a 1 kHz pulse repetition rate for only several minutes before undergoing bulk breakdown. In general, semiconductor switches will breakdown along the surface between electrodes at a much lower field strength than the bulk breakdown field, placing an even tighter constraint on ℓ for high voltage operation. For a given bias voltage, the choice of ℓ is always a compromise between decreasing ℓ for switching speed and efficiency and increasing ℓ to stay below the threshold for surface breakdown. To achieve optimal switching, switches are usually operated very close to the breakdown point and often need to be immersed in transformer oil or SF_6, or epoxy-encapsulated to avoid surface breakdown.

E. Optical Pulse Requirements

For efficient photoconductive switching with a fast rise time, a short, high-energy laser pulse is required. A short pulse is required for fast switch response and high energy is needed to generate high carrier density in the switch bulk. Referring to the earlier example, 100 μJ of infared energy (λ = 1064 nm, E_γ = 1.17 eV) is required to excite a 1 cm cube of GaAs to an on-state resistance of .6 Ω. To obtain ultrafast switching this 100 μJ would have to be delivered on a picosecond time scale. Special techniques are required to produce picosecond laser pulses with such energy.

The laser wavelength must be consistent with the optical transitions in the semiconductor material. All photoconductive switching described in this work was done with infrared laser pulses,λ = 1064 nm, or the second harmonic, λ = 532 nm. Silicon, with a band gap of E_g = 1.12 eV, can undergo an intrinsic transition by

absorbing one-photon of infrared energy (E_γ = 1.17 ev). Switching in GaAs, E_g = 1.42 eV, with infrared pulses must be due to extrinsic transitions or two-photon absorption. For Cr:GaAs, the switching is accomplished through assistance of the deep Cr trap located .63 eV below the conduction band. For intrinsic GaAs, the switching is through the EL2 defect .75 eV below the conduction band [39] . The absorption depth for 1 μm light in Si is ~1 mm. The absorption depth in GaAs will vary with impurity concentration, as a trap or defect may be involved. A measurement of the absorption coefficient for 1064 nm light in a sample of intrinsic GaAs yielded a value of 1.39 cm^{-1} for an absorption depth of ~7 mm. The absorption depth effectively limits the conducting volume of the switch. As the switch in the on-state is a conductor, there will be some effective penetration depth in the switch for fast electrical signals. The most efficient switching is obtained when the laser absorption depth is matched to the skin depth [27] .

The laser pulse used must also be very clean. i.e., not be preceded by prepulses. This can be difficult to achieve, as prepulses will inevitably result when one pulse is selected at some point in the lasing cycle from a train of optical pulses. A high contrast ratio between prepulses and the main pulse is essential. The prepulses do not have enough energy to fully activate the switch, however, Si, with its long carrier lifetime, can integrate the energy of all the prepulses. The switch will turn on with a slow ramp rather than a sharp rise. GaAs, with its short carrier lifetime, is less likely to integrate the prepulses. Even still, optical prepulses can reduce switch efficiency by depleting the charging system used to bias the switch before the main pulse arrives [6] . Also, if the bias field is high enough, the small number of carriers created by the optical prepulses can trigger an avalanche in the switch [40].

The laser system used in this work, a Nd:YAG regenerative amplifier seeded by a mode-locked Nd:YAG oscillator [41], produced laser pulses at 1064 nm (E_γ = 1.17 eV) with a nominal pulse width of 100-200 picoseconds. The main pulse to prepulse ratio was ~10^4. This system is described in more detail in Appendix A.

F. Switch Diagnostics

Having constructed an adequate photoconductive switching circuit, it is then desired to characterize the circuit and observe the switch behavior. Characterizing the operation of photoconductive switches operating at high speed at very high voltages can present many difficulties. Electronic probes with ultrafast temporal response that can operate at kilovolt levels are extremely difficult to construct. Except at relatively low voltage levels (< 1 kV), direct connection to the circuit is impossible. At low voltages, it is possible to connect directly to the load or source side of the switch and observe the switching on an oscilloscope, although the signal will usually require attenuation. The bandwidth of readily available analog oscilloscopes, however, is not sufficient to resolve transient events on a time scale less than ~1 ns. State-of-the art analog oscilloscopes or sampling oscilloscopes can access the picosecond regime but can only be used to study low voltage switching. The attenuators used to allow direct connection of an oscilloscope to the circuit may themselves degrade the signal, defeating their purpose. Also, direct attenuators are, themselves, subject to electrical breakdown. Direct connection to a high voltage circuit is practicable only when the bias voltage has been lowered to a level which will not be hazardous to the associated test electronics. While this does not allow high-voltage effects to be studied, it does facilitate alignment and timing of the optical system and the switching circuit. Low voltage switching of Si, monitored directly at the load resistor with a Tektronix

(a)

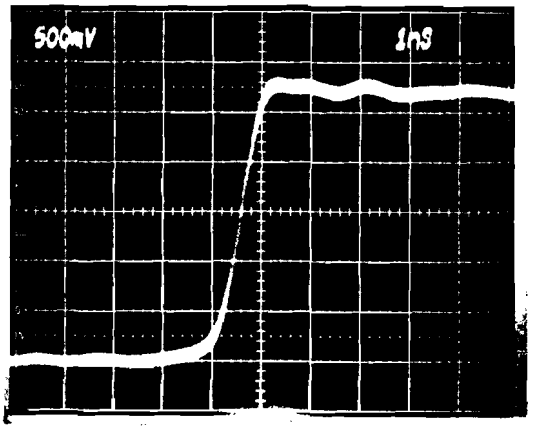

(b)

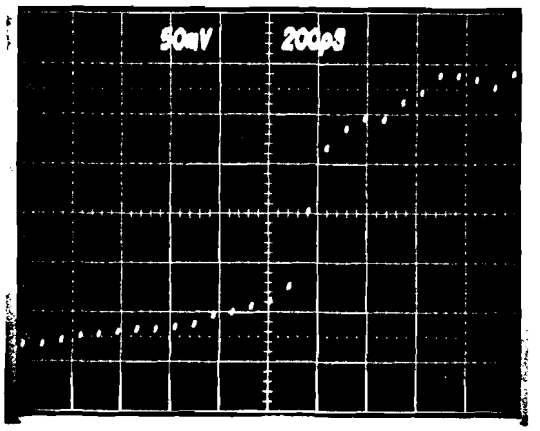

(c)

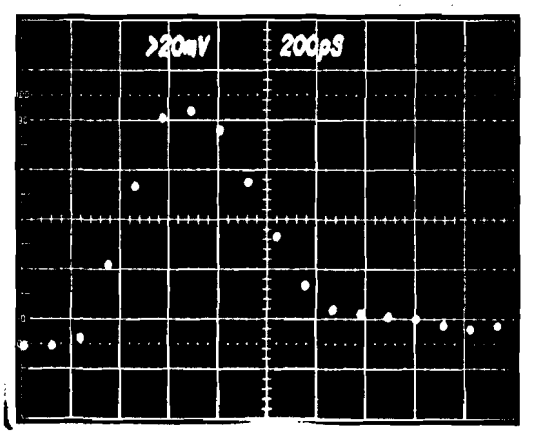

Fig.1.9 Low-voltage switching in Si monitored directly across the load resistor. A ~200 ps, λ=1064 nm laser pulse was used to excite the switch (a) Analog oscilloscope trace of switched voltage pulse. The rise time is scope limited to 1 ns. (b) Tektronix sampling scope trace showing ~200 ps rise time. (c) Sampling scope trace of the output of a diode used to monitor the exciting laser pulse.

sampling oscilloscope is shown in Fig.1.9. The voltage "ramp" seen in Fig.1.9(b) before the main switching is due to laser prepulses An analog oscilloscope trace of a switched pulse is also shown for comparison, as is a sampling scope trace of the optical pulse. This data represents the practical temporal resolution limit of direct connection to the switching circuit.

Indirect connection, such as capacitve or inductive coupling, must be made to the circuit to monitor switching at high voltage. While capacitive voltage probes and inductive current probes can operate at multikilovolt levels, their temporal response is limited by their internal time constants to, again,~1 ns. Fig.1.10 shows an oscilloscope trace of high-voltage switching in Si monitored on the bias side of the switch with a capacitive high-voltage probe. The bias is a 1 kV negative voltage pulse. The optical pulse is timed to arrive at the peak of the bias pulse. When the switch is activated, the bias side of the switch is grounded through the load resistor. The data in Fig.1.10 is probe and scope limited to ~ 1 ns.

Standard methods are not adequate to characterize and study ultrafast photoconductivity in high-power switches and special techniques have to be used to make picosecond time scale measurements. The development of these techniques will be discussed in chapters 2 and 3.

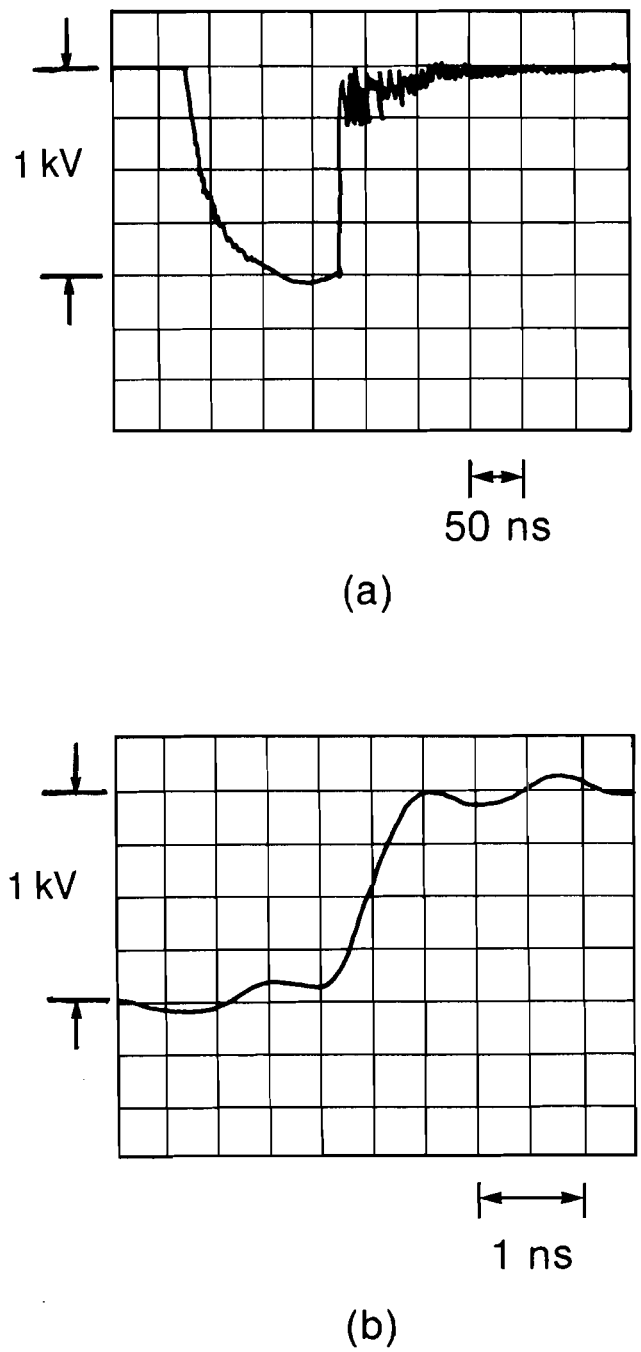

Fig.1.10 Photoconductive switching in Si monitored at the bias electrode with a capacitive probe. The switch was pulse-biased at -1 kV. When the switch is activated by the ~200 ps, 1064 nm laser pulse the bias pulse is switched to ground. Traces shown for (a) 50 ns/div, and (b) 500 ps/div.

CHAPTER 1

REFERENCES

[1] S. Jayarman and C.H. Lee, "Observation of Two-Photon Conductivity in GaAs with Nanosecond and Picosecond Light Pulses," *Appl.Phys.Lett.* **20**, 392-395 (1972).

[2] D.H. Auston, "Picosecond Optoelectronic Switching and Gating in Silicon," *Appl.Phys.Lett.* **26**, 101-103 (1975).

[3] J.A. Valdmanis, G. Mourou, and C.W. Gabel, "Subpicosecond Electrical Sampling," *IEEE Jour.Quant.Elect.* **QE-19**, 664 (1983).

[4] P.le Fur and D.H. Auston, "A Kilovolt Picosecond Optoelectronic Switch and Pockels Cell," *Appl.Phys.Lett.* **28**, 21-23 (1976).

[5] G. Mourou and W. Knox, "High Power Switching with Picosecond Precision," *Appl.Phys.Lett.* **35**, 492 (1979).

[6] W.R. Donaldson, "Ultrafast High Power Switching: Techniques and Applications," Proceedings, **ELECTRO/89**, New York, April,1989.

[7] W.C. Nunnally and R.B. Hammond, "80-MW Photoconductor Power Switch," *Appl.Phys.Lett.* **44**, 980 (1984).

[8] G. Mourou, J. Bunkenburg, and W. Seka, "Electro-Optic Prepulse Suppression for Laser Fusion Systems," *Optics Comm.* **34**, 252 (1980).

[9] J. Agostinelli, G. Mourou, and C.W. Gabel, "Active Pulse Shaping in the Picosecond Domain," *Appl.Phys.Lett.* **35**, 731 (1979).

[10] M. Stavola, J. Agostinelli, and M. Sceats, "Ultrafast Pulse Shaping with a Travelling Wave Kerr Cell and Picosecond Rise Time Electrical Pulse," *Appl.Optics* **18**, 4101 (1979).

[11] G. Mourou and W. Knox, "A Picosecond Jitter Streak Camera," *Appl.Phys.Lett.* **36**, 623 (1980).

[12] G. Mourou, C.V. Stancampiano, A. Antonetti, and A. Orzag, "Picosecond Microwave Pulses Generated with a Subpicosecond Laser-Driven Semiconductor Switch," *Appl.Phys.Lett.* **39**, 295 (1981).

[13] W. Margulis, W. Sibbett, and J.R. Taylor, "Active Mode-Locking of Lasers Using GaAs and GaP Picosecond Switches," *Optics Comm.* **35**, 153 (1980).

[14] C. Bamber, W. Donaldson, T. Juhasz, L. Kingsley, and A.C. Melissinos, "Radial Compression of Picosecond Electrical Pulses," *Part.Accel.* **23**, 255 (1988).

[15] L.E. Kingsley and W.R. Donaldson, "Electro-Optic Surface Field Imaging System," *Digest of Technical Papers,* 7th IEEE Pulsed Power Conf., edited by R. White and B.H. Bernstein (IEEE, New York, 1989) pp.376-379.

[16] L.E. Kingsley and W.R. Donaldson, "Electro-Optic Imaging of Surface Electric Fields in High-Power Photoconductive Switches," *IEEE Trans. Elect. Dev.*, **ED-37** (12), 2449 (1990).

[17] S.M. Sze, *Physics of Semiconductor Devices*, 2nd ed.,(John Wiley and Sons, New York, 1981) p.744.

[18] Ibid, p.745; base figure © John Wiley and Sons, Used with Permission.

[19] Ibid, p.41; © John Wiley and Sons, Used with Permission.

[20] D.H. Auston, "Picosecond Photoconductors: Physical Properties and Applications," *Picosecond Optoelectronic Devices*, edited by C.H. Lee (Academic Press, Orlando,1984), pp.73-117.

[21] G. Loubriel, M.W. O'Malley, and F. Zutavern, "Toward Pulsed Power Uses for Photoconductive Switches: Closing Switches," *Digest of Technical Papers,* 6th IEEE Pulsed Power Conf., edited by P.J. Turchi and B.H. Bernstein (IEEE,New York, 1987) pp.145-148.

[22] C.H. Lee, "Picosecond Optoelectronic Switching in GaAs," *Appl.Phys.Lett.* **30**, 84 (1977).

[23] F.J. Leonburger and P.F. Moulton, "High Speed InP Optoelectronic Switch," *Appl.Phys.Lett.* **35**, 712 (1979).

[24] W. Margulis and W. Sibbett, "Picosecond GaP Switches," *Optics Comm.* **37**, 224 (1981).

[25] V.K. Mathur, C.S. Chang, W.-L. Cao, M.J. Rhee, and C.H. Lee, "Multikilovolt Picosecond Optoelectronic Switching in CdS0.5Se0.5," *IEEE Jour.Quant.Elect.* **QE-18**, 205 (1982).

[26] P.-T. Ho, C.H. Lee, J.C. Stephenson, and R.R. Cavanagh, "A Diamond Opto-Electronic Switch," *Optics Comm.* **46**, 202 (1983).

[27] W.C. Nunnally and R.B. Hammond, "Optoelectronic Switch for Pulsed Power," *Picosecond Optoelectronic Devices*, edited by C.H. Lee (Academic Press, Orlando,1984), pp.373-398.

[28] G. Mourou, W.H. Knox, and S. Williamson, "High Power Switching in Bulk Semiconductors," *Picosecond Optoelectronic Devices*, edited by C.H. Lee (Academic Press,Orlando,1984), pp.219-248.

[29] Sze, op. cit., p.46.

[30] J.B. Gunn, "Microwave Oscillation of Current in III-V Semiconductors," *Solid State Commun. 1* **88**, (1963).

[31] B.K. Ridley and T.B. Watkins, "The Possibility of Negative Resistance Effects in Semiconductors," *Proc.Phys.Soc.Lond.* **78**, 293 (1961).

[32] C. Hilsum, "Transferred Electron Amplifiers and Oscillators," *Proc.IRE* **50**, 185 (1962).

[33] C.H. Lee, "Picosecond Optoelectronic Devices Based on Optically Injected Electron-Hole Plasma," *Picosecond Optoelectronic Devices*, edited by C.H. Lee (Academic Press,Orlando,1984) pp.119-188.

[34] M. Weiner, L. Bovino, R. Youmans, and T. Burke, "Modeling of the Optically Conrolled Semiconductor Switch," *Jour. Appl. Phys.* **60** (2), 823 (1986).

[35] M. Stavola, G. Mourou, and W. Knox, "Picosecond Switching of a Multi-Kilovolt DC Bias with Laser Activated Silicon at Low Temperature," *Optics Comm.* **34**, 252 (1980).

[36] W.R. Donaldson and G. Mourou, "Improved Contacts on Silicon for High Voltage Photoconductive Switching," *Digest of Technical Papers*, Fifth IEEE Pulsed Power Conf., edited by P. Turchi and M. Rose.(IEEE, New York, 1985) pp.590-593.

[37] V.L. Rideout, "A Review of the Theory and Technology for Ohmic Contacts to Group III-V Compound Semiconductors," *Solid State Elec.* **18**, 541 (1975).

[38] K. Meyer, "Study of Picosecond Electron Transport in GaAs Using Transient Photoconductivity and Transient Absorption Spectroscopy," Thesis(Ph.D.)-University of Rochester, Dept. of Physics and Astronomy, (1988).

[39] T. Burke, M. Weiner, L. Bovino, R. Youmans, "The Role of Deep Traps in the Optically Controlled Semi-insulating GaAs Switch," *Digest of Technical Papers*, 6th IEEE Pulsed Power Conf., edited by B. Bernstein and P. Turchi (IEEE, New York, 1987) pp.283-286.

[40] S. Williamson, G.F. Albrecht, and G. Mourou, "Laser Triggered Cr:GaAs HV Sparkgap with High Trigger Sensitivity," *Rev. Sci. Instrum.* **53**(6), 867 (1982).

[41] I.N. Duling III, T. Norris, T. Sizer II, P. Bado, and G.A. Mourou, "Kilohertz Synchronous Amplification of 85-femtosecond Optical Pulses," *J.Opt.Soc.Am B* **2**, 616 (1985).

CHAPTER 2

CHARACTERIZING THE OPERATION OF A HIGH-VOLTAGE COAXIAL SILICON SWITCH

In order to investigate the behavior of photoconductive switches under high bias conditions, a switching circuit capable of repeatedly delivering voltage pulses of 20-30 kilovolts was constructed at LLE. In this chapter we will review the construction of the switching circuit and the use of fast capacitive probes and electro-optic sampling in characterizing the operation of a silicon switch.

I. SWITCHING CIRCUIT

1. HIGH VOLTAGE PULSER

Fig.2.1 shows schematically the switching apparatus consisting of a high voltage bias pulser, charge resistor, switch holder and switch, load resistor, and associated connecting cables.

A high-voltage pulser capable of supplying pulses of up to ~50 kV with a rise time on the order of 100 ns at a pulse repetition rate of several hundred Hz was designed and constructed based on an EG&G HY-31 thyratron. The thyratron output is capacitively coupled to a trifilar wound toroidal transformer which steps-up the output by a factor of two. The whole assembly is immersed in silicon oil (Dow 361) to prevent breakdown at high voltages, and an external supply provides a heater and reservoir current to the thyratron. The pulser driver fires the thyratron grid by amplifying an input TTL electrical trigger to the requisite level (~800V). An internal, resistive, attenuating (x~920) probe is connected to the pulser output so that the

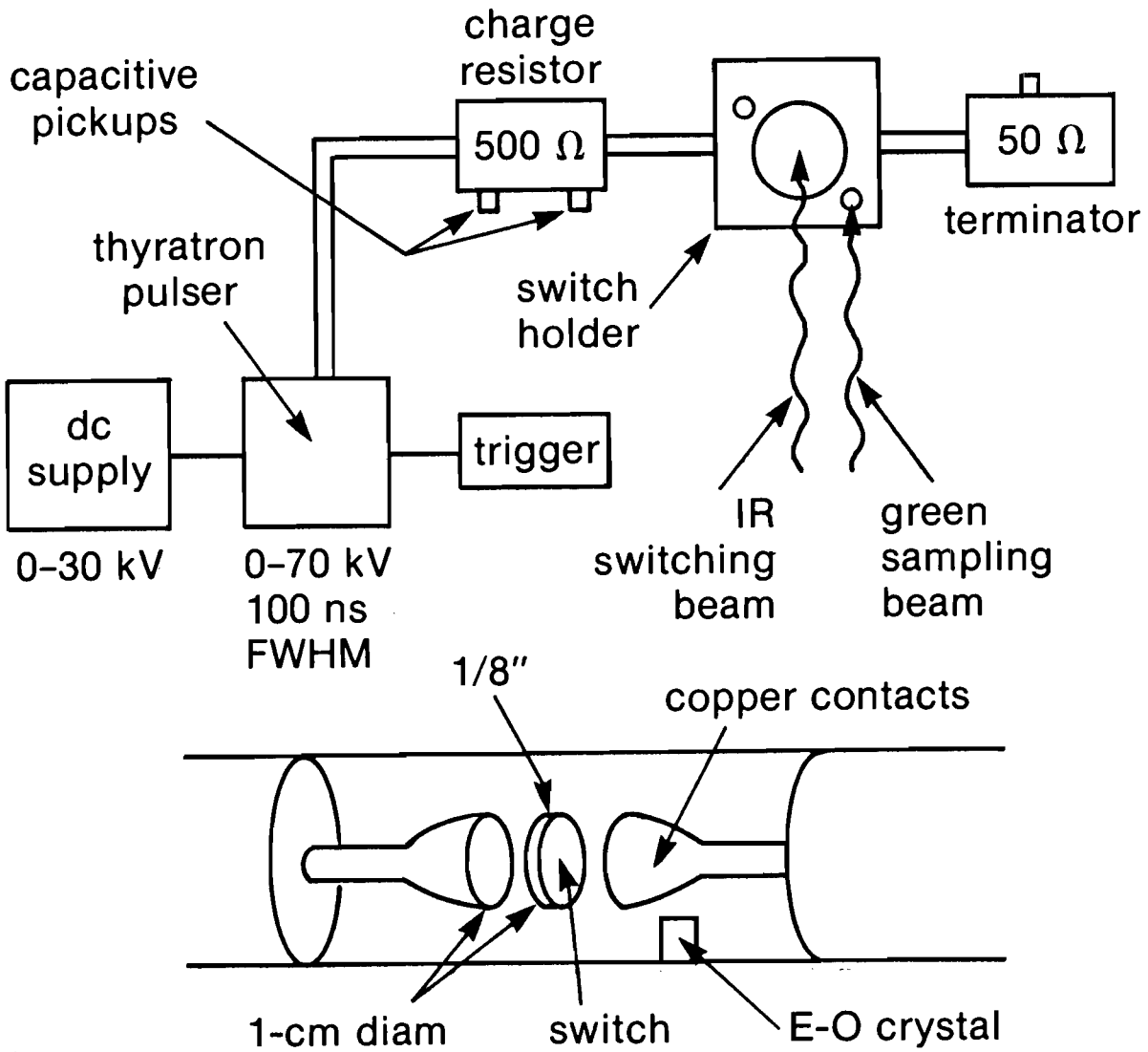

Fig.2.1 Schematic of high-power switching circuit. (a) Entire circuit showing major circuit components. (b) Switchholder detail.

output pulse can be monitored. The output pulse, which is negative, is shown in Fig.2.2. The rise time of the pulse is ~100 ns, and the pulse duration is ~200 ns. The pulser was designed for 25 kV DC input and could deliver an output of 50 kV. It was operated typically at an output voltage of 20 kV, as the other circuit components could not hold off higher voltages. A repetition rate of 50 Hz-100 Hz was set by the thyratron DC power supply.

2. TRANSMISSION LINE &ASSOCIATED COMPONENTS

The pulser output is connected through an RG218 coaxial cable using modified LC connectors to the charge resistor, to the switch holder, and the termination . RG218 cable has an overall diameter of 1 in. with a 3/16 in.(~4.5 mm) diameter solid copper center conductor, a capacitance of 30 pF per foot and an impedance of 50 Ω. All components are designed to maintain coaxial geometry and 50 Ω impedance with a minimum of discontinuities for optimal pulse propagation. The equivalent switching circuit is shown in Fig.2.3. The actual bias voltage applied to the switch is .68 of the pulser output because there is an effective capacitive-resistive divider between the pulser and the switch, as can be seen in the figure. This is due to the reactance of the cable between the charge resistor and switch holder. The output pulse from the pulser,~200 ns wide, can be considered as half of a sinusoid with frequency $\omega = 1.57 \times 10^7$ Hz. The 60 pF capacitance of the cable has a reactance of 1062 Ω at this frequency. The divider is such that 1062 Ω/(1062 Ω+ 500 Ω) = .68 of the pulser output arrives at the switch. Switch biases quoted in later sections are actual voltage at the switch.

The 500 Ω charge resistor is a .75 in. diameter, 5 in. long carbon cylinder housed in an aluminum cylinder, 4.5 in. diameter coaxial with the resistor. Modified LC connectors are used. The cylindrical charge resistor body was filled with Dow

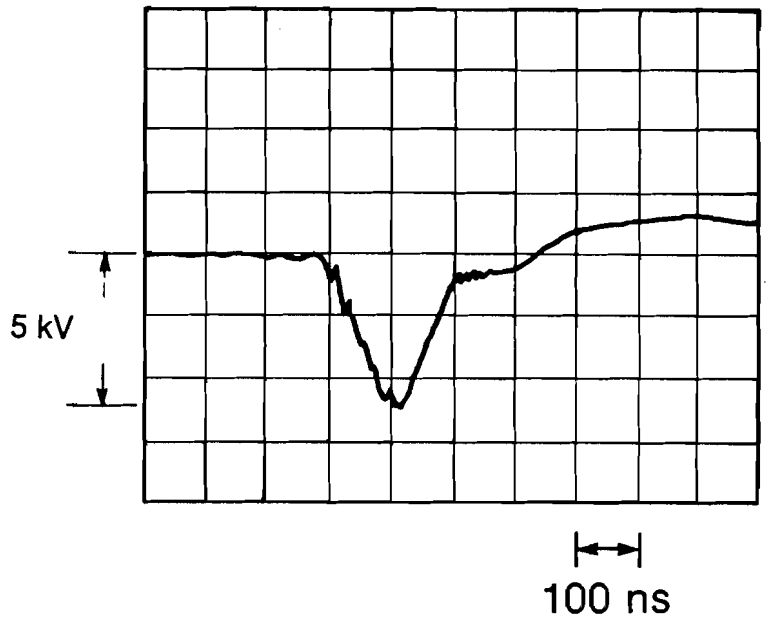

Fig.2.2 High-voltage thyratron bias pulser output voltage measured with internal resistive probe.

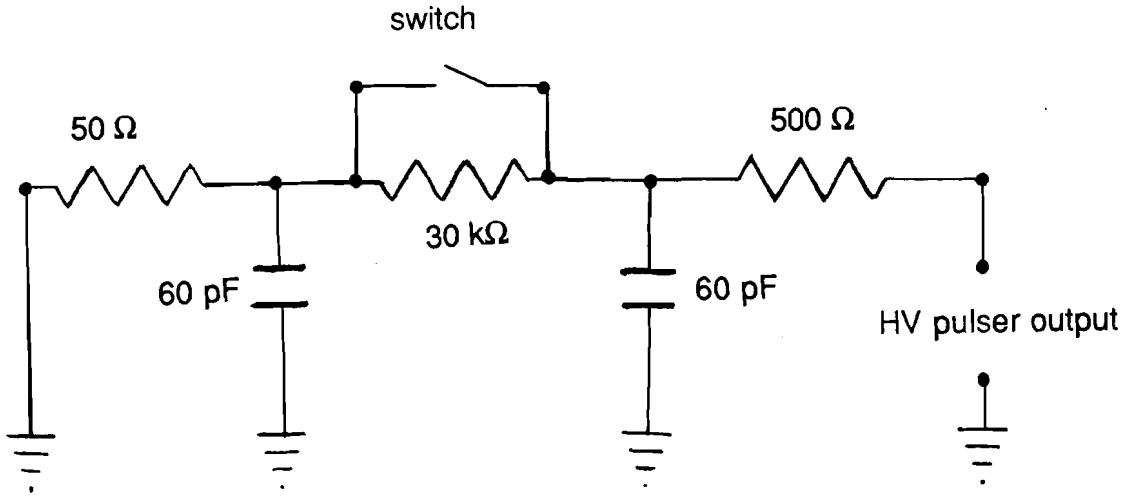

Fig.2.3 Equivalent switching circuit.

361 silicon oil for breakdown prevention. The charge resistor isolates the pulser from the rest of the circuit. A 500 Ω impedance in a transmission line with a characteristic impedance of 50 Ω has a reflection coefficient , r, of :

$$r = \frac{500\ \Omega - 50\ \Omega}{500\ \Omega + 50\ \Omega} = .82 \quad . \qquad [1]$$

The charge resistor will provide the pulser with 82% isolation from back-reflected high-voltage pulses.

In the circuit, the switch bridges a break in the center conductor of the RG218 cable between the charge resistor and the load impedance as shown for the coaxial switch geometry in Fig.1.9(c). The switch is a 1 cm diameter, 3 mm (~1/8 in.) thick right circular cylinder of silicon. The faces of the Si cylinder are gold coated for contact to the switching circuit. The switch was manufactured by Amorphous Materials. RG218 is brought into the holder through modified LC connectors. The center conductor of the RG218 is connected to the circular end faces of the switch via machined copper electrodes which smoothly taper from the 1 cm switch diameter to the 4.5 mm center conductor diameter. The electrodes are spring-loaded and press firmly against the switch end faces for a good electrical contact. Windows in the holder allow laser light to illuminate the switch. The windows and connectors are sealed with gaskets so the switch holder can be filled with Dow 361 silicon oil to suppress arcing from the electrodes to the Al switch holder body. Time domain reflectometry has shown that the switch holder blends smoothly into the 50Ω transmission line.

The off-state resistance of the switch was measured to be 30 kΩ (yielding ρ = 2.5 x 10^4 Ω cm). The cylindrical circumference of the switch was polished to an optical finish to facilitate transmission of the optical excitation pulse into the bulk of

the switch. The switch holder is shown schematically in Fig.2.1(b) and a detailed drawing is shown in Fig.2.4.

The load is designed to terminate the transmission line with a minimum of reflections and could safely handle voltage pulses >20 kilovolts without breakdown. This termination consists of a 1 in diameter, 6 in long cylindrical carbon resistor surrounded by a coaxial aluminum ground. The distance from the resistor to the ground shield varies logarithmically with distance along the resistor to maintain 50 Ω geometry. Like the other components, the load termination can be filled with silicon oil. Fig.2.5 shows the termination in detail.

3. CAPACITIVE PROBES

A. Design

To characterize the operation of the switch, capacitive probes were installed at various points of the circuit. Indirect connection to the circuit was necessary due to the high voltages present during operation; these probes allow viewing the switched waveforms with a response time of ~1 ns or less.

The probes were installed in the charge resistor and load termination and were made from modified BNC feedthroughs as follows (see Fig.2.6). A .75 cm diameter circular brass plate connected to the center conductor of the BNC feedthroughs served as the capacitive pick-up. The feedthrough was installed in the charge and load resistors with the brass plate flush with, but not touching the grounded coaxial Al case surrounding the carbon resistors. Voltage pulses traveling along the coaxial transmission line induce charge on the brass plate, appearing as a

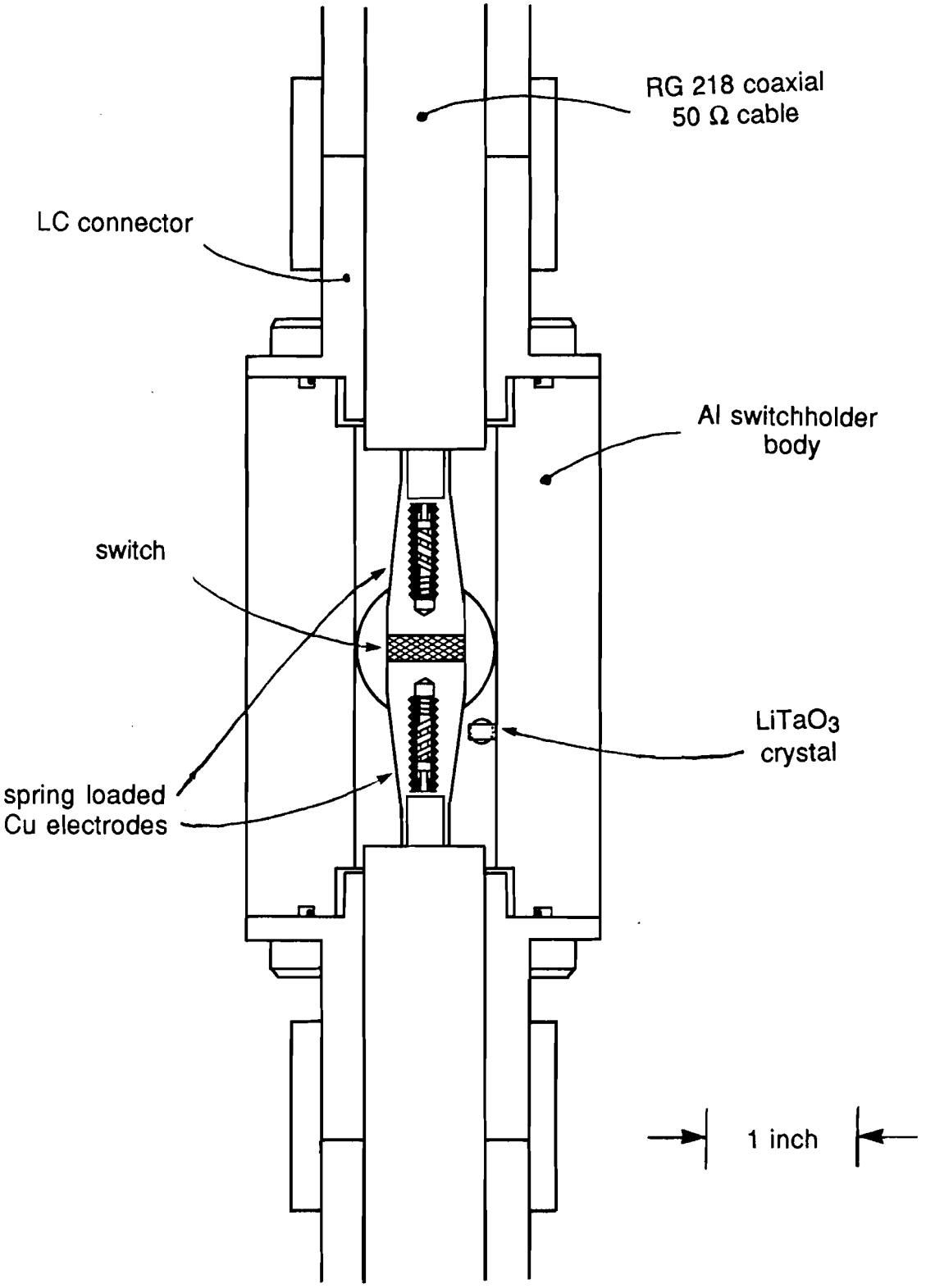

Fig.2.4 Switchholder mechanical detail showing switch, electrodes, connectors, and electro-optic sampling crystal. The switch holder is shown actual size.

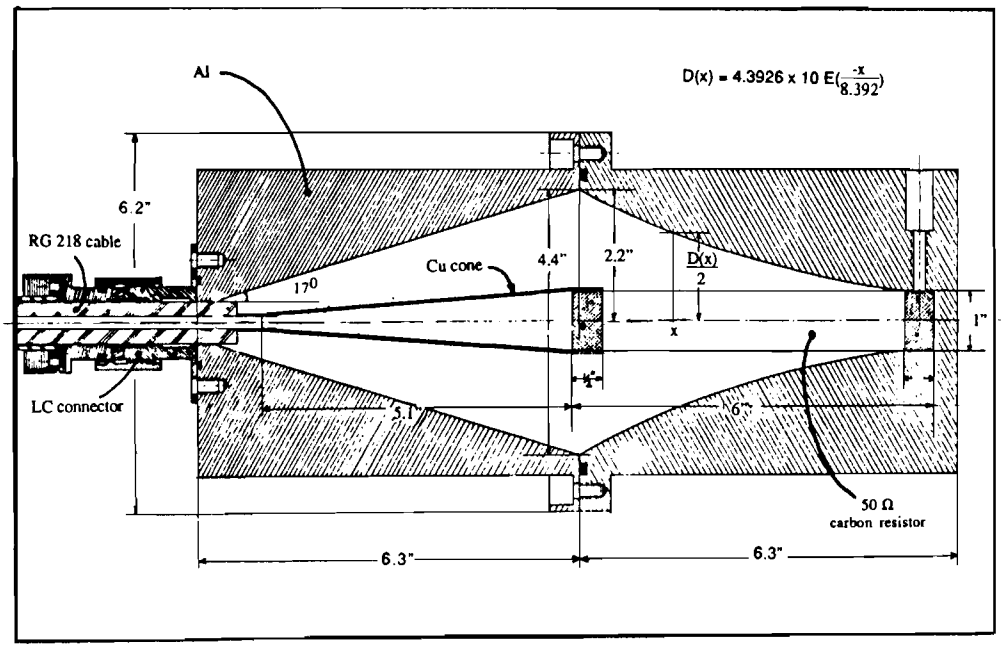

Fig.2.5 Load termination detail. The overall length of the resistor housing is 1.5 ft. This drawing does not show capacitive probes.

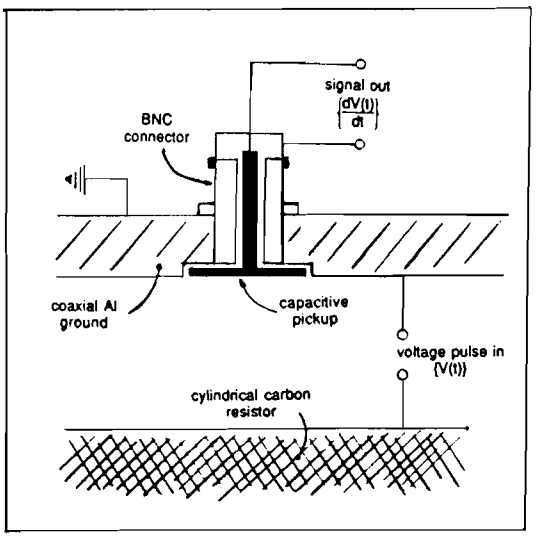

Fig.2.6 Capacitive probe assembly sketch. The probe is a modified BNC connector.

voltage at the BNC feedthrough output which is proportional to the derivative of the signal in the transmission line.

To calibrate the probes, the RG218 cable connecting the switch holder to the load termination was pulsed with a reference pulse of known amplitude and the output of the load probe was recorded with an oscilloscope. Similarly, the RG218 cable connecting the switchholder to the charge resistor was pulsed with a reference voltage pulse and the charge 1&2 probe signals were recorded. The probes were calibrated for both high and low voltages.

For the low voltage calibration, an SRS DG535 digital pulser was used to pulse the line at voltages up to about 40V. For the high voltage calibration, the RG218 cables were reconnected to the switch holder and the silicon switch was replaced with a copper disk so that the high-voltage pulser was connected through the charge resistor directly to the load termination. In addition, the voltage pulse delivered to the load was measured at the copper surrogate switch with a commercially available high-voltage probe. The use of this commercial probe is not possible during the actual photoconductive switching of the circuit. The probe outputs were recorded for various voltages. A typical probe output trace is show in Fig 2.7.

Since the probes give the derivative of the input pulse, the area under the probe output is proportional to the peak voltage. This was calculated for the load probe and is plotted versus applied voltage in Fig.2.8. The data indicate that the load probe response is .9 ns-mV per input volt.

To measure the switched voltage pulse, an HP digital scope #54201 was used to digitize the probe output. This digitized data was transfered to a personal computer,

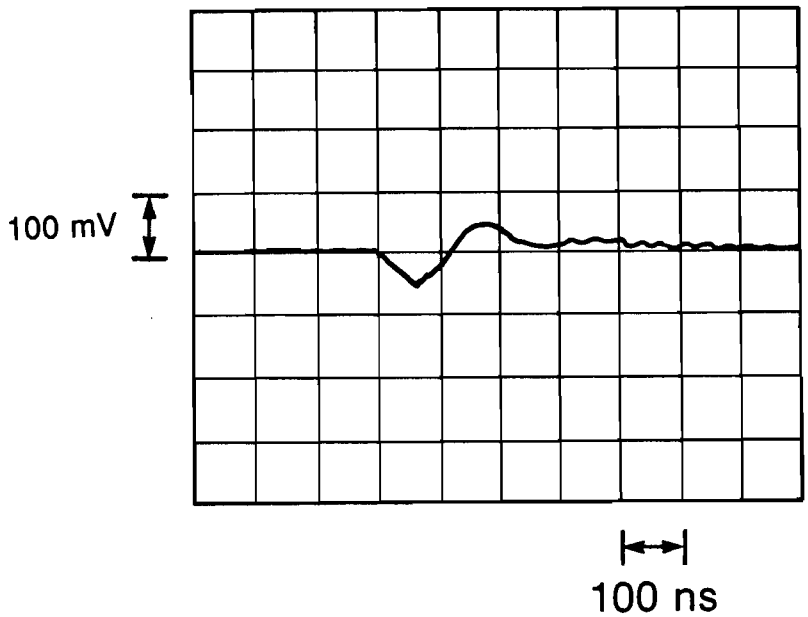

Fig.2.7 Typical output pulse from the capacitive probe. The area under the trace is proportional to the signal voltage.

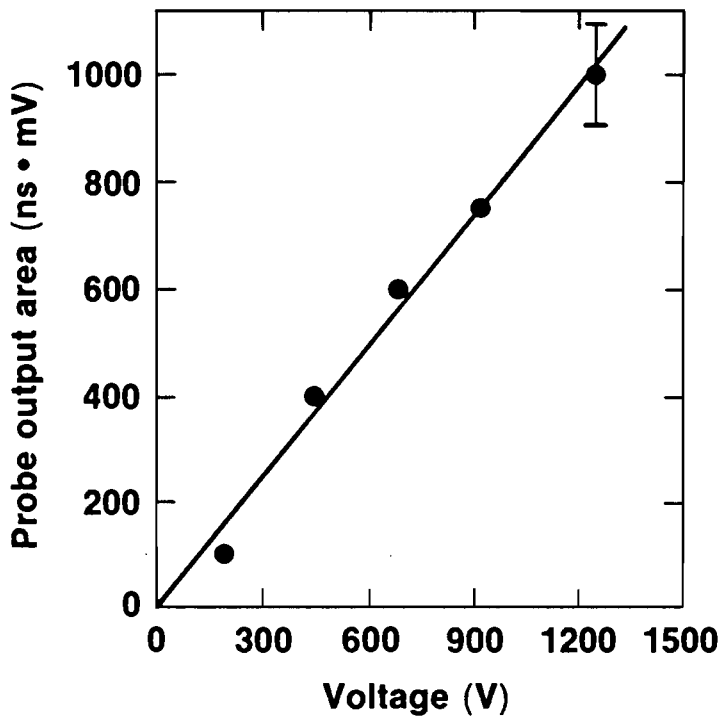

Fig.2.8 Capacitive probe calibration curves for the load probe for high voltage calibration.

where the differential output was numerically integrated. The probe calibration was used to scale these integrals.

B. Switching Data and Analysis

The capacitive probe-computer acquisition system was used to monitor the load probe during photoconductive switching. The switch was illuminated with laser light from the Nd:YAG regenerative amplifier (λ = 1064 nm). Data was taken for laser pulse energies of 25 μJ, 75 μJ, and 150 μJ, and for various applied bias voltages. Switched waveforms for various optical pulse energies and constant bias voltage of 12 kV are shown in Fig.2.9. Switched waveforms for different applied bias voltages at a constant applied optical pulse energy of 150 μJ are shown in Fig.2.10.

The switched voltage waveforms in Figs.2.9&2.10 display some interesting characteristics. All the waveforms are a "staircase", i.e., a large peak (more negative) followed by a series of smaller plateaus, due to a mismatch between the charge resistor and the coaxial cable. The width of these plateaus is twice the length of the charge line, i.e.,twice the transit time of the RG218 cable between the charge resistor and the switch. From Eq.1.8, the maximum voltage is switched to the load when R_s = 0. In this case, V_L, for Z_s=Z_L= 50Ω, is

$$V_L = \frac{Z_L}{Z_L+Z_s+R_s} V_{BIAS} = \frac{50\Omega}{100\Omega} V_{BIAS} = \frac{V_{BIAS}}{2}.$$

The bias pulser charges the RG218 cable between the charge resistor and the switch to the bias voltage. When the switch is closed by the light pulse, a voltage pulse equal in height to half the bias voltage is launched towards the load, assuming near perfect switching (R_s< 1 Ω). A second pulse, equal to - $\frac{V_{BIAS}}{2}$, is launched in

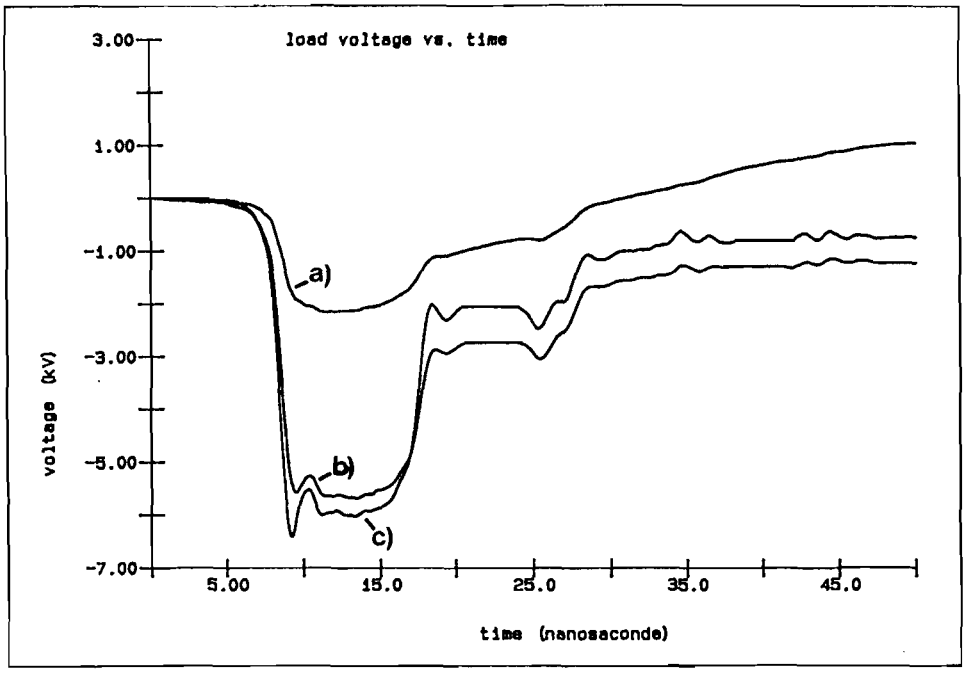

Fig.2.9 Switched voltage waveforms at a constant bias of 12 kV for various optical energies measured with capacitive probe. (a) 25 μJ; (b) 75 μJ; (c) 150 μJ. The temporal resolution is ~1 ns.

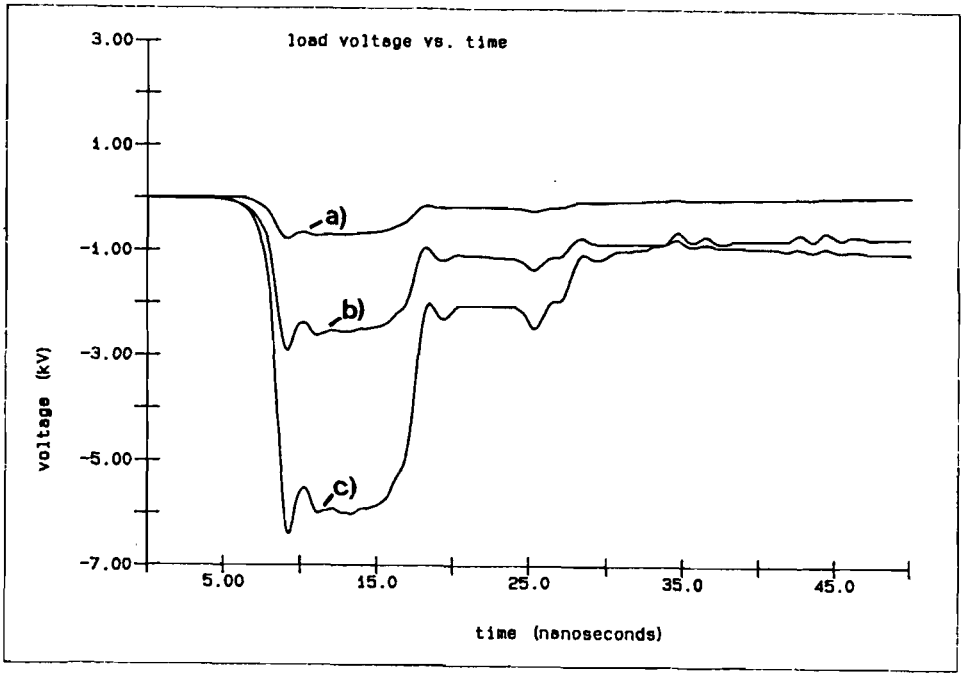

Fig.2.10 Switched voltage waveforms at a constant optical energy of 150 μJ for various bias voltages measured with capacitive probe. (a) 1.1 kV; (b) 5.1 kV ; (c) 12 kV. The temporal resolution is ~1 ns.

the opposite direction towards the charge resistor. 82% of this pulse changes sign and reflects from the 500 Ω charge resistor back towards the switch. This will produce a secondary pulse of height

$$(1\text{-}.82)\,\frac{V_{BIAS}}{2} = .18\,\frac{V_{BIAS}}{2}$$

which will be delivered to the load. Further reflection from the small, yet finite, switch resistance will lead to tertiary pulses, etc., until the charge line is depleted of charge. This will cause the staircase effect that is observed in the switched waveforms.

The switch resistance, and , thus, the voltage switched to the load will depend on the optical energy, as given by Eq.1.6 and Eq.1.8. This is seen in the data shown in Fig.2.9, where the switched voltage varies with applied optical energy. At 25 μJ optical energy, 2 kV of the applied 12 kV bias is switched. This is 2 kV out of a possible 6 kV (6 kV = 12 kV/2), or 33% efficiency. For 75 μJ and 150 μJ applied optical energy, the efficiency is near 100%, the switch having reached saturation efficiency somewhere between 25 μJ and 75 μJ of applied optical energy. In Fig 2.10, the efficiency is near 100% for each waveform. The staircase step height is not the expected 18% of the first step, but is ~30%. This discrepancy is not surprising, as it was assumed, as a first guess, that the impedance of the charge resistor assembly was equal to its DC resistance of 500Ω. The switching data indicates that the charge resistor assembly impedance is ~283 Ω.

The switched voltage waveforms in Figures 2.9 and 2.10 have rise times of ~1 ns. This is the limit of resolution obtained with the HP digital scope and capacitive probe combination. It was not possible to achieve subnanosecond response with

these probes. To observe the rise time on a finer time scale, the switched waveforms were measured electro-optically.

II. ELECTRO-OPTIC SAMPLING

The electro-optic effect is the phenomenon whereby the birefringence of certain crystals is altered by an applied electric field. This is often called the Pockels effect after F. Pockels, who first studied the effect in 1893. The electro-optic effect can be viewed as the mixing of an applied electric field and an optical field inside a crystal to produce a new optical field whose polarization is rotated with respect to the incident optical field. Crystals exhibiting this effect, of which there are hundreds, are termed "electro-optic" crystals. Commonly used electro-optic crystals are lithium tantalate ($LiTaO_3$), lithium niobate ($LiNbO_3$), and potassium dihydrogen phosphate (KDP). We will now briefly review the origin of the electro-optic effect and describe, in general, how the Pockels effect is utilized in electric field measurements.

1. BASIC PRINCIPLES OF ELECTRO-OPTIC SAMPLING

A review of the fundamental physical basis of the Pockels effect has been given by Yariv [2]. The original work on ultrafast, electro-optic sampling was done by Valdmanis, who describes in great detail the practical application of the Pockels effect in the measurement of subpicosecond electrical transients [3] .

A. Physical Origin

In a birefringent crystal, the optical properties of the crystal are not the same in all directions. The physical cause of birefringence is asymmetry in the crystal lattice, so that the binding force of an electron at a lattice site is not equivalent for all directions of oscillation. The response of an electron to an optical oscillation, $\mathbf{E}e^{i\omega t}$,

will depend on the orientation of E. This anisotropy in the binding force manifests itself in an anisotropy in the crystal's index of refraction which can no longer be represented by a single scalar constant, but, instead, is a tensor quantity. The index of refraction can be depicted as an index ellipsoid, or index "indicatrix", which uses six scalars, n_i (i=1-6), to depict the anisotropic index properties. The general equation of the index ellipsoid in an arbitrary cartesian coordinate system is

$$\frac{x^2}{n_1^2} + \frac{y^2}{n_2^2} + \frac{z^2}{n_3^2} + \frac{2yz}{n_4^2} + \frac{2xz}{n_5^2} + \frac{2xy}{n_6^2} = 1. \tag{2.2}$$

with the subscripts 1-6 being the reduced form of the cartesian coordinates: 1=xx,2=yy, 3=zz, 4=yz,5=xz,6=xy [3]. Any plane cross section of this ellipsoid will be an ellipse. Consider an arbitrary direction of propagation for a light wave in a crystal with an index ellipsoid described by Eq.(2.2). The major and minor axes of the plane cross section of the ellipsoid perpendicular to the direction of propagation are proportional to the indices experienced by light waves polarized along these same axes. If the cross section is a circle, the crystal appears symmetric along this direction and all polarizations of light propagate with equal speed. For a given crystal, there is either one, two, or an infinite number of directions along which the plane cross section of the index ellipsoid is a circle. Most common electro-optic crystals are uniaxial, having a unique direction termed the "crystal axis".

Consider the propagation of a beam of polarized laser light through a birefringent crystal, as sketched in Fig.2.11. The initial polarization state of the laser beam can always be considered to be the sum of two orthogonally polarized components. Propagation along any direction other than the crystal axis will result in a phase difference between the two polarization components when the light exits the crystal. Upon exit, these components will, in general, not add up to the original

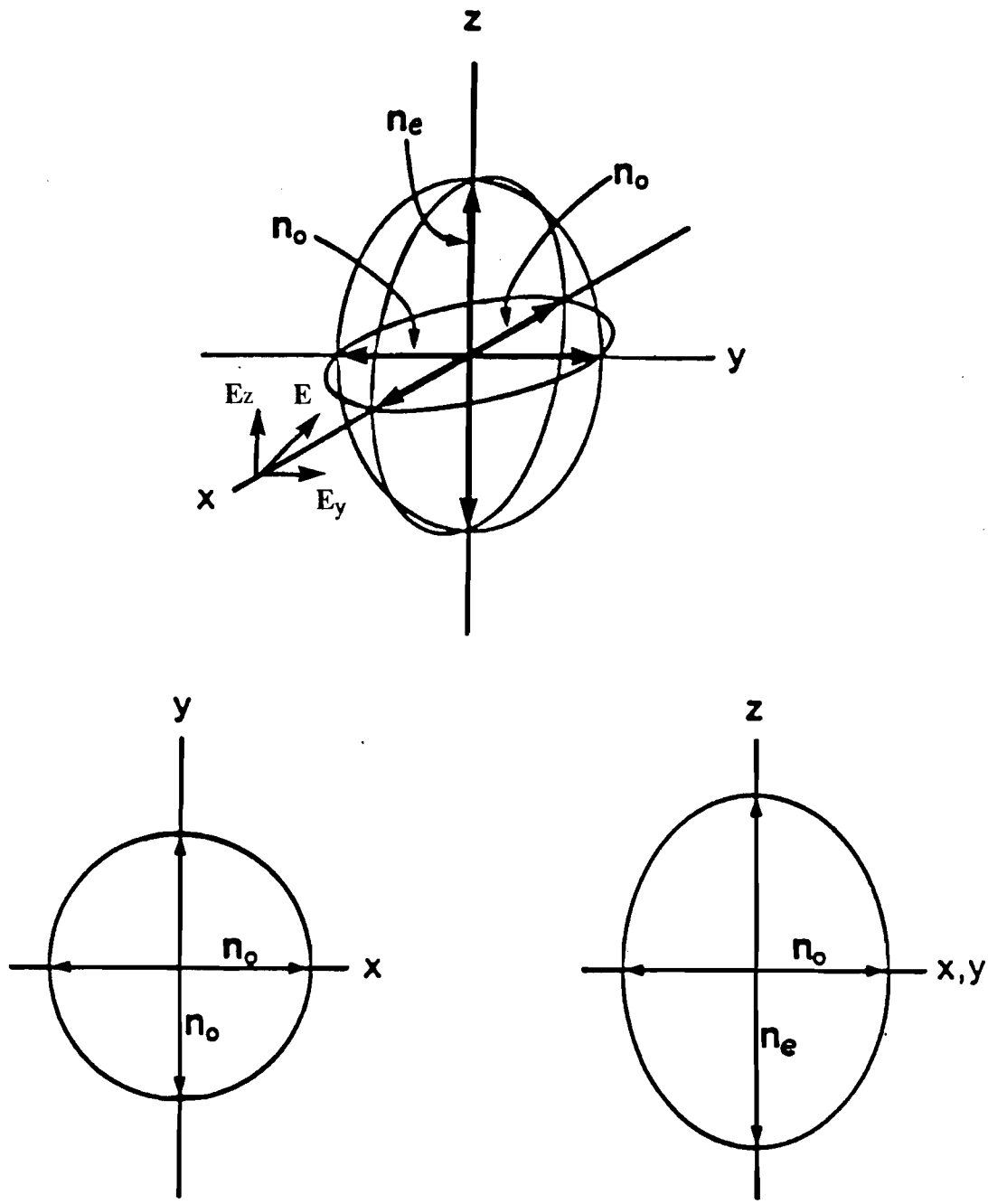

Fig.2.11 Propagation of an optical wave in a birefringent crystal. The index ellipsoid is shown. The cross section of the ellipse in the xy plane is a circle: the z-axis is the crystal axis. The optical wave propagates along the x-axis. The plane cross section in the zy plane is an ellipse: E_z and E_y will experience different indices of refraction, n_e (extraordinary index) and n_o (ordinary index) respectively.

polarization state of the incident beam so that the polarization state of the output optical beam has been rotated with respect to the incident optical beam by traversing the birefringent crystal. This property of birefringent crystals, the ability to change the polarization state of a beam of light, is the basis for various optical components, including polarizers and waveplates. A comprehensive review of the propagation of light in birefringent crystals has been given by Yariv and Yeh [4].

An electric field applied to a crystal can displace ions and electrons bound to the lattice from their equilibrium positions, producing electric dipoles, the macroscopic manifestation of this being electric polarizability. As a result, the electron binding force and, hence, the index of refraction of the crystal can be altered, inducing or altering existing birefringence in the crystal. The linear electro-optic effect is the change in the indices that is caused by an applied electric field and is proportional to its strength. This change of the indices can be viewed as a rotation of the index ellipsoid. This index change will depend on the orientation of the crystal with respect to the applied electric field. The change in the index indicatrix element, n_i, due to the applied electric field, E, is given by

$$\Delta\left(\frac{1}{n_i^2}\right) = r_{ij} E_j \qquad [5] \qquad (2.1)$$

where i = 1,2,3,4,5,6 and j =1,2,3. j refers to the Cartesian axes, x,y,z. r_{ij} is the linear electro-optic tensor (of third rank), which has 3 x 6 = 18 components. Due to crystal symmetry, most of the 18 r_{ij} are zero. The linear effect exists only in crystals that lack a center of inversion symmetry as all third-rank quantities must vanish in systems that possess a center of inversion [6]. The non-zero elements of r_{ij} determine the combinations of light direction and field direction that will produce an electro-optic effect. In general, practically useful electro-optic effect is only obtained with a given

crystal for one or, perhaps, two orientations. For KDP, a popular orientation is for the electric field and light direction to lie along the optic axis. For $LiTaO_3$, the electric field is along the optic axis but the light propagation is perpendicular to the optic axis. Fig.2.12 illustrates the electric field/crystal axis orientation for producing electro-optic effect in $LiTaO_3$.

By electrically inducing or altering the birefringence of a crystal via Pockels effect, it is possible to modulate optical beams by changing their polarization state. Electro-optic modulation is used in many applications, including optical beam deflection, fast optical shutters, and laser Q-switching; it can also be used for the optical detection of electric fields.

B. Electro-Optic Field Measurement

The basic principles of electro-optic field measurement are outlined in Fig.2.13. To measure a signal voltage, V, an electro-optic crystal is placed between two parallel plates and the signal is applied to the plates. The plates have a hole to allow a polarized laser probe beam to traverse the crystal. For the particular, longitudinal, geometry illustrated KDP would be an appropriate electro-optic crystal, but the analysis is the same for the transverse, $LiTaO_3$ geometry. The probe beam traverses two crossed polarizers, between which the crystal is placed. Alternately, in a reflection geometry, the beam traverses the same polarizer after being reflected from the back surface of the crystal. The linearly polarized optical probe beam passes through the crystal, and the electrically induced birefringence due to the signal voltage, V, rotates the beam's polarization which, therefore, allows transmission through the analyzing polarizer and is detected by the photodiode. The light intensity through the second polarizer is a measure of the electric field present in the crystal, and is given by

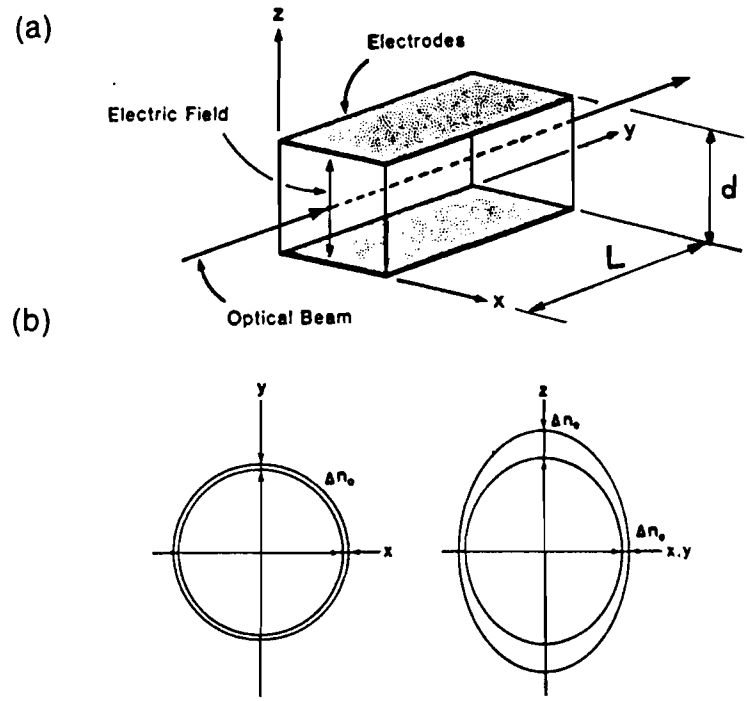

Fig.2.12 a) Electric field, probe beam, and crystal alignment for producing electro-optic effect in $LiTaO_3$. This is called the transverse sampling geometry. b) The change in the indicatrix of the $LiTaO_3$ crystal induced by the applied electric field.(after ref.[3])

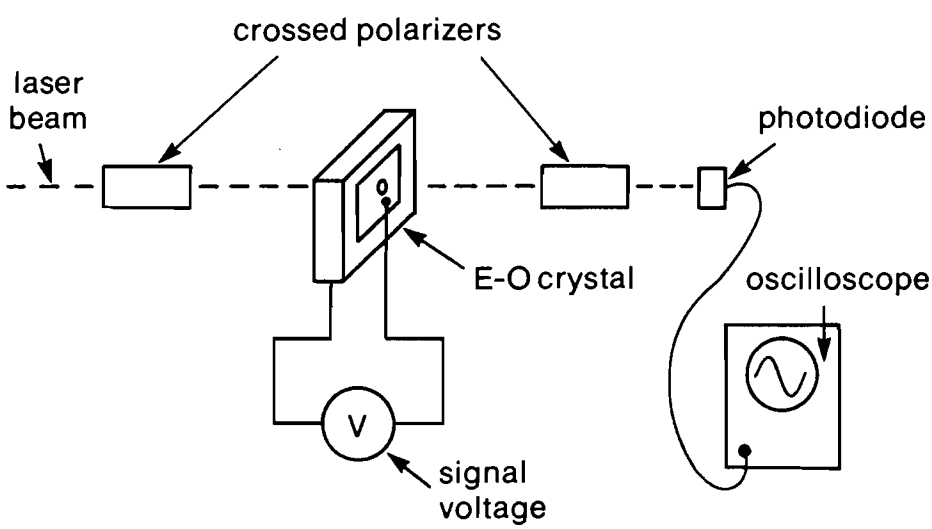

Fig.2.13 Set-up for electro-optically measuring an electric field. The electro-optic crystal is placed between two crossed polarizers. The applied electric field modulates the probe beam intensity measured at the detector.

$$I(V) = I_0 \sin^2(\alpha V + \beta) \tag{2.3}$$

where I_0 is the initial laser probe beam intensity and the argument of the sine function is the total rotation experienced by the beam as it propagates between the two polarizers. The total rotation has two components: a static, or non-electrically induced component, β; and an electrically induced component, αV. α is a constant which relates the electro-optic coefficient to the applied electric field and whose value depends on material parameters, optical path length in the crystal, electrode geometry, and wavelength of the optical probe beam. β may include rotation due to static birefringence in the crystal or rotation introduced by other optical elements in the beam path.

The unknown voltage, V, can be determined from a measurement of the transmissivity, $I(V)/I_0$ using Eq.(2.3), if the constants α and β are known. For the simple case illustrated, α can be calculated, but it is usually determined by an experimental calibration, using known applied voltages. The value of β in Eq.(2.3) can be adjusted to produce the optimum system response by inserting a waveplate in the probe beam path.

The parallel plate capacitor/crystal arrangement of Fig.2.13 is an electro-optic modulator. A useful figure of merit for an electro-optic modulator is the half-wave voltage, V_π, of the modulator, which is the voltage that need be applied to the modulator electrodes to rotate the polarization plane of a linearly polarized probe beam by $\pi/2$, or, equivalently, for the two orthogonal components of the probe beam to acquire a phase difference of π radians and achieve 100% intensity modulation. V_π is related to the constant α of Eq.2.4 by

$$\alpha = \frac{\pi}{2V_\pi} \cdot \qquad [2] \tag{2.4}$$

V_π for $LiTaO_3$ in the transverse geometry pictured in Fig.2.12 is given by

$$V_\pi = \frac{\lambda}{(n_e^3 r_{33} - n_o^3 r_{13})} \frac{d}{L} \qquad [3]$$

where λ is the free space wavelength, n_o and n_e are the ordinary and extraordinary indices of refraction, and r_{13} and r_{33} are the appropriate electro-optic tensor elements. For λ= 532 nm, V_π = (2323 V) $\frac{d}{L}$. For KDP,in the longitudinal geometry, V_π is independent of crystal size and for λ= 532 nm, V_π = 7.3 kV. The response of an electro-optic intensity modulator is shown in Fig.2.14.

Time-varying, or transient, electric fields, such as the output of a photoconductive switch, can be sampled using the electro-optic effect. If the optical probe is a pulsed laser, the birefringence of the crystal will only be sampled during the time the pulse is present in the crystal, i.e., the electric field measurement is "gated" by the laser probe pulse width and makes possible temporally resolved electric field measurements. A transient electric field is determined by measuring the instantaneous value of the electric field for various gate delays, taken at regular intervals to span the entire waveform. Gate delay is provided by optically delaying the laser probe pulse. The temporal resolution of the measurement is determined only by the probe laser pulse width as the physical mechanism responsible for the electro-optic effect, electric polarizability, is extremely fast. The intrinsic ability of an electro-optic modulator to respond to ultrafast electrical transients is limited by crystal absorption to about 10 THz, or time scales of tens of femtoseconds [3]. Practical limits are imposed by the modulator's electrical response time and the transit time of the sampling beam through the crystal. Using ultrafast lasers, picosecond and subpicosecond time scale measurements of transient electric fields have been demonstrated [7,8].

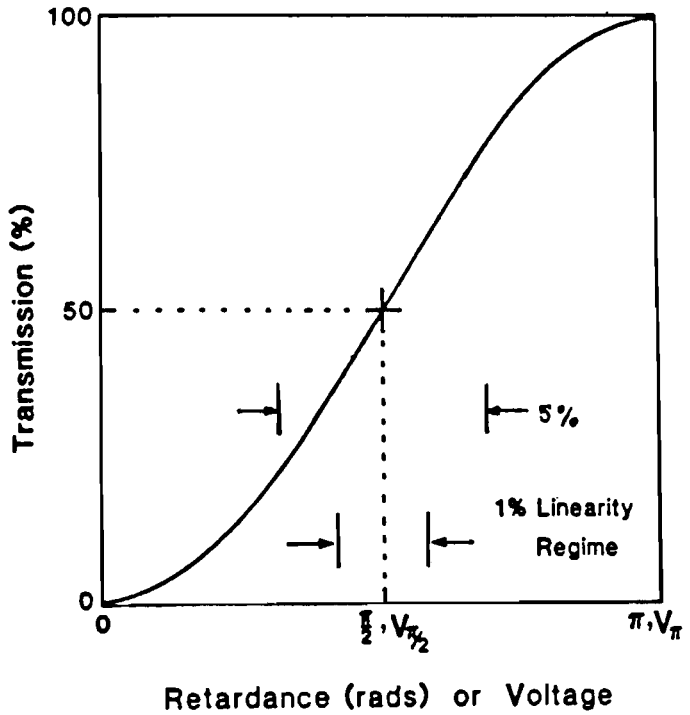

Fig.2.14 Response of electro-optic intensity modulator to applied voltage. The curve is given by Eqs.(2.3) & (2.4). The curve is quasi-linear at $V_{\pi/2}$. The regions of 5% and 1% deviation from linear response are indicated. In these regions the intensity change is essentially proportional to the applied voltage.(after ref.[3])

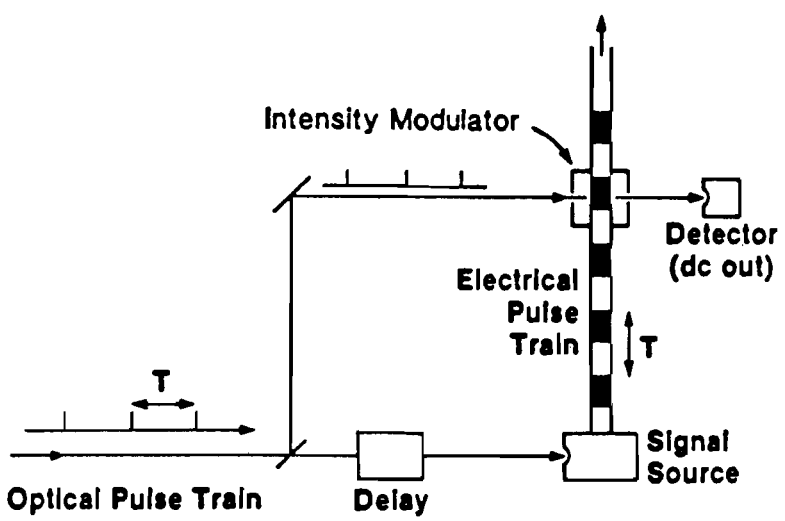

Fig.2.15 Basic principles of electro-optic sampling. Optical pulse train repeatedly samples photogenerated electrical pulse train in electro-optic modulator. Optical and electrical pulses are in complete synchronization: there is no jitter. Optical delay can be inserted in either the pump or probe beam.(after ref.[3])

To use the sampling technique, the electrical pulse that is to be measured must be synchronized to the optical probe pulse train. For photogenerated electrical signals, the optical excitation and probe pulses trains are derived from the same laser pulse train using an optical splitter and are , therefore, in synchronization: this is refered to as an optical "pump and probe" arrangement. The general principles of electro-optic sampling are shown schematically in Fig.2.15.

The electro-optic modulator and test set-up shown in Fig.2.13 is idealized. It is not always possible or necessary to arrange the electro-optic crystal and the electric field to be in perfect orientation. In practice, the field to be measured may not be spatially uniform as between the two capacitor plates. Also, it is not always possible or desirable to connect the fast electrical transient to an external electro-optic modulator for characterization as this may introduce connector and cable effects which can degrade an ultrafast electrical signal. In practice, the electro-optic crystal is placed as close as possible to the signal source and the crystal is oriented to produce maximum electro-optic effect for the given electrode geometry. As the electrical signal may be weak and/or the field configuration may be less than ideal, i.e. V_π for the modulator may be quite large, the modulation imposed upon the optical probe beam may be quite small. It is, therefore, often necessary to average over many probe pulses at each delay position and for very weak signals, phase sensitive techniques must be employed.

The electro-optic sampling technique is especially suited for measuring the switched output of high-bias photoconductive switches as demonstrated by Auston and LeFur [9] and Mourou and Knox [10], who used Pockel cells to measure picosecond kilovolt electrical pulses.

2. ELECTRO-OPTIC RISE TIME MEASUREMENT

A. Experimental Arrangment

The switch holder, shown in Figs.2.1(b) and 2.4,.was designed to facilitate the use of electro-optic probes. A y-cut $LiTaO_3$ crystal, 4 x 3 mm, .5 mm thick, was glued to the aluminum switchholder body directly below the tapered copper electrode on the load side of the Si switch, 5 mm from the switch. The crystal was, thus, immersed in the electric field of the switched pulse. In this arrangement, the $LiTaO_3$ crystal axis is parallel to the radial electric field of the coaxial geometry switchholder and the orientation is appropriate for transverse electro-optic sampling. An optical probe beam of 532 nm light can enter through a small hole in the holder, traverse the $LiTaO_3$ crystal and exit the holder through a small hole in the opposite side. The crystal is placed as close to the Si switch as practical to minimize signal degradation due to dispersive propagation. The entire electro-optic sampling apparatus is shown schematically in Fig.2.16.

The 532 nm probe pulse train is derived from the infared (λ =1064 nm) switching pulse train by frequency doubling a portion of the infared (IR) beam using second harmonic generation in a KTP ($KTiOPO_4$) crystal. The probe beam passes through the polarizer and half waveplate, enters the switchholder, traverses the $LiTaO_3$ crystal, and then passes through the second polarizer. The crystal is between crossed polarizers and acts as an electro-optic intensity modulator. The transversely polarized component of the transmitted probe beam is rejected by the polarizer and directed to a PIN diode detector. The half waveplate is used to introduce continuously adjustable static birefringence to optically bias the transmission to the detector at the half intensity point for optimum linear response. A variable delay,

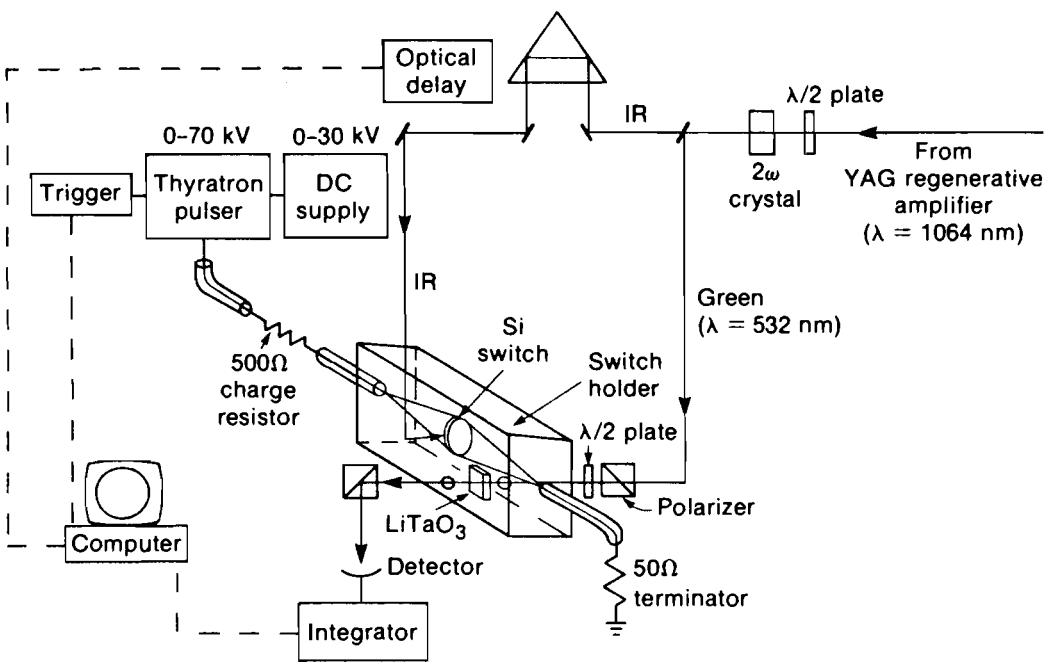

Fig.2.16 Entire switching and electro-optic sampling set-up in schematic.

consisting of a retro-reflector on a stepper motor driven translation stage is inserted in the pump beam path. The fractional electro-optic modulation of the probe beam versus probe delay is measured. This is done by toggling the high voltage bias pulser on and off at each delay position, and measuring the probe pulse height with the diode detector for bias voltage on and bias voltage off. Due to the magnitude of the switched voltage, the intensity modulation of the probe pulse can be clearly seen on an oscilloscope and an example measurement is shown in Fig.2.17. The output of the signal detector is connected to an SRS 250 gated integrator to reduce noise and for signal averaging. The integrator was interfaced with a personal computer, as was the delay stage stepper motor controller and high-voltage pulser, to allow for automated data collection.

The switching circuit was first optimized using the capacitive probes, adjusting the IR pump beam alignment and high-voltage pulser timing for maximal switching to the load resistor. The laser and bias pulser were operated at 67 Hz, both being synchronized to the same electronic oscillator. The laser pulse width was ~100 ps. The optical delay stage was swept through its 1000 ps range in 20 ps steps. At each step, the fractional intensity modulation is measured, averaging 300 laser pulses. This value is recorded by the computer so that a plot of fractional intensity versus optical delay can be made: this maps out the switched voltage waveform.

B. Experimental Results and Discussion

Switched voltage waveforms were measured electro-optically for IR pump pulse energies of 115 μJ, 67 μJ, and 45 μJ at two bias voltages, 13 kV and 19 kV [11]. These bias voltages correspond to applied electric fields of 43 kV/cm and 63 kV/cm, respectively. The optical energy was varied using a half-wave plate and polarizer. The results are shown in Figs.2.18.

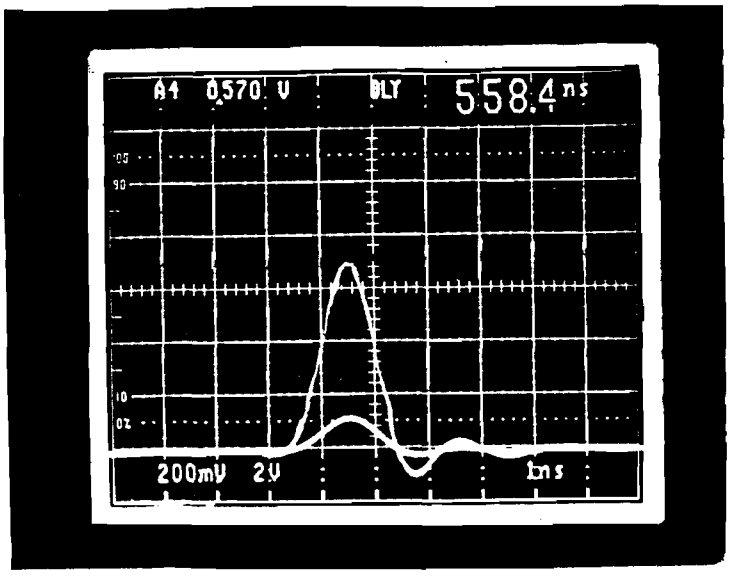

Fig.2.17 Modulation of optical probe pulse due to applied electric field. Oscilloscope trace of probe pulse measured with a diode detector is shown. Lower trace is pulse with bias voltage off; upper trace with bias voltage on. The applied voltage was ~4 kV.

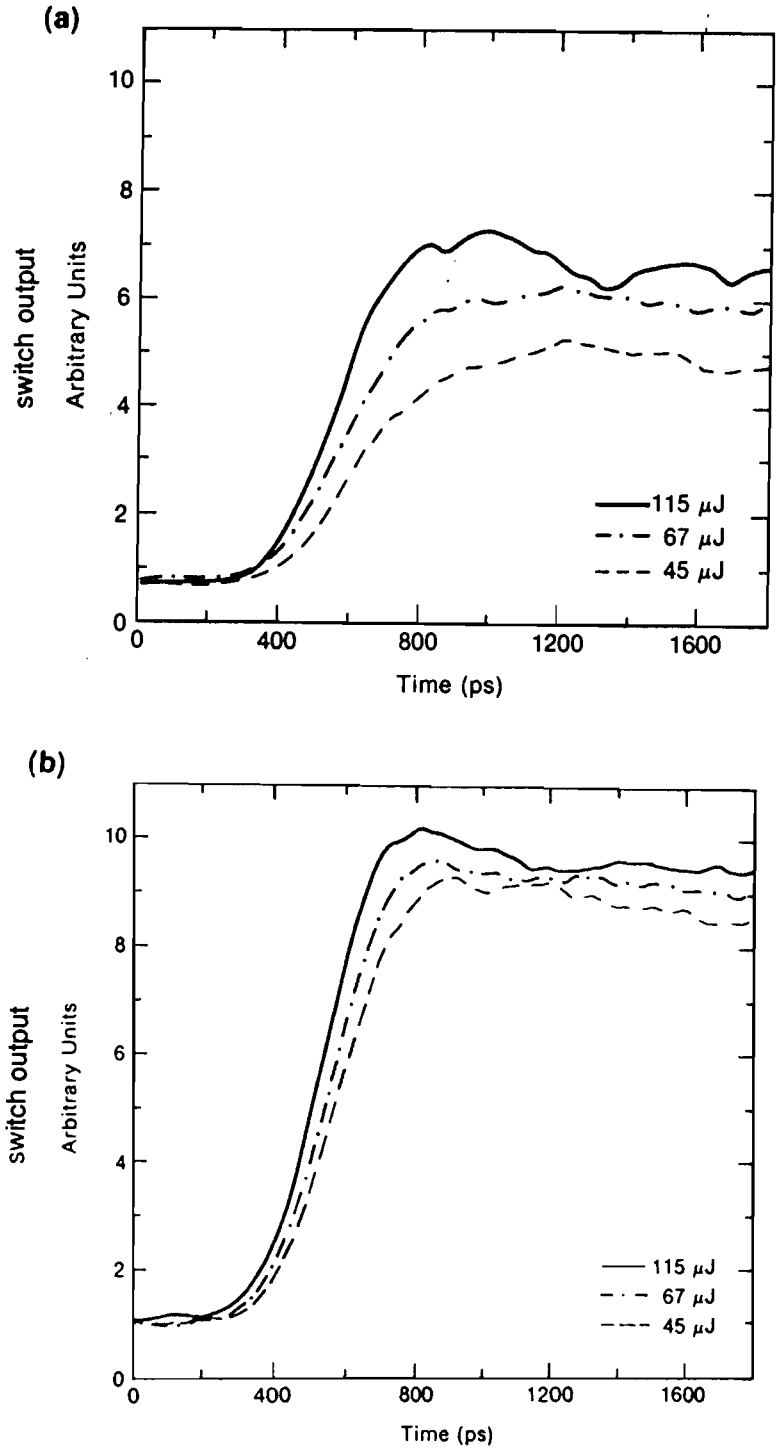

Fig.2.18 Switched voltage waveforms measured electro-optically. Data taken for optical energies of 115, 67, and 45 μJ for bias voltages of a) 13 kV and b) 19 kV.

Table 2.1

Si Switch Electro-optic Rise Time Measurement Results

Laser Pulse Energy	10%-90% Rise Time	
μJ	13 kV bias	19 kv bias
	(43 kV/cm)	(63 kV/cm)
115	277 ps	277 ps
67	370 ps	290 ps
45	390 ps	310 ps
Circuit limited rise time		30 ps
Minimum rise time measurement result obtainable with 150 ps probe		163 ps

The 10%-90% rise times of the waveforms in Fig.2.18 are tabulated in Table 2.1. The measured rise time is greater than the actual waveform rise time by ~ 10% due to the finite sampling pulse width. A trend can be seen in these results. For either bias voltage, the rise time decreases as the optical energy increases. For a given optical energy, the rise time is longer at the lower bias voltage. Fig.2.18 also shows that the peak of the switched voltage pulse shifts to later times with decreasing optical energy at either bias. Switching is more efficient at higher bias. A voltage overshoot is also observed.

These results are not immediately explainable in terms of previously published models of carrier behavior in photoconductive switches. Mourou and Knox [11] presented the following expression for the gap conductance, G(t), as a function of time, valid for bias fields $>10^4$ V/cm,

$$G(t) = \frac{2v_s e\eta}{h\nu \ell V_0} \int_{-\infty}^{t} P(t')dt' \tag{2.4}$$

where, as before, V_0 is the applied bias voltage, v_s is the carrier saturation velocity, e is the electron charge, η is the fraction of absorbed optical pump energy, h is Planck's constant, ν is the optical pump frequency, ℓ is the gap length, and P(t) is the incident laser power. In Eq.2.4, the time dependence of the gap conductance, and hence, the switched voltage, depends only on the integral of the laser pulse intensity. Eq.2.4 does not account for the variation in the time dependence of the gap conductance with applied optical energy which was experimentally observed. The shift of the electrical pulse in time is, however, qualitatively explained by this model.

The analysis that resulted in Eq.2.4 assumed a constant carrier drift velocity, equal to the saturation velocity, throughout the switching process. From the drift

velocity versus field curve in Fig.1.8 it can be seen that v_s varies linearly with electric field at field strengths below 10 kV/cm for Si. While the carrier velocity may equal v_s when the initial bias (> 10 kV/cm) is applied, this will clearly not be the case as the electric field collapses as the switch becomes conductive. Mourou and Knox, in effect, assume the photogenerating process creates "super carriers" which move at the high field drift velocity even in the low field regime. This "super carrier" assumption also leads to a gross underestimate of the optical energy required to switch a given voltage. This underestimation has been observed in practical pulsed-power switch engineering projects.

A more detailed analysis of photoconductive switching by Li *et. al.* [12] assumes constant carrier mobility. Nunnally and Hammond [13] also make this assumption and imply that this analysis is valid at field strengths equal to the bulk breakdown field for the switch, ~100 kV/cm. Extrapolation of the low field, linear regime to 100 kV/cm leads to an order of magnitude overestimation of the carrier velocity, again a "super carrier" assumption. The constant mobility assumption is not valid for bias fields in the saturated velocity regime.

The two bias fields in the experiment, 43 and 63 kV/cm, are well into the saturated velocity regime. As the switch is driven conductive, the carrier velocity moves into the linear regime. Depending on the bias field, a different path is taken to the conductive state. The process is not so simple as the optical injection of carriers in a constant bias field. Weiner *et. al.* also do not report a variation in rise time in their results of constant mobility numerical switch modeling [14], although their model does include field variation with time. The electric field, carrier density, and carrier mobility and, thus, velocity are interdependent and any model must include *all* variables.

This chapter's experimental results, which are significant as they were done at the highest bias voltage/fastest time scale combination yet achieved and with insignificant circuit effects, compare favorably with our model of the photoconductive process, described in detail in Chapter 5.

CHAPTER 2

REFERENCES

[1] I.A.D. Lewis and F.H. Wells, *Micromillisecond Pulse Techniques*, (McGraw-Hill Book Co., New York, 1954) p.23.

[2] A. Yariv, *Quantum Electronics*, 3rd ed., Chapter 14, (John Wiley and Sons, New York, 1989) pp.298-323.

[3] J. Valdmanis, "Subpicosecond Electro-Optic Sampling," Thesis (Ph.D)University of Rochester, Institute of Optics, (1983).

[4] A.Yariv and P. Yeh, *Optical Waves in Crystals*, Chapter 4, (John Wiley and Sons, New York, NY,1984) pp.69-120.

[5] Yariv, op. cit , pp.289-299.

[6] Yariv and Yeh, op. cit., p.223.

[7] J.A. Valdmanis, G. Mourou, and C.W. Gabel, "Subpicosecond Electrical Sampling," *IEEE Jour.Quant.Elect.* **QE-19**, 664 (1983).

[8] G.A. Mourou and K.E. Meyer, "Subpicosecond Electro-Optic Sampling Using Coplanar Strip Transmission Lines," *Appl.Phys.Lett.* **45**, 492 (1984).

[9] P.le Fur and D.H. Auston, "A Kilovolt Picosecond Optoelectronic Switch and Pockels Cell," *Appl.Phys.Lett.* **28**, 21-23 (1976).

[10] G. Mourou and W. Knox, "High Power Switching with Picosecond Precision," *Appl.Phys.Lett.* **35**, 492 (1979).

[11] G. Mourou and W. Knox, "A Picosecond Jitter Streak Camera," *Appl.Phys.Lett.* **36**, 623 (1980).

[12] K.K. Li, J.R. Whinnery, A. Dienes, "Pulse Forming with Optoelectronic Switches," *Picosecond Optoelectronic Devices*, edited by C.H. Lee (Academic Press, Orlando,1984), pp.189-217.

[13] W.C. Nunnally and R.B. Hammond, "Optoelectronic Switch for Pulsed Power," *Picosecond Optoelectronic Devices*, edited by C.H. Lee (Academic Press, Orlando,1984), pp.373-398.

[14] M. Weiner, L. Bovino, R. Youmans, and T. Burke, "Modeling of the Optically Conrolled Semiconductor Switch," *Jour. Appl. Phys.* **60** (2), 823 (1986).

CHAPTER 3

TWO-DIMENSIONAL ELECTRO-OPTIC IMAGING SYSTEM

The switched output waveform of a photoconductive switch was characterized using electro-optic sampling, as reviewed in Chapter 2. Such a measurement of the output waveform yields information about the temporal evolution of the voltage at the output electrode of the switch, but gives no information about the evolution of the rapidly varying electric field within the electrode gap itself. By combining electro-optic sampling, short-pulse lasers, and imaging technology, an ultrafast, 2-D, electro-optic imaging system was developed that can monitor rapid variations of the switch surface electric field over an extended region. As the tangential component of the surface field is continuous across the semiconductor interface, surface field maps can be used as a probe of the underlying carrier dynamics in the switch gap. This chapter will review the development of this diagnostic. It is the latest advance in the characterization of electric fields produced by metallic contacts on semiconductor surfaces [1,2].

The work on this project progressed through an number of phases. The first requirement was to show that surface fields could be mapped with the electro-optic sampling technique. The next phase was to show that the field could be imaged with a detector array rather than a single detector. This allowed the mapping of multiple spatial events with a single laser pulse. Finally, the system was upgraded to use 2-D detectors and single-shot imaging.

I. EARLY WORK: STATIC 2-D AND DYNAMIC 1-D IMAGING

1.STATIC 2-D IMAGING SYSTEM AND SELECTED RESULTS

The initial series of measurements investigated the low voltage, quasi-static configuration of the surface electric field for two rectangular electrodes separated by a fixed distance on a semiconductor surface to see geometric and contact effects [3,4]. This work will be briefly discussed.

A piece of y-cut $LiTaO_3$ was placed across evaporated metal contacts on both silicon and gallium arsenide. Laser-annealed and unannealed contacts were tested. A dielectric mirror was bonded directly to the electro-optic (e-o) crystal and the entire assembly was placed directly on top of the surface to be monitored covering the contact gap completely. The dielectric mirror was in contact with the semiconductor substrate surface. The crystal was, thus,immersed in the surface field extending from electrode to electrode. The $LiTaO_3$ optic axis (z-axis) was perpendicular both to the direction of light propagation and the edges of the electrodes. Thus, the optic axis was oriented along the electric field lines and the Pockels effect was sensitive to only the component of the electric field perpendicular to the electrode edges. The crystal/field arrangement is shown in Fig.3.1. The experimental set-up is shown in Fig.3.2.

A time-varying potential (5 V, 1-kHz square wave) was placed across the contacts that induced a modulation of the birefringence of the $LiTaO_3$ in both space and time via the Pockels effect. A tightly focused cw HeNe laser, with a spot size of approximately 40 μm, probed the crystal birefringence, passing through the polarizer and compensator, traversing the e-o crystal, reflecting from the dielectric mirror, and

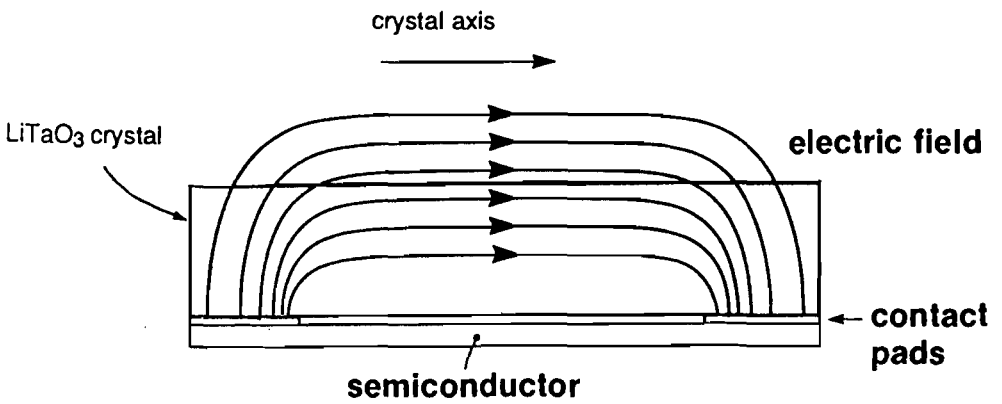

Fig.3.1 Arrangement of $LiTaO_3$ crystal in surface field above semiconductor surface.

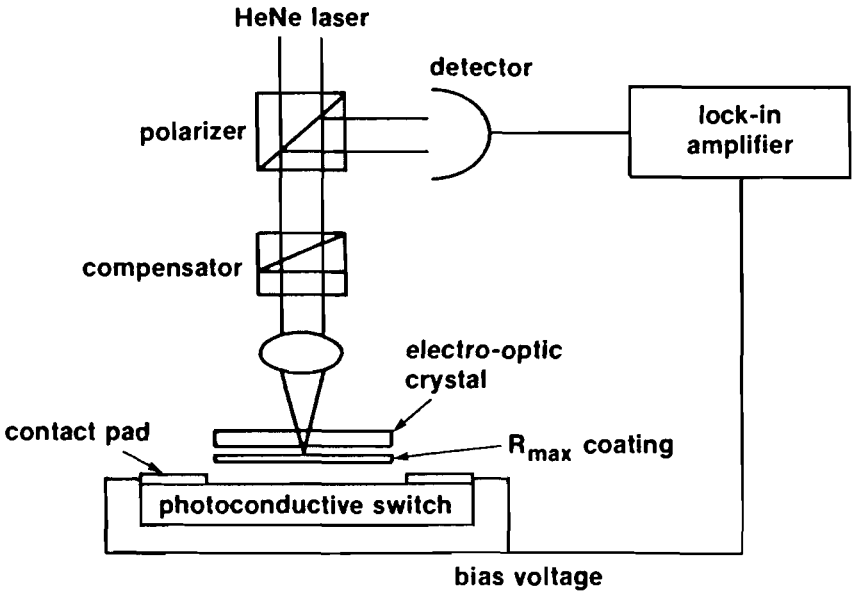

Fig.3.2 Surface field probe utilizing pinpoint, cw electro-optic sampling.

retracing its path back to the polarizer and on to the photodetector. Due to the double pass through the polarizer, the e-o crystal is effectively between crossed polarizers. The compensator biases the optical transmission at the 50% point. The e-o signal appears as 1-kHz modulation of the transmitted intensity to the photodiode. The low voltage applied to these devices produced very weak e-o modulation of the optical signal requiring that the signal be extracted with a phase-sensitive detector. An EG&G lock-in amplifier was used to provide the bias voltage and to extract the 1-kHz e-o signal from the photodiode signal. The spatial profile was obtained by translating the e-o crystal and semiconductor in such a way that different points in the crystal were illuminated by the laser beam. The translation stage and lock-in were computer controlled. Fig.3.3 shows a cross section of the electrically induced birefringence along the center line between laser-annealed Al contact pads on a silicon switch, electrode gap 2.5 mm, obtained with this system. By translating the sampling point across the crystal in two orthogonal directions, a two dimensional map of the surface electric field can be obtained, as shown in Fig.3.4 for unannealed Al contacts on Si.

2. DYNAMIC 1-D IMAGING SYSTEM AND RESULTS

The data acquired as described above lacked temporal resolution and required that the beam be scanned across the device to acquire the total spatial variation of the field. It also required lock-in techniques to obtain the e-o signal. Such conditions are incompatible with the need to record spatially non-local, transient events typical of photoconductivity. To time resolve events short-pulse laser probes must be used instead. The spatial variations in the surface field were monitored by illuminating the entire area of interest, so that the electric field at every point in the electrode gap was interrogated. Instead of using a single detector and scanning a tightly focused spot, a

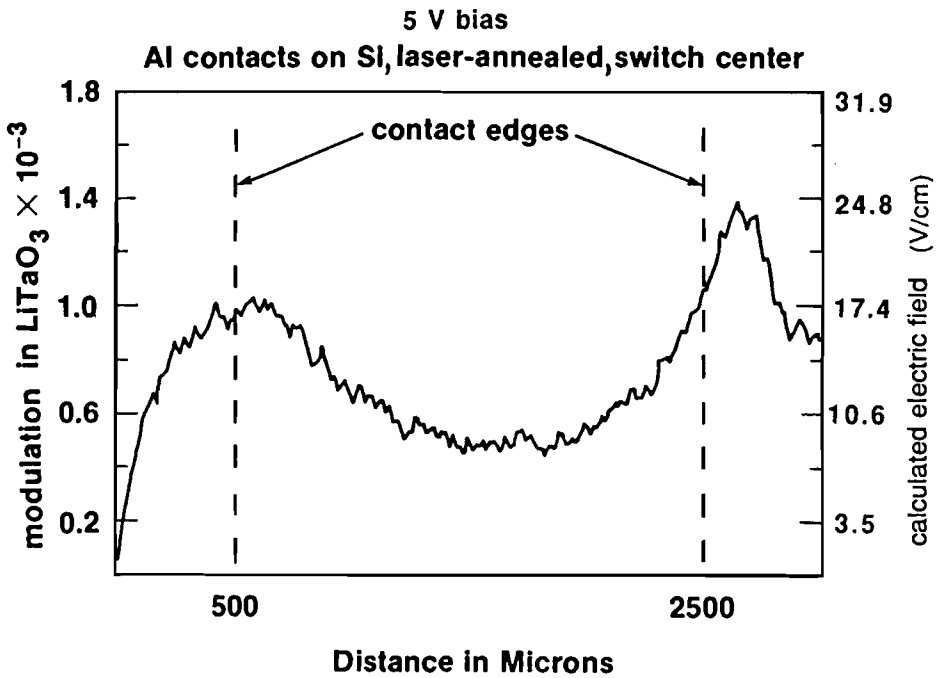

Fig.3.3 Profile of electrically induced birefringence along center line between Al contact pads on Si measured using cw probe. The electric field calculated from the induced birefringence is also given.

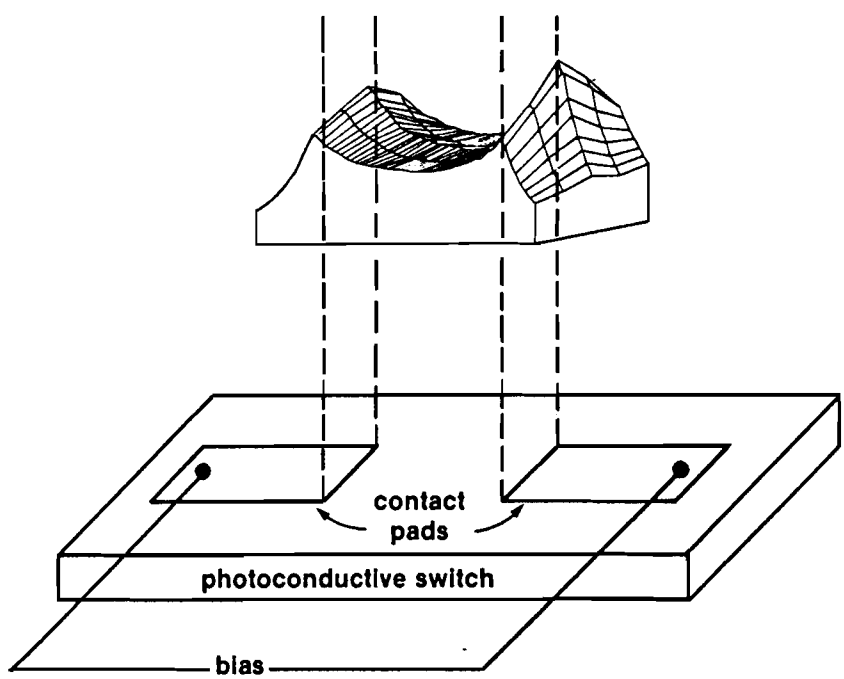

Fig.3.4 Two dimensional map of electrically induced birefringence obtained by translating switch beneath sampling probe point.

detector array was used, each detector element measuring only a small portion of the electric field, increasing the speed of data acquisition. Higher bias voltages produced significant e-o modulation which allowed for data collection with a single laser pulse: no averaging was required.

The initial experiment was done with a 512-element, linear, intensified diode array as shown in Fig.3.5. A 2-mm gap with identically prepared gold-coated, laser-annealed contacts on intrinsic silicon ($\rho = 7000\ \Omega$cm) was pulsed biased with a short electrical pulse synchronized with respect to the laser pulse. Y-cut $LiTaO_3$ covered the switch gap, oriented as in Fig.3.1. The sample was illuminated with a 120-ps, 532-nm light pulse at the peak of the voltage pulse. A 50-Ω load was placed on the low side of the silicon and the leakage through the material was monitored on an oscilloscope. The lack of photoconductive switching at the load guaranteed that none of the light coupled through the dielectric mirror into the silicon. It is important that the probe light does not perturb the field. The laser illuminated a circular region on the silicon surface. The detector acquired a 1-D slice of the electric field on a line joining the two electrodes midway between the ends of the electrodes. This was the first demonstration of imaging technology applied to electro-optic field measurements [5]. Initially, the electric pulse was applied with conventional high-voltage pulser, rise time ~100 ns, giving a quasi-static measurement. Later, the electrical pulse was applied with a second photoconductive switch for time-resolved data.

The time-resolved data was taken by grounding one of the electrodes on the high-resistivity Si switch and attaching the other to a terminated 50-Ω line driven by a second photoconductive pre-switch to pulse bias the test structure on a 100-ps time scale. The second pre-switch was triggered with a 1064 nm light pulse from the

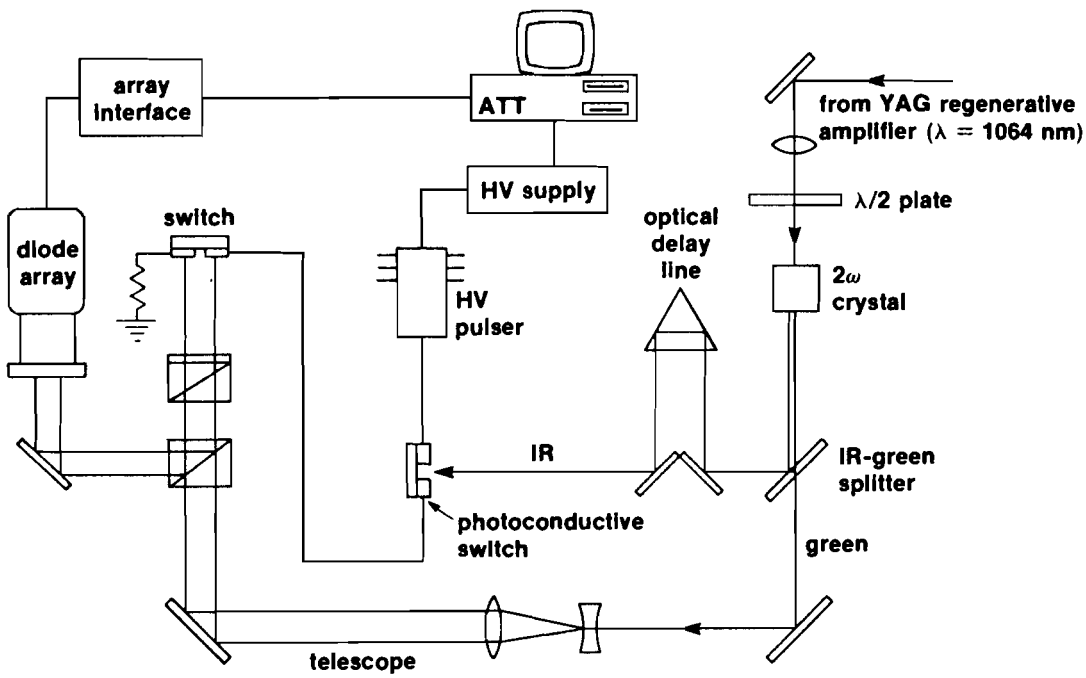

Fig.3.5 Schematic of 1-D, dynamic electro-optic sampling system.

Nd:YAG regenerative amplifier. A 532 nm pulse, derived by frequency doubling a portion of the 1064 nm pulse, probed the $LiTaO_3$ crystal on the test switch. An optical delay line in the path of the 1064 nm light provided a variable time delay between the voltage and probe. The time-evolution of the cross section of the field between the two electrodes is shown in Fig.3.6. The units of the vertical axis are in percent modulation of the light signal (i.e., the signal obtained with the voltage on, minus the signal with the voltage off, divided by the signal with the voltage off). The temporal resolution of this data is ~120 ps.

3.ANALYSIS OF EARLY EXPERIMENTS

The static electric field distribution produced by the coplanar electrodes used in these experiments was not uniform. It is a common field configuration encountered when fabricating devices on wafers (e.g., coplanar transmission lines between transistors in VLSI circuits or photoconductive switches fabricated on wafer substrates). The field lines in a plane perpendicular to the surface are shown in Fig.3.7(b). They may be derived from the simple case illustrated in Fig. 3.7(a) by the operation of a conformal transformation [5]. The parallel electrode pattern is first laid out on a plane, where $w = u + iv$. Then it is transformed to a second complex plane where $z' = x' + iy'$, upon which the coplanar electrodes are laid out. The transformation begins with the application of a transform to the z plane:

$$z = 2\,\ell n\left\{\frac{\left\{[1 + \sin(w)]^{1/2} + [b_z + \sin(w)]^{1/2}\right\}}{(b_z - 1)^{1/2}}\right\} . \qquad (3.1)$$

Followed by the second transformation to the z' plane:

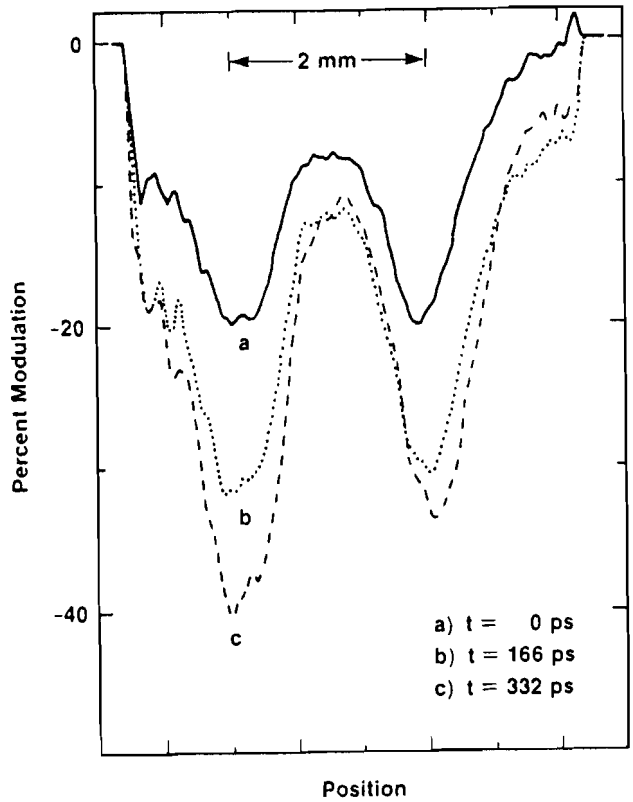

Fig.3.6 Time evolution of electric field profile above a Si switch after application of step function bias. The contact gap was 2 mm, the bias was 1 kV.

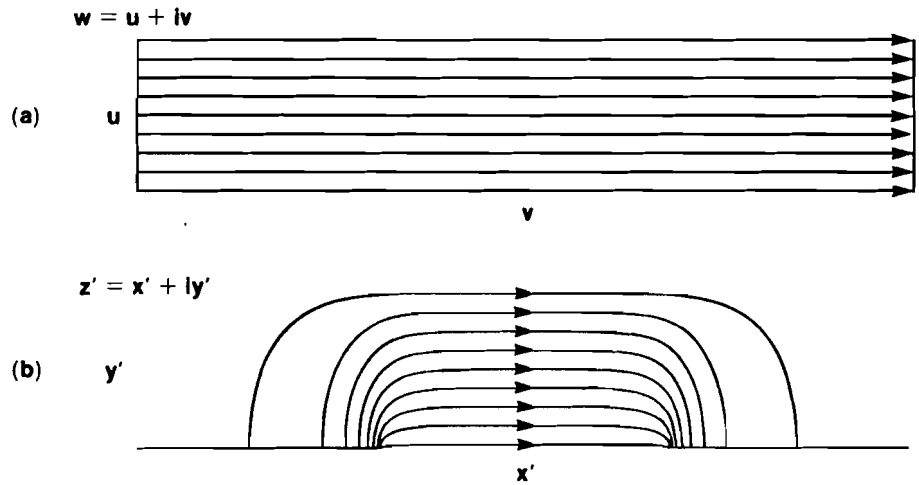

Fig.3.7 Variables and geometry for conformal mapping of electric field distribution of: a) parallel electrodes, to b) coplanar electrodes.

$$z' = w_d - 2\,\ell n\left\{\frac{\left\{[1 + \sin(iz+\pi/2-iw_g)]^{1/2} + [b_z + \sin(iz+\pi/2-iw_g)]^{1/2}\right\}}{[b_z - 1]^{1/2}}\right\}. \qquad (3.2)$$

where:

$$b_z = 2\coth^2(\pi\,\ell_c/2\,\ell_s) - 1\ , \qquad (3.3)$$

w_g is the normalized gap width; ℓ_c the electrode length; ℓ_s the substrate thickness; and w_d a parameter used to set the transformed coordinates' origin.

These transformations fold the parallel electrode end faces out into the coplanar geometry. The second transformation is only valid if the transformed plane is at infinite distance from the first plane because the electric field lines must be normal to the second plane. However, if the electrodes are sufficiently far apart, the deviation from normal incidence is negligible. The transformation, which is one dimensional, defines the expected value of the electric field throughout the volume of the semiconductor provided that the measurement is not taken near the corners of the electrodes (where the 1-d analysis is not valid). The fringing field outside of the semiconductor can be inferred from electromagnetic theory (i.e., the surface electric field is continuous across a dielectric interface). Thus, the coplanar electrode configuration provides a reasonable test of the ability to map electric field configurations.

From the known electric field configurations in Fig. 3.7(a), the electric field in Fig.3.7(b) can be calculated. For the type of e-o crystal that was used in this experiment, the electric field along the y axis in Fig.3.7 was measured. Fig.3.8 shows the field in the plane of the interface. The features are exactly as expected. Above the contacts the electric field is normal to the surface; therefore, the field along the y axis is zero. At the edge of the contacts the field lines bunch-up due to the attraction of charges on the opposing electrodes. However, this is not what is

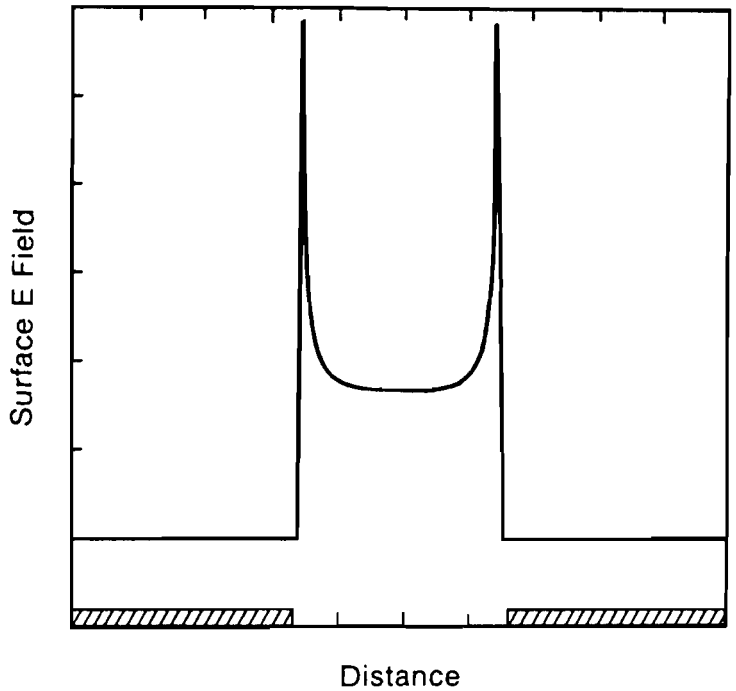

Fig.3.8 Field profile directly at surface obtained from conformal map.

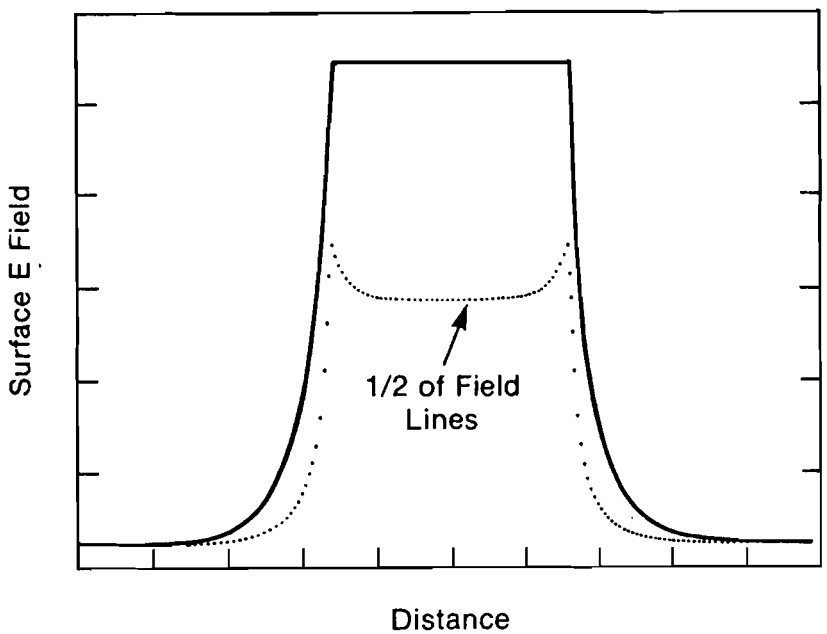

Fig.3.9 Field profile after integrating over crystal thickness, perpendicular to electrode plane. Upper curve has been integrated over all field lines. Lower curve is result of integral over 1/2 field lines. Note loss of detail compared to Fig.3.8 as crystal becomes thicker.

actually measured. As the crystal has a finite thickness, T, the probe beam and field induced birefringence interact over the distance T What is actually measured is the polarization rotation, θ, experienced by the probe beam in the crystal:

$$\theta(x) = \int_{IA} dA \int_{0}^{T} \alpha E_x(x,y)dy \tag{3.4}$$

where y is along the direction of the probe beam, IA is the area illuminated by the probe beam, and α is the e-o coefficient as in Eq.2.3. This integral is clearly dependent on the thickness of the e-o crystal. Fig.3.9 shows the integrated detected signal as a function of the e-o crystal thickness. The uppermost curve indicates what happens if the crystal is so thick that the integral extends over all the field lines. The surface features are completely obscured because the total integrated flux is conserved between the electrodes. Alternatively, if the crystal is too thin, then the modulation imparted to the light signal becomes very small, since the amount of rotation is proportional to the optical path length in the crystal. However, the high dielectric of the e-o crystal will trap most of the field lines, reducing the peaking of the contacts. Additionally, smearing of the detected signal is also incorporated into the calculation of the curves in Fig. 3.9. The signal must be averaged over either the laser spot size or the size of the detector element on which it is imaged. In Eq. (5) this is represented by the integral over the illuminated area (IA).

Fig.3.4 displays a cross-sectional view of the field along the center line between the contact pads on a Si switch. The applied electric field was essentially dc. The figure shows the general features that are expected, the bunching at the contacts, and the tailing off at the electrodes. The sampling crystal was thick with respect to the electrode separation. Therefore, the peaks exhibit a significant amount of smearing. What is most interesting is the asymmetry of the electric field. The contacts were

identically prepared, so no asymmetry was expected from the material properties of the sample. When the polarity of the applied bias was reversed, the asymmetric field distribution also reversed. This indicated that the contacts were not ohmic with respect to the different carrier species (electrons and holes). It was also noted that as the contacts became more ohmic, the peaking at the edges decreased. Semiconductors, with their mobile charge carriers, that can move in response to the applied field, would not be expected to rigidly conform to the field distribution described above.

The time-resolved data shows the time scale on which the asymmetry illustrated in the cw data evolved. The dielectric relaxation time of this material is given by the product

$$\rho\varepsilon = \rho\varepsilon_0\varepsilon_r = (\ 7000\ \Omega\text{m} \times 11.9 \times 8.85 \times 10^{-12}\ \text{F/m}\ ) = \sim 7\ \text{ns}.$$

where $\varepsilon_r = 11.9$ is the relative dielectric constant of the silicon. Thus, on time scales <7 ns, one expects to see transient behavior of the silicon in response to an applied electric field. Fig.3.6 shows three traces of the surface electric field of a device with a 2-mm gap pulsed with a 1-kV voltage pulse and measured with the gated diode array at various time delays between the pump and probe. At very early times (a), very little voltage has built up but the device appears to be symmetric in response to the electric field. Curve (b), 166 ps later, shows that a significant voltage has built up across the device and the field is still symmetric. At 166 ps later still (c), the voltage is still rising but the field shows a definite asymmetry. The simple explanation of this data is that at early times the electrical inertia of the silicon prevents it from reacting to the field. The device then behaves as if it were a perfect dielectric, and the field rises symmetrically on both electrodes. Later, as the charge carriers in the silicon begin to

rearrange in response to the field, the field itself is modified by the charges in the silicon.

Neither the point sampling nor the 1-D measurement made allowance for the possible spatial variation of crystal properties and they were not properly calibrated. The primary result of the cw experiments was to demonstrate that spatial variations in the surface field between the switch electrodes could be detected and that this is a reliable method of characterizing the contacts [6]. The time-resolved 1-D data showed that single-shot data acquisition and field imaging were possible without extensive signal processing. The 2-D, time-resolved e-o imaging system was the logical extension of this work.

II. 2-D ELECTRO-OPTIC SAMPLING

1.SYSTEM

Electro-optic imaging of extended areas was made possible by the replacement of the 512 element linear array, used in the 1-D experiments,by a 512 x 512 element video camera. With a short-pulse probe, this unique system could, in effect, obtain instantaneous "snapshots" of the surface electric field on a picosecond time scale [7,8].

Two different probe geometries were used and the pump/probe roles of the fundamental and second harmonic of Nd:YAG could be reversed. Fig.3.10 shows the 2-D surface field probe set up to measure the field of a photoconductive switch of a surface device type, i.e., the metallic contacts are in the same plane on the surface of a semiconductor substrate. Fig.3.11 shows the probe set up to measure the field of a bulk photoconductive switch, which has contacts on opposite faces of a rectangular slab of a semiconductor. The geometry shown in Fig.3.11 had the advantage of a

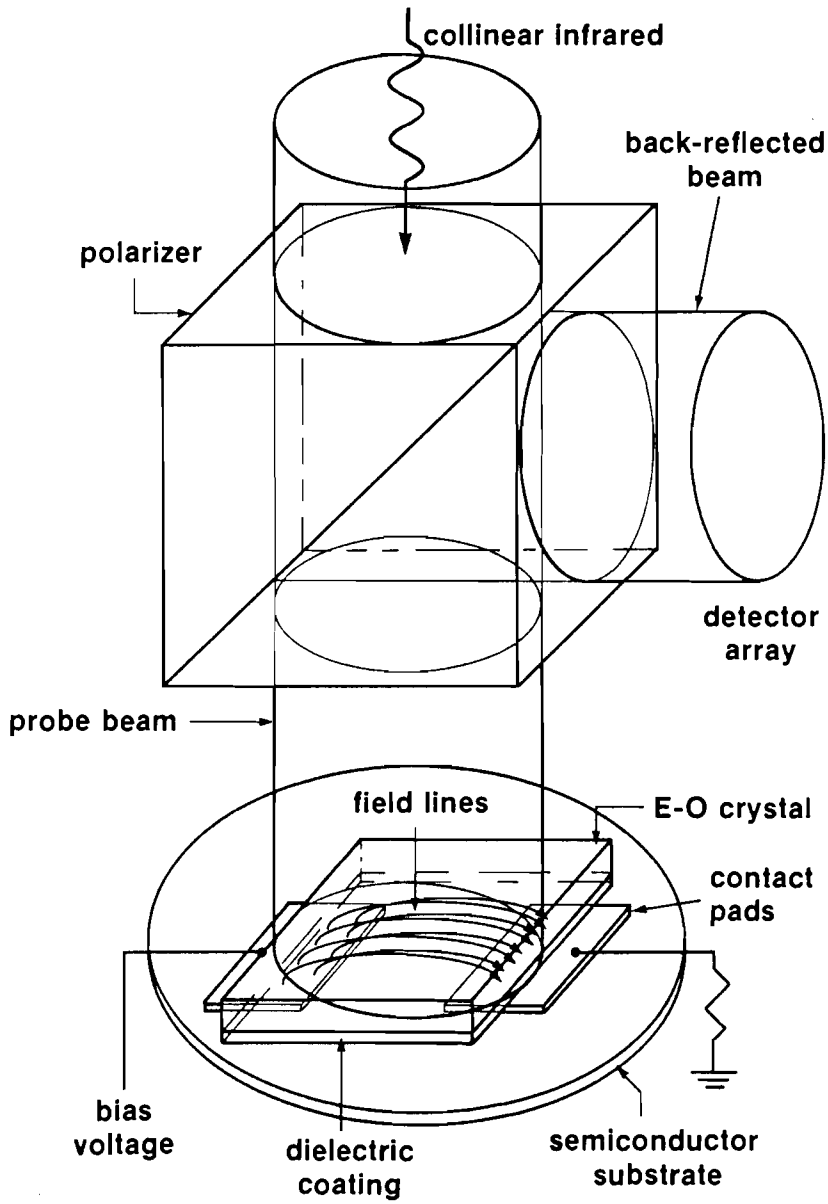

Fig.3.10 Detail of electro-optic probe set-up to measure electric field above photoconductive switch of surface device type.

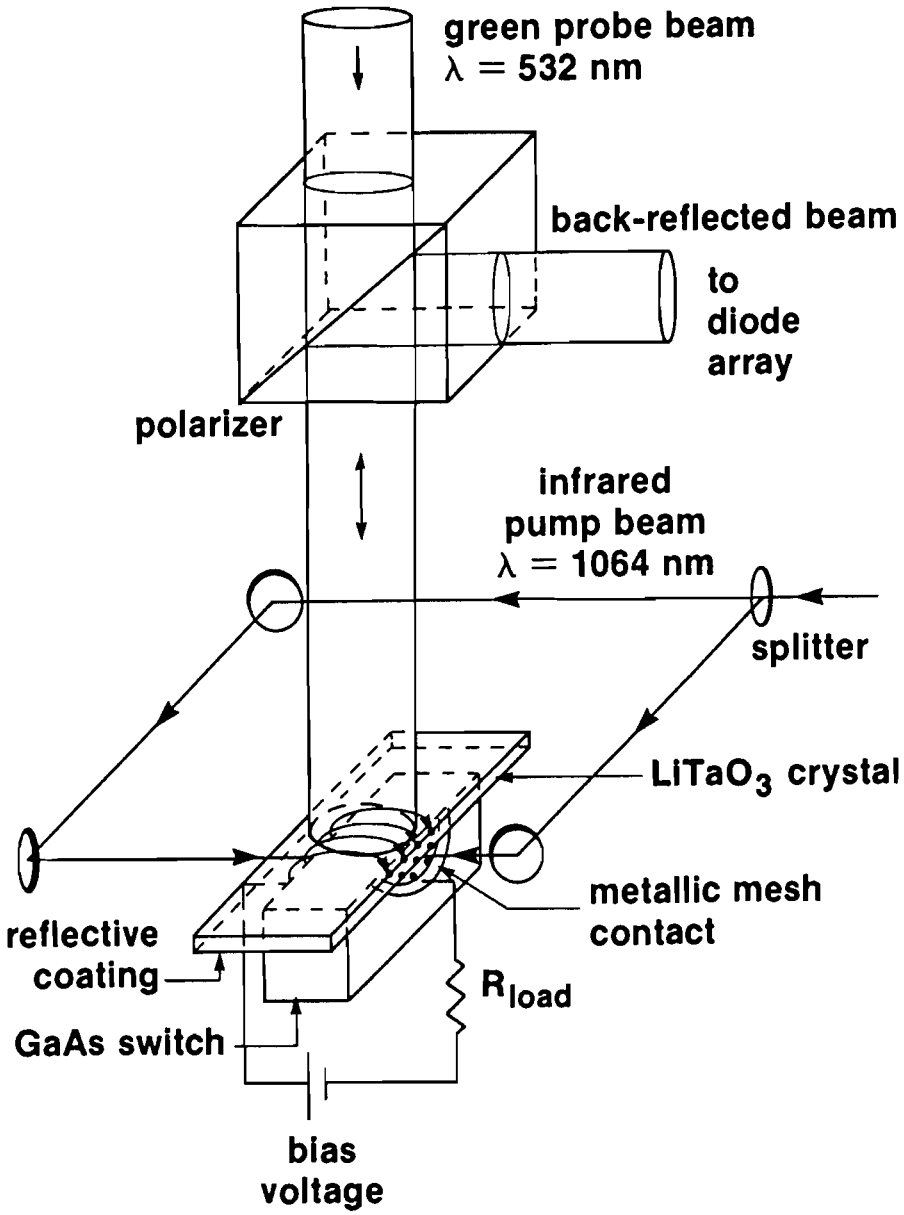

Fig.3.11 Detail of electro-optic probe set-up to measure electric field of GaAs bulk photoconductive switch.

much simpler (i.e., spatially uniform) field distribution. For either type of switch, probe operation is the same, only the pump geometry is different. Each point in the beam transmitted to the detector array has sampled the local birefringence of the corresponding point in the crystal. Thus, the intensity profile of the transmitted beam is an optical replica of the electrically induced birefringence pattern in the crystal. The back-reflected beam is imaged onto the 2-D diode array that records the beam's intensity profile. Each pixel in the array image has a corresponding point in the crystal. The intensity at any given point in the cross section of the back-reflected beam will depend on $\sin^2\theta$, where θ is the polarization rotation experienced by that particular beam element as it traverses the crystal. The transmission to a detector element (i,j), can be written:

$$T_{ij}(V) = I_{ij}(V)/I'_{ij} = \sin^2 [(\alpha_{ij}E_{ij} + \beta_{ij})] \tag{3.5}$$

where $I_{ij}(V)$ is the light intensity measured at camera pixel (i,j) when a voltage V is applied to the electrodes; I'_{ij} is the intensity that appears at the camera if 100% of the light is imaged onto the camera without bias voltage applied; E_{ij} is the magnitude of the local electric field; α_{ij} is a constant for a given point (i,j) which relates the electro-optic coefficient to the local electric field ; and β_{ij} is a constant optical rotation due to static birefringence in the crystal and $\lambda/4$ wave plate setting. Eq.(3.5) is the 2-D version of Eq.(2.3). The $\lambda/4$ plate setting determines where the probe beam sits on the sine-squared transmission curve with no voltage applied.

The field data must be extracted from the raw camera image. The values of α_{ij} and β_{ij} for each point (i,j) must be measured so that given the transmission T_{ij}, the field E_{ij} can be determined. The crystal is not illuminated uniformly because the probe beam has a Gaussian spatial profile. This must be considered in the analysis of

the data. Therefore, before the field can be determined, the raw image must be normalized with respect to the beam profile, so that the transmissivity and not the transmitted intensity is used.

To calculate the transmissivity, each image acquired by the camera is normalized to a stored reference image. This reference image is the average of four frames taken with the quarter-wave plate set for maximum transmission. The light intensity is adjusted so that the most intense pixel is just within the 8-bit camera resolution; i.e., no points in the detector field are saturated. This reference image contains I'_{ij} for each point (i,j), as in Eq. (6). Images normalized with respect to this reference are scaled to the maximum signal and represent $I_{ij}(V)/I'_{ij}$.

The values of α_{ij} and β_{ij} are obtained by calibrating the response of the probe to applied electric field. A quasi-dc, i.e, long compared to the light pulse, bias voltage is applied to the contacts by a computer controlled high-voltage pulser only when an image is to be taken to eliminate any Joule heating in the switch and any thermally induced birefringence in the e-o crystal. The bias voltage is varied from 0–9.5 kV in 500 V increments. An image was taken at each voltage. The initial data that was taken with the 2-D imaging system was reduced to a 32 x 32 format by averaging over pixels. This array size reduction is done so that image acquisition, processing, and display can be done with a PC rather than a workstation and in real time, i.e., without any post-processing. This allows for rapid scanning of camera images. The transmission curve [Eq. (3.5)] for each of the 1024 elements of the reduced image was determined experimentally by this procedure. α_{ij} and β_{ij} were obtained by performing a least squares fit of the experimental transmission curve to Eq.(3.5) for each element in the reduced image. Fig.3.12 shows this dc calibration

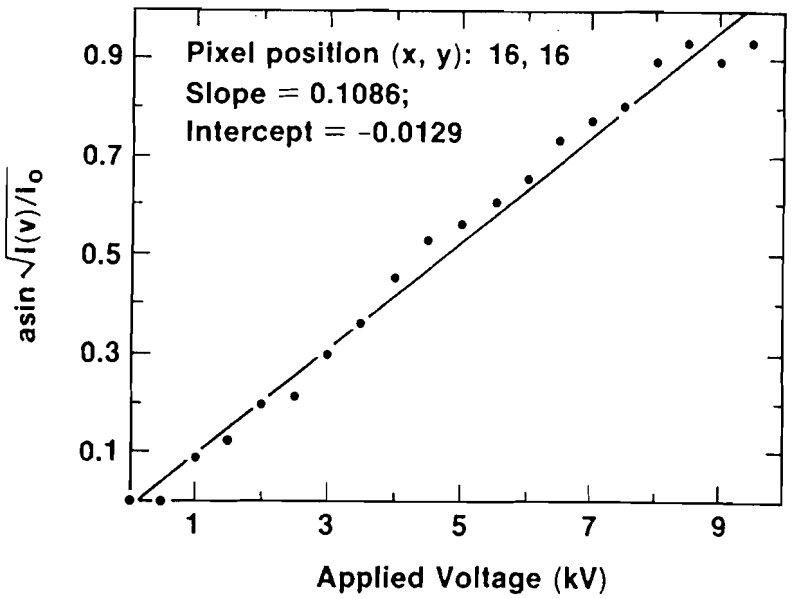

Fig.3.12 Results of DC calibration of electro-optic imaging system showing least squares fit of the experimental transmission curve to Eq.(3.5) for one image pixel.

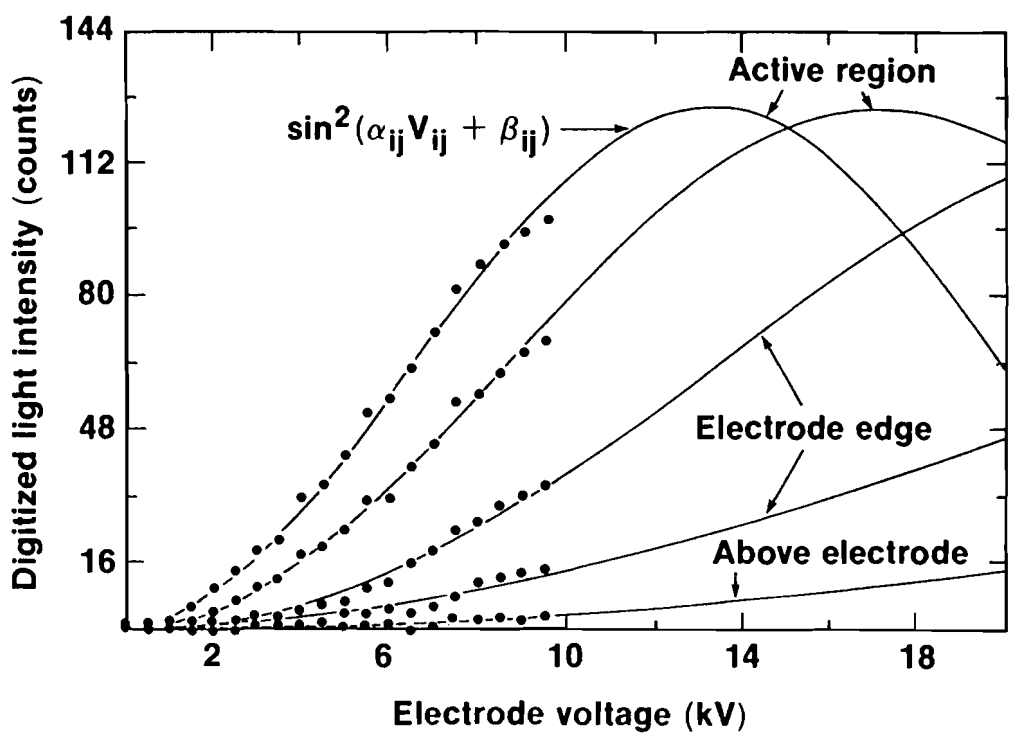

Fig.3.13 Transmission function for different pixels corresponding to various positions in the e-o crystal. The active region is the area between the electrodes Note the spatial variation in the e-o properties of the crystal, i.e. V_π is a function of sampled position.

for one element of the reduced image. The biasing is chosen such that all points lie within one-half cycle of the transmission curve. Due to the sinusoidal nature of Eq.(3.5), it is sometimes necessary to reduce sensitivity to see large effects. The spatial variation in the crystal parameters α_{ij} and β_{ij} is illustrated in Fig.3.13, which shows the calibration curves for several points in the sampling crystal. This is a much more sophisticated calibration procedure than the simple percent modulation done with the earlier work.

The e-o crystal used in the 2-D work was 0.5 mm thick, y-cut $LiTaO_3$; orientation as in Fig.3.1. The surface switches can be studied with both the IR pump with a visible probe and the visible pump with IR probe. $LiTaO_3$ with different coatings was used depending on probe wavelength. The top surface of the $LiTaO_3$ was antireflection coated to prevent spurious back reflection and improve transmission through the crystal. The bottom surface was coated with the a dielectric mirror that had a reflectivity of 99% for either the 532 nm or 1064 nm probe pulse A conventional oscilloscope attached to the load side of the switch revealed that the green probe light caused a voltage pulse equal to about 10^{-6} times the applied bias voltage to be switched to the load. This is negligible. Green or IR probes effectively do not excite the switch. The complete probe system is shown in Fig.3.14.

The system operation will be described for green probe light (only the relative amount of optical energy directed to the second harmonic crystal will change with probe wavelength). The infrared beam from the amplifier is first upcollimated and then split, 90% for switching use and 10% for second-harmonic generation. This green beam is upcollimated and serves as the probe beam. The green beam diameter is 1.25 cm, which completely illuminated the electrode gaps that were studied. The back-reflected green probe beam pulses are imaged onto a 512 x 512 element GE CID

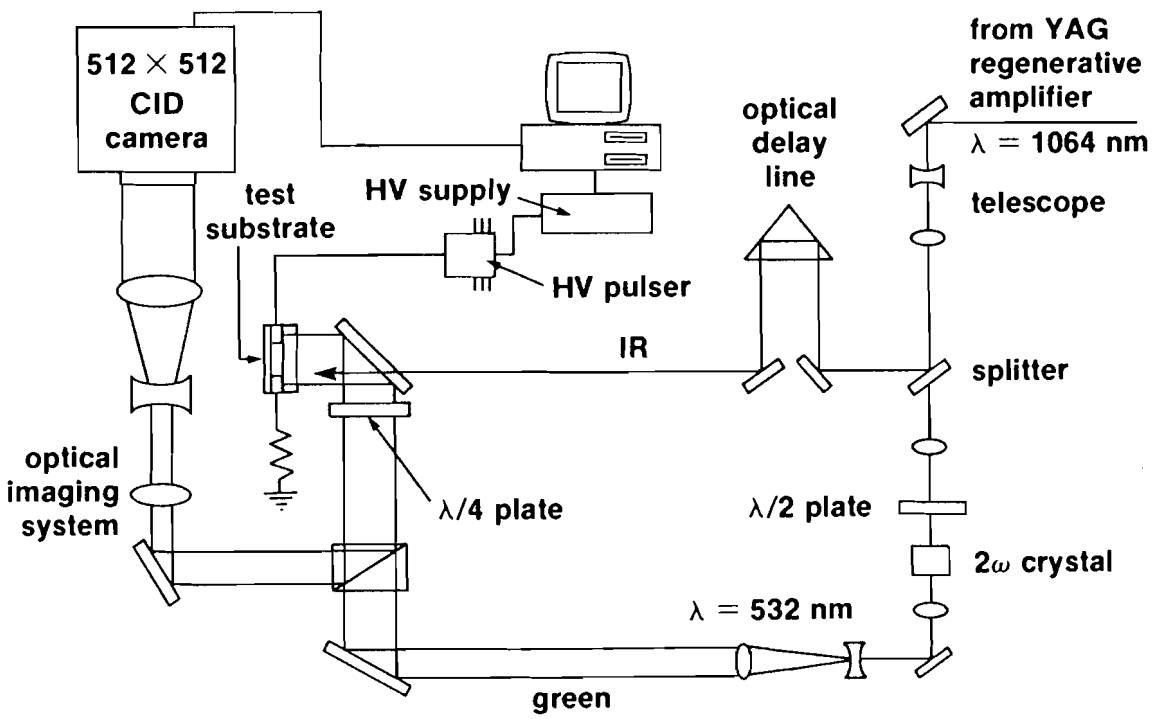

Fig.3.14 The complete electro-optic imaging system.

camera. The CID camera is interfaced to a personal computer through a PCVISIONplus video frame grabber supplying a digital image of the modulated probe beam. Images are digitized with 8-bit resolution. The camera response was measured to be linear with applied light intensity over the range of intensity used in this experiment. As the green probe was only 140 ps in duration, the switch surface field is sampled only during a short window in time. If an infrared excitation pulse illuminated the switch during this window, the switch field could be sampled during the photoconductive collapse. For surface switches, as in Fig.3.10, this is accomplished by directing a pump pulse onto the switch gap collinear with the probe pulse. For the bulk switches, Fig.3.11, the infrared illuminates the switch directly through the metallic mesh contacts. By sweeping the 140-ps sampling window through the photoconductively induced event, the switch surface field can be monitored as it evolves in time. This is actually 512 x 512 separate, parallel pump-probe experiments, each probing a different spatial region in the electrode gap. The sampling window is moved in time by changing the length of an optical delay line in the pump beamline.

As the system operates in the high-field regime, the change in transmission to the camera is large with respect to the shot-to-shot noise in the laser pulse. Thus, the electro-optic images can be acquired with a single pulse without averaging. To ensure that the camera sees only one laser pulse, the camera and laser are synchronized to the same electronic oscillator, with a pulse from the camera triggering the firing of the laser. The CID camera and laser repetition rate is 30 Hz. The overall image collection rate is ~.01 Hz. The overall energy of every laser pulse is measured with a fast diode. Any pulse that is not within 10% of a reference value is rejected and the measurement is repeated.

After correcting for the probe beam spatial profile and calibrating the crystal response, the surface electric field information can be decoded from the raw images from the camera. To measure the field, a frame is first acquired with high-voltage bias on and then with the bias off. The images are scaled by cross-referencing the raw image pixel (with voltage on) value and the corresponding reference pixel (voltage off) value and using a look-up table to determine the scaled image pixel value. The zero bias image is used to remove the contribution of the static birefringence, β_{ij}. The lookup table associates each pair of points in the reference and voltage images with a value corresponding to the product $\alpha_{ij}E_{ij}$. The scaled pixel image is divided by α_{ij}, as determined by the dc calibration described earlier, to yield E_{ij}. The field, E_{ij}, is given in units of "equivalent electrode voltage," or EEV, which means that the point (i,j) is responding to the applied electric field as if a voltage E_{ij} were applied to the electrodes. Although the electrode bias voltage may be constant, the local field E_{ij} may be nonuniform due to the presence of carriers or bending of field lines due to the geometry of the electrodes. The resulting field map of the electric field has an 8-bit range and can be displayed as a false-color image on a monitor or the digital image can be manipulated to produce field contour plots, 3-D plots, or field cross sections at a particular line across the switch. The optical system is capable of producing images with a spatial resolution of 3 μm per pixel. If no pixel averaging is done, i.e., the full 512 x 512 image is used , the electric field can be measured with this type of spatial resolution. This requires that the above calibration procedure be applied to the entire 262,144 element array. The system will then take full images at 4 voltage settings and use that data to calculate the least squares fit. Post-processing of the full images on a Sun workstation is required to

extract the electric field data. The minimum electric field sensitivity is approximately 200 V/cm and can be adjusted by rotating the quarter-wave plate before the $LiTaO_3$.

2. IMAGING OF PHOTOCONDUCTIVITY IN SILICON

The first demonstration of the 2-D e-o imaging system was with silicon switches. The Si switches were surface devices, as in Fig.3.10, where rectangular gold contact pads were deposited on a 1-in.diameter, 5-mm thick Si wafer. The electrode gap was 4 mm, and the contact width was 17 mm. The contacts were oven sintered and were measured to be ohmic to at least 1500V. A special switch holder was constructed for the multi-kilovolt bias to be used with these switches. This holder was vacuum tight, with a window for the laser pump and probe. A 50 Ω stripline, with Be-Cu spring clips, was used to connect the Si electrodes to the vacuum-tight high-voltage feedthroughs. The low side of the switch was connected by 50 Ω cable to a 50 Ω terminator. HN connectors and coaxial RG8 cable were used. The switch holder was pumped down to ~1 μm Hg and backfilled with ~50 psi SF_6 to prevent surface breakdown and arcing. Bias was applied with a computer controlled 0-10 kV pulser.

Figs.3.15 & 3.16 show typical data from raw, unnormalized, uncalibrated, 32 x 32 pixel-averged field images obtained with the electro-optic imaging system. The $LiTaO_3$ crystal was 1-cm square, covering the majority of the switch gap. Fig.3.15 shows successive lineouts of the surface field over the 4-mm gap Si switch taken through the center of the switch parallel to the contact edge. The switch bias was 5.8 kV. Green light was used as the probe, completely illuminating the $LiTaO_3$ crystal. The switch gap was excited by a 150 μJ IR pump pulse. The IR pump beam had a

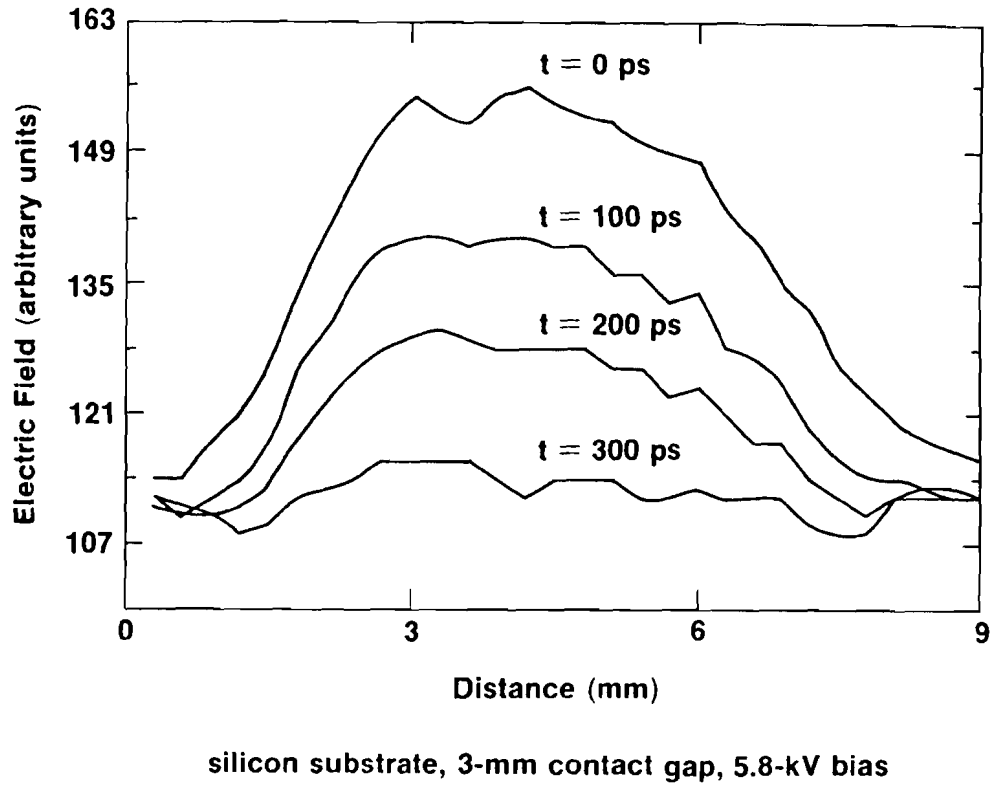

Fig.3.15 Collapse of electric field above IR illuminated surface type Si switch. Lineouts from raw electro-optic images taken through center of switch parallel to contact edge for various times (0 ps is before IR pump pulse). The switch was biased at 5.8 kV across a 4 mm contact gap. Note the spatially uniform collapse of the field. This data was taken before the imaging system development was complete and lacks later improvements in system calibration.

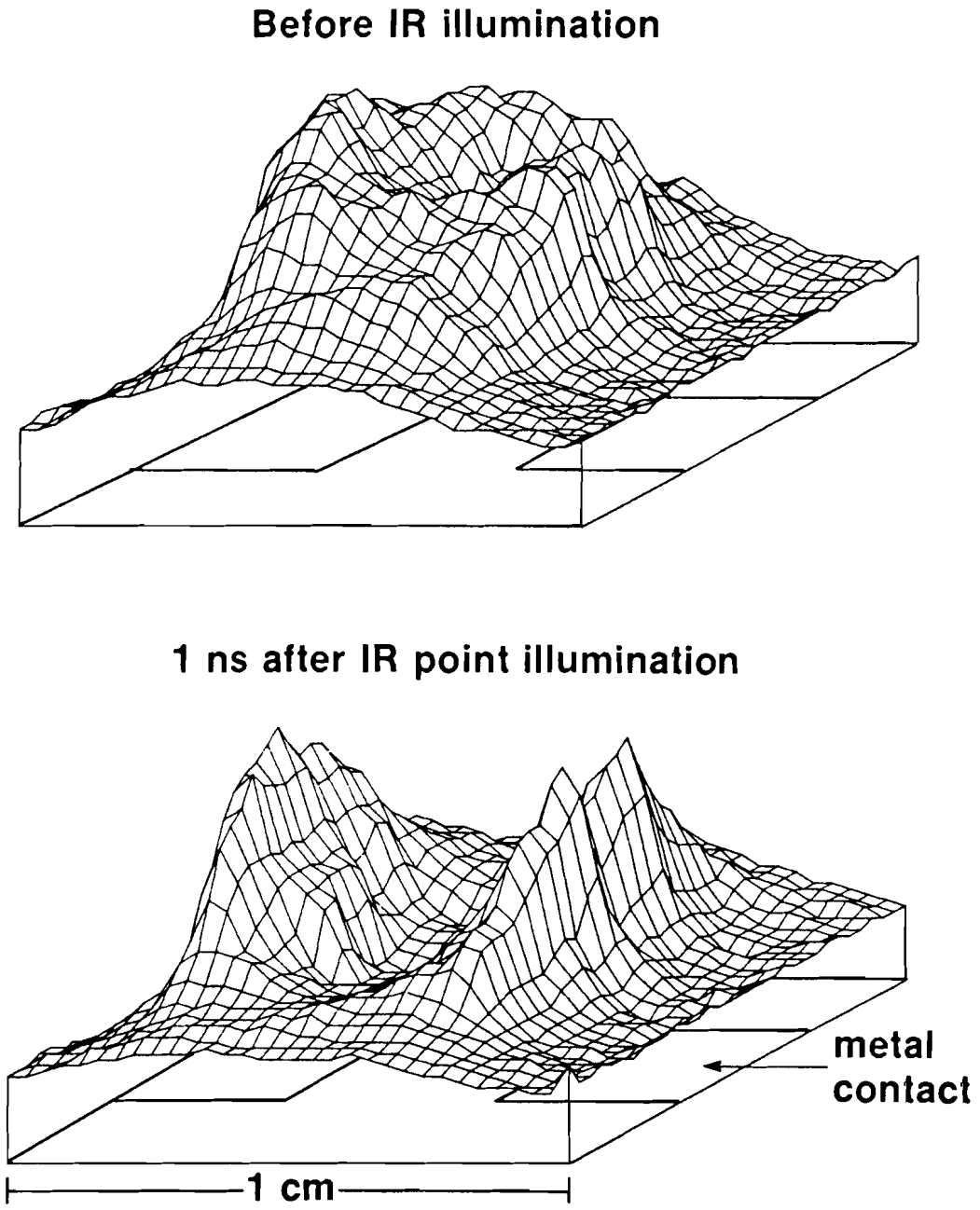

Fig.3.16 Effect of non-uniform illumination on the electric field above Si surface type switch. Raw electro-optic images shown before and 1 ns after illumination by 40 μm spot of IR energy at switch center. Switch was biased at 3 kV across 3 mm contact gap. Note local collapse of electric field near switch center.

Gaussian spatial profile and a diameter of ~6 mm, exciting carriers throughout the imaged region . Time is relative to the position of the IR optical delay line. The surface electric field begins collapsing at the onset of photoconductive switching and has collapsed completely within 300 ps, consistent with the ~200-ps pulse width of the laser. Fig.3.15 illustrates the ability of the system to monitor the surface field in the switch gap during switch operation, and the ability to measure switching parameters like switch rise time, using the field across the electrode gap. The field collapse is spatially and temporally uniform for spatially uniform illumination. This is typical of the imaging observed in silicon. The field collapses as the light pulse is applied and shows no oscillation or recovery (field recovery is not expected to be observed due to the μsec time scale for carrier recombination in Si). Fig.3.16 shows the result of nonuniform IR illumination on the Si switch surface field. The center of the switch gap was illuminated with a pinpoint (~40 μm) spot of infrared laser energy. This local illumination photogenerates carriers only in a small region at the gap center. These carriers migrate outward, collapsing the surface field as they drift. Figure 3.16 illustrates how the system maps nonuniform fields and that carrier effects within a small region in the switch gap can be observed. One significant feature of the field on the coplanar silicon switch is that the significant field enhancements at the contact edge, suspected from the geometry, were not detected. This may be due to a number of factors including: the presence of ohmic contact, the conductivity of the substrate, and the averaging of the dielectric crystal.

After the e-o imaging system was fully operational, a more complete study of the planar Si switch was done. Switch bias was 7 kV, and the images were obtained under a pressure of ~50 psi SF_6. IR probe light was used. The $LiTaO_3$ crystal was 1 cm by 3 cm, completely covering the 4 mm x 17 mm switch gap. Fig.3.17 shows

a)

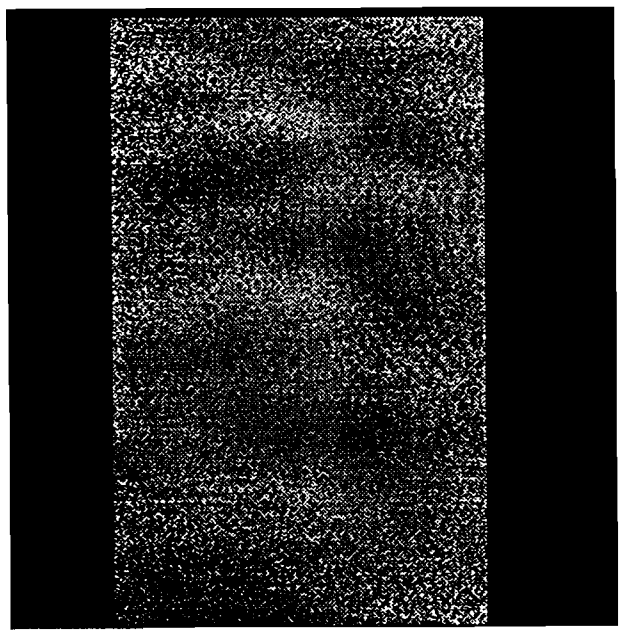

b)

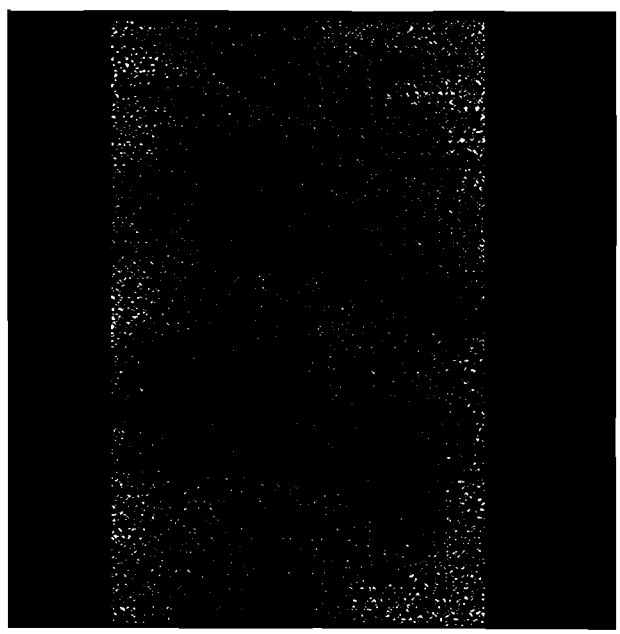

Fig.3.17 512 x 512 gray-scale images of the electric field above a Si photoconductive switch obtained with 2-D e-o imaging system. The electrodes were coplanar and the contact gap was 4 mm. Bias was 7 kV. High field is white, zero field is black. Image shown for a) before pump pulse, and b) 1650 ps after pump pulse. Note reduction in field strength following pump illumination.

gray-scale, 512 x 512 images of the electric field above the 4-mm gap Si switch. Low field is indicated by black, high field by white. The contacts have been artificially set to black. Fig.3.17(a) is a field image before green pump illumination; Fig.3.17(b) is an image 1650 ps after the pump pulse. The green pump pulse energy was 50 μJ. The electric field between the contacts has collapsed, as evidenced by the shift from white towards black going from Fig.3.17(a) to 3.17(b). The collapse of the field is seen dramatically in Fig.3.18, where the image data has been processed and presented as lineouts, showing the electric field profile along a line between the contacts perpendicular to the contact edge obtained by averaging over all 512 pixels along a line parallel to the contact edge. Profiles are shown at a time before the pump pulse, 1000 ps after the pump, and 2000 ps after the pump. The field collapses to a value of 2 kV EEV (the true field equals EEV divided by the electrode gap, or 5 kV/cm) and remains collapsed out to the 2000 ps limit of the IR delay line. A residual voltage of 2 kV is not unreasonable considering the large volume of Si that must be driven conductive (4 mm x 17 mm x .5 mm) and the low pump power, and is consistent with the photoconductive switch model for the experimental operating parameters. The collapsed field shows little spatial variation, also in agreement with the model.

The e-o imaging of photoconductivity in Si revealed that Si is a relatively simple photoconductive system, displaying the expected behavior. The results obtained with Si were very useful for comparison to the results obtained with GaAs switches.

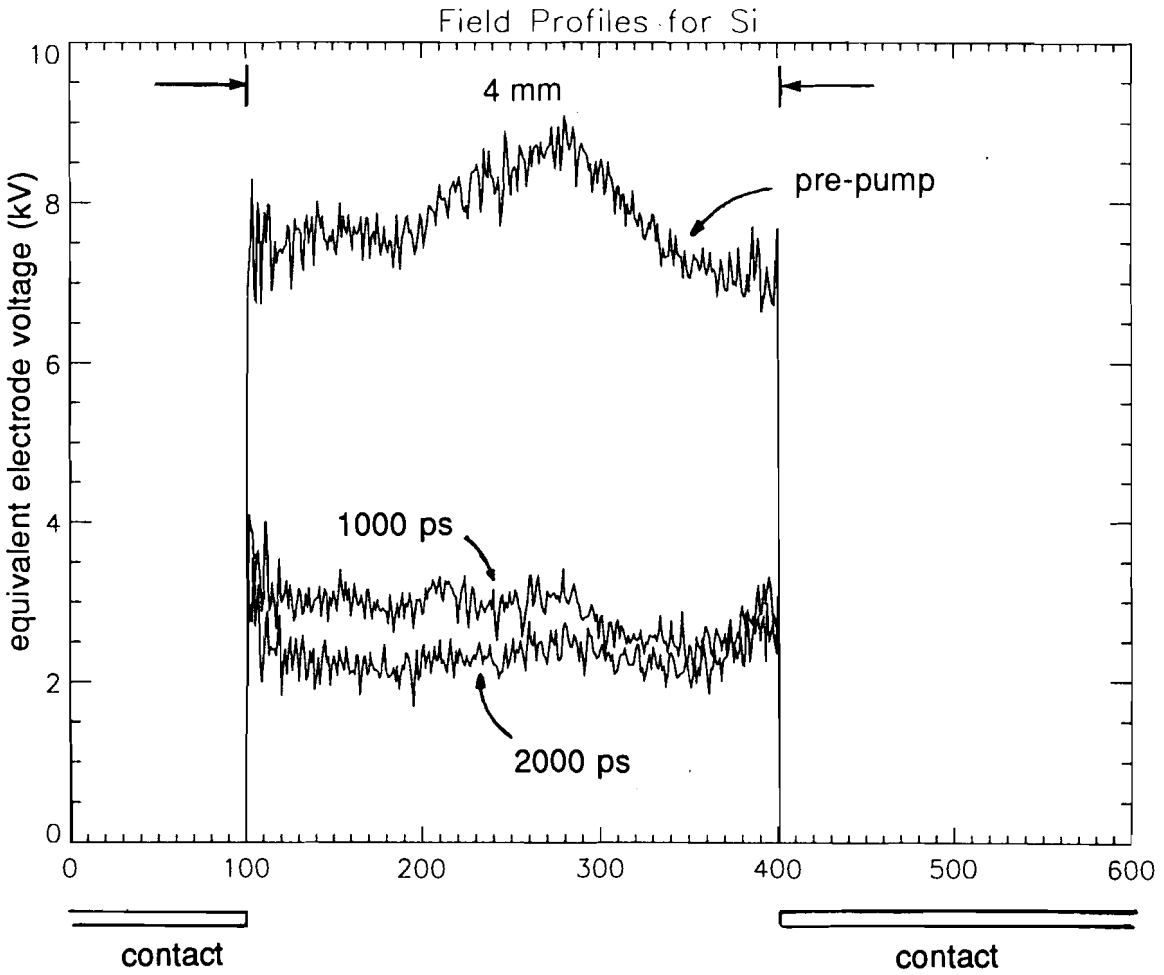

Fig.3.18 Electric field profiles along a line perpendicular to the contact pads on Si switch obtained from images like those in Fig.3.17 by averaging all 512 pixels along a line parallel to the pads. Note uniform collapse of field from pre-pump to 1000 ps after pump. The field remains collapsed out to the limit of this measurement, 2000 ps after pump.

CHAPTER 3

REFERENCES

[1] Z.H. Zhu, J-P. Weber, S.Y. Wang, and S Wang, "New Measurement Technique: CW Probing of Electric Fields," *Appl. Phys. Lett.* **49**, 432 (1986).

[2] Y.H. Lo, Z.H. Zhu, C.L. Pan, S.Y. Wang, and S. Wang, "New Technique to Detect the GaAs Semi-insulating Property- CW Electro-optic Probing," *Appl. Phys. Lett.* **50**, 1125 (1987).

[3] W.R. Donaldson, L.E. Kingsley, K. Meyer, and C. Bamber, "Semiconductor Contact Characterization Using Electro-Optic Sampling," *Conference on Lasers and Electro-optics Technical Digest Series 1987, Vol.14* (Optical Society of America, Washington, D.C.,1987) p.272.

[4] W.R. Donaldson, G. Mourou, L.E. Kingsley, and C. Bamber, "Characterization of High-Voltage Photoconductive Switches," *Digest of Technical Papers,* 6th IEEE Pulsed Power Conf., edited by B.H. Bernstein and P. Turchi (IEEE, New York, 1987) pp.141-144.

[5] W.R. Donaldson, L.E. Kingsley, "Electro-Optic Imaging Of Semiconductor Contact Fields," *Conference on Lasers and Electro-optics Technical Digest Series 1988, Vol.7* (Optical Society of America, Washington, D.C.,1988) pp.112-114.

[6] P.M. Hall, "Resistance Calculations for Thin Film Pattern," *Thin Solid Films I*, p. 277-295 (1967).

[7] L.E. Kingsley and W.R. Donaldson, "Electro-Optic Surface Field Imaging System," *Digest of Technical Papers,* 7th IEEE Pulsed Power Conf., edited by R. White and B.H. Bernstein (IEEE, New York, 1989) pp.376-379.

[8] L.E. Kingsley and W.R. Donaldson, " Two-Dimensional Electro-Optic Imaging," *Conference on Lasers and Electro-optics Technical Digest Series 1989, Vol.11* (Optical Society of America, Washington, D.C.,1989) pp.112-114.

CHAPTER 4

ELECTRO-OPTIC IMAGING OF HIGH-FIELD PHOTOCONDUCTIVTY IN GaAs SWITCHES

The electro-optic imaging system was used to investigate the collapse of the electric field in a GaAs photoconductive switches, both bulk and planar. The motivation for this work was to provide some insight into the mechanism for observed high-field effects in GaAs switches, such as the aforementioned lock-on behavior, and to provide an experimental basis for the evaluation of a model of GaAs switch operation.

I. BULK SWITCH OPERATION

1.IMAGING DATA

Bulk switches, also called vertical switches, are switches with the electrodes on opposite sides of a slab of semiconductor. Bulk switches were prepared and their operation characterized with the e-o imaging system [1,2,3], the probe set-up as in Fig.3.11. These switches were fabricated by depositing circular contacts of NiAu:Ge on opposite faces of 0.6 to 1 cm thick blocks of intrinsic GaAs. The GaAs was high resistivity material ($\rho \sim 10^7\ \Omega$ cm) supplied by MA-COM. The contacts consisted of a solid annulus surrounding a center region which was perforated with holes to allow light to pass through into the bulk of the GaAs. This resulted in a nonuniform carrier density profile that decreased exponentially through the bulk of the switch. The contact preparation was also varied with the 6 mm thick switches having an ion

implantation under the metalization to make ohmic contacts, the other samples having contacts deposited on bare GaAs. This switch design is of particular interest both for its applicability to the coaxial geometry [4] and for its relative immunity to surface breakdown, as a surface arc must travel out to the edge, down the side and back into the center—a very long physical path. The design is also useful in that this contact geometry allows for uniform fields which facilitate extraction of absolute field values, as opposed to the coplanar geometry which has a much more complicated field pattern. To access the fields between the contacts, this design has been modified by cutting the GaAs in a plane passing through the center of the contacts. The switch electrode configuration is shown in detail in Fig.4.1. These switches were obtained from the U.S. Army Electronics Technology and Device Laboratory.

Connection to the external circuit was made by pressure contacting copper electrodes coated with indium along the outside circumference of the NiAu:Ge electrodes. The Cu electrodes were bored out so that IR light could reach the switch contacts. By placing a dielectric beam splitter in the IR pump beam, approximately 50% of the IR light could be directed onto each electrode. Either of these beams could be blocked to investigate asymmetries in the response of the photoconductor. The arrival time of the two beams at the switch was adjusted to within 300 ps by monitoring the arrival of the switch pulse at the load with a 1 GHz analog oscilloscope. The dielectric beam splitter was mounted on a kinematic mount so that it could be removed and the full IR laser energy could be applied to one side of the switch. Thus, five illumination schemes were employed, considering that full energy could be applied to either the ground or high-voltage contact.

The bulk switches were mounted in a 50 Ω coaxial transmission line geometry using RG8 cable. Bias voltage was applied with a computer controlled 0 - 9.5 kV

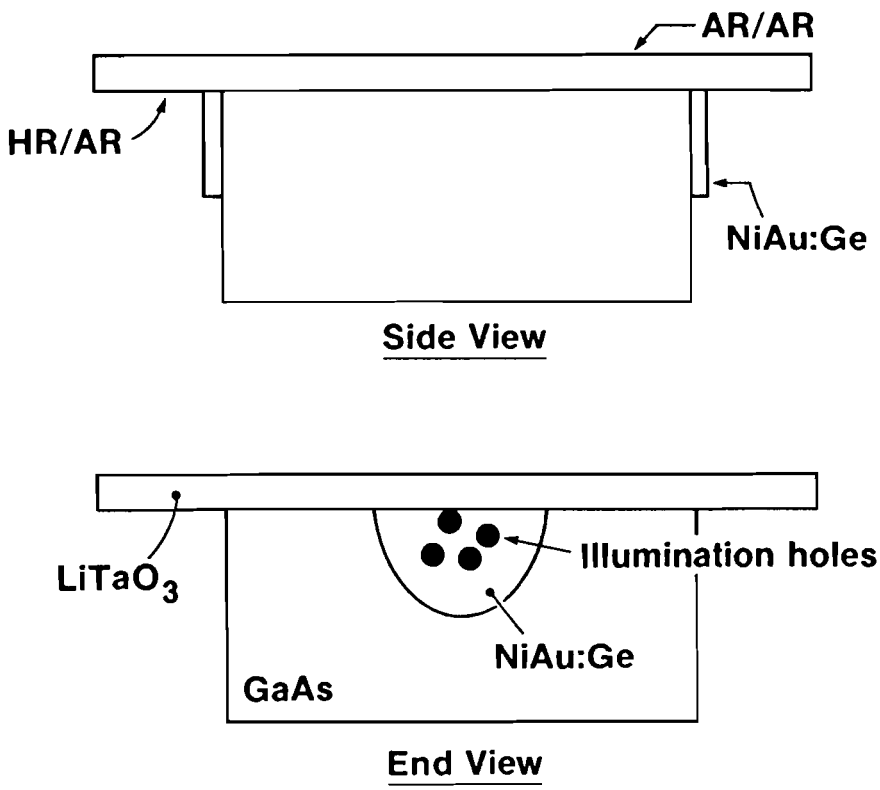

Fig.4.1 Bulk GaAs switch with mesh electrodes on opposite faces. The switch has been halved and a $LiTaO_3$ crystal is in place to measure the surface electric field between the contacts. The $LiTaO_3$ crystal has an anti-reflection (AR) coating for both 532 nm and 1064 nm light on the top surface. The bottom surface has a high-reflection (HR) coating for 532 nm and an AR coating for 1064 nm.

pulser. The switch was connected via the RG8 cable to a 50 Ω termination. The optical pulse width was ~200 ps for the bulk switch experiments.

Figs.4.2-4 show data taken for a 6 mm thick ion-implanted GaAs bulk switch. The images taken were normalized and scaled to equivalent electrode voltage (EEV). The true field is EEV divided by the gap distance (in this case, 6 mm). A typical e-o image is shown in Fig.4.2, which shows a 3-D plot of the surface field on the 6-mm GaAs switch illuminated simultaneously through both contacts, 800 ps after initial illumination. Each contact received ~ 50 μJ of optical energy for a pump intensity of 1.9 mJ/cm^2. The left edge of the image corresponds to the negative high-voltage contact, and the right side to the ground contact. The active area in the center is 6 mm wide, and the front and back edges of the image are 10 mm apart and correspond to the edges of the deposited electrodes. Outside the region between the contacts, the field falls abruptly to zero because there is no tangential component of the electric field at the surface of a conductor. Noise spikes in that region of the image have been artificially suppressed. Initially, the image was uniform between the contacts. The infrared light has caused the field to collapse. The center section of the image is where the 2 mm wide pump beam illuminated the GaAs. Note that the field has collapsed over most of the active region to a value of ~ 0.3 kV EEV although the bias voltage is 5 kV. The field collapses uniformly on the ground side of the image but it has areas of significant enhancement on the high-voltage side. There are two significant high-voltage spikes of ~3 kV EEV even though most of the switch field has collapsed. These spikes are located at the very edges of the high-voltage contact. A survey of all the images that have been acquired reveals that this is a general feature independent of the contact preparation. There is always an enhancement at the

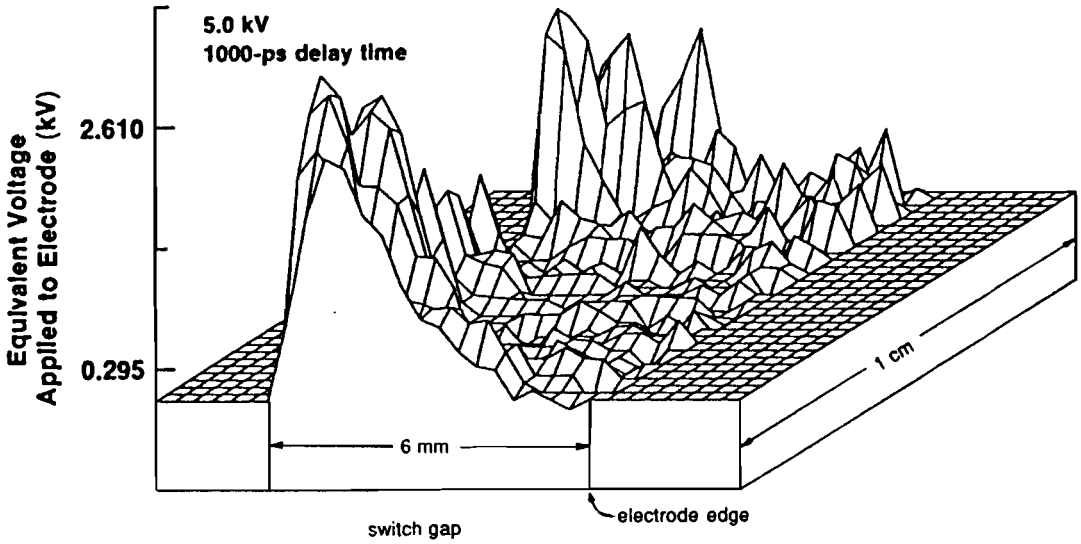

Fig.4.2 The electro-optic image of the surface electric field on a GaAs switch 800 ps after illumination by a 200 ps IR pulse through both of its electrodes. The left side of the image corresponds to negative high voltage electrode. The active area is 6 mm by 10 mm and the field enhancements are located behind the solid portion of the high voltage contact.

high-voltage contact. The enhancement can be alleviated at the perforated region of the contact by illuminating with more IR light, but the field collapse is never as complete as on the ground side.

Figs.4.3 and 4.4 show a series of 3-D plots of the field above a 6-mm GaAs switch. These illustrate the progressive collapse of the surface field in time for two different bias voltages. Both contacts were illuminated simultaneously with ~ 50 μJ of IR. In Fig.4.3, the switch bias was 5 kV; in Fig.4.4, 9 kV. The field is given in EEV. The time is relative to the IR translation stage position; 0 ps is the arrival of the IR pulse and the stage can scan out to 1 ns after IR illumination begins. At -200 ps, the field across the switch is essentially uniform, as expected. As time progresses, the field collapses. For 5 kV bias, the collapse is almost complete, except for the enhancement near the contacts. At 9 kV, the situation is much different: the field collapses only to ~ 3 kV EEV: there is still a field of ~5 kV/cm across the switch, 1 ns after illumination.

Fig.4.5 shows a series of lineouts from the surface field images of the 6 mm GaAs switch, taken through the center of the image, perpendicular to the contact faces. These illustrate the progressive collapse of the surface field in time for various illumination schemes. Switch bias was 8 kV. Single-side illumination is characterized by a wave front that propagates across the switch. In Figs.4.5(a) and 4.5(b), the field collapses from the illuminated contact to the nonilluminated contact in time as the region of conduction propagates from the region of photogeneration. For both-side illumination, Fig.4.5(c), the field collapses more quickly and to a lower final value than for single-side illumination, as in Figs.4.5(a) and 4.5(b). Switch rise time is faster and the efficiency is higher for illumination through both contacts, an

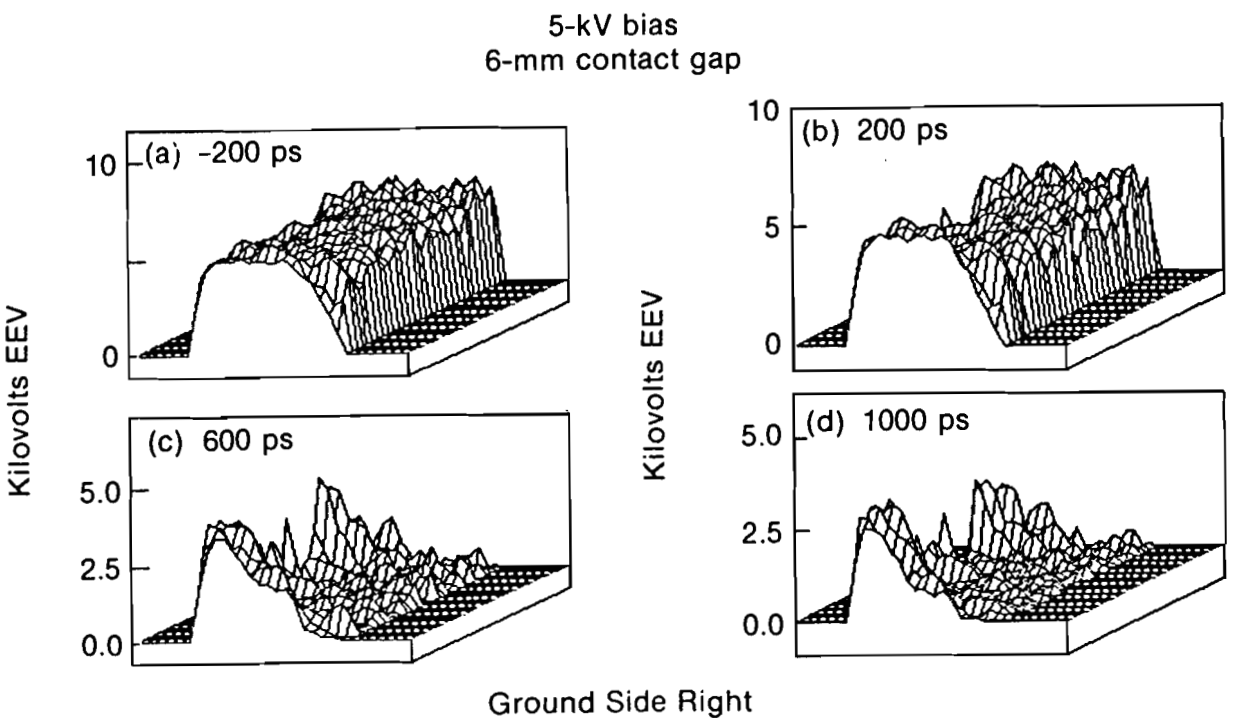

Fig.4.3 Temporal evolution of electric field above 6 mm thick bulk GaAs switch illuminated by 200 ps IR pulse through both contacts. Switch biased at 5 kV. Images processed and scaled to equivalent electrode voltage (EEV). The active area of the image is 6 mm by 1 cm. The collapse of electro-optic field proceeds from the essentially uniform profile shown in (a).

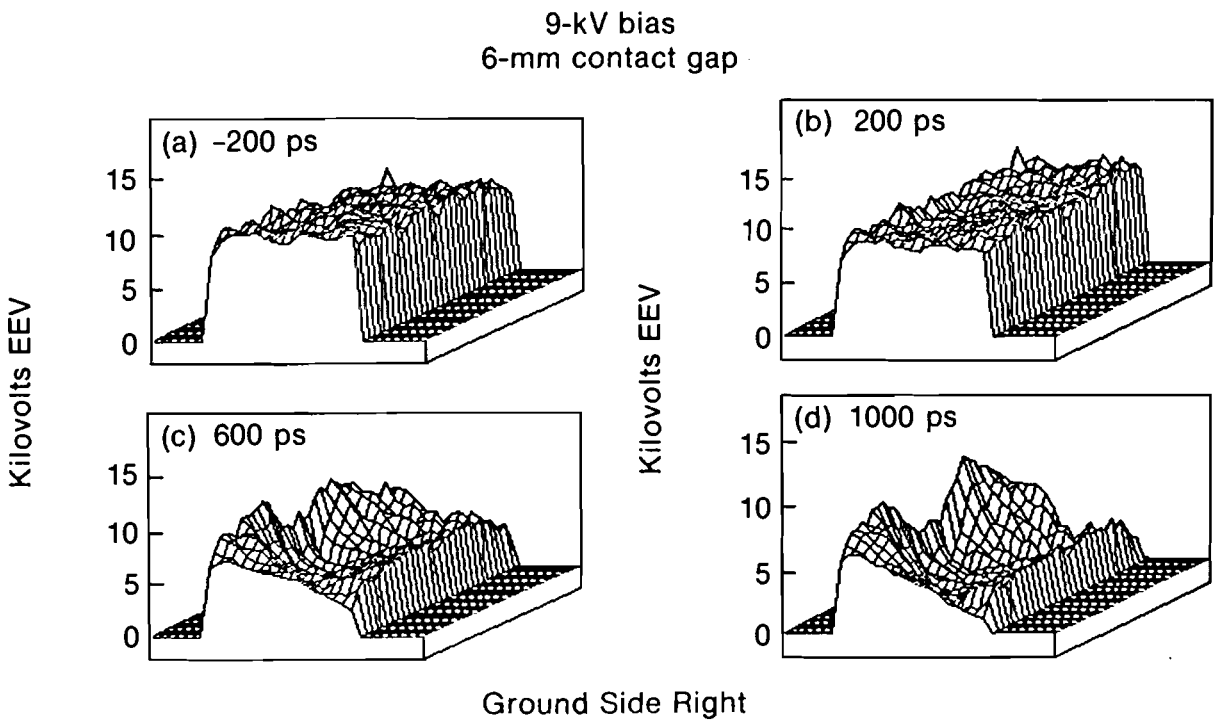

Fig.4.4 Same conditions as in Fig.4.3 except switch biased at 9 kV. The incomplete collapse of field is evidenced by ~5 kV/cm field remaining across switch after 1000 ps.

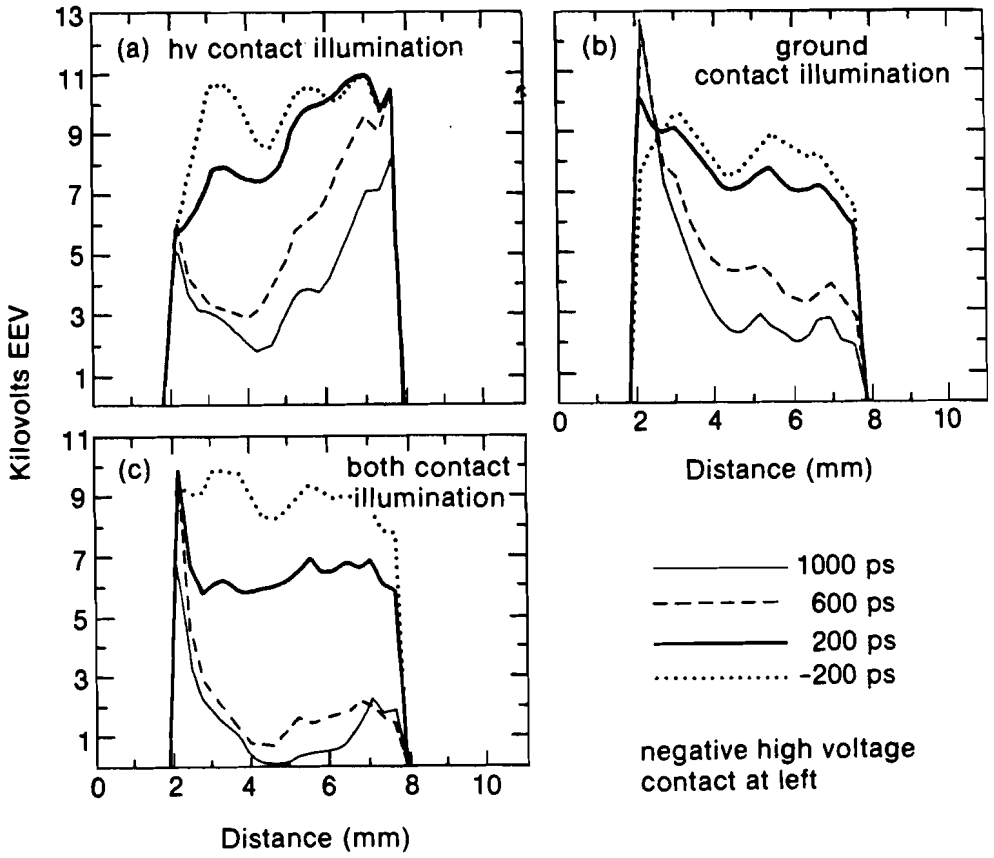

Fig.4.5 Temporal evolution of electric field above 6 mm thick bulk GaAs switch for different illumination conditions. Switch biased at 8 kV. Lineouts taken through center of processed electro-optic image at different times after illumination with 200 ps IR pulse. Greater efficiency and speed are obtained for illumination through both contacts.

important engineering consideration. The field enhancement exhibited in Figs.4.2, 4.3 and 4.4 can also be observed in these lineouts. Small differences in the - 200 ps lineouts may be due to the small prepulses which excite the switch before the main IR pulse arrives, as well as the laser intensity fluctuation (~10%).

Some of these observations can be made more quantitative by defining an electro-optic switching efficiency. A standard measure of switching efficiency would be what fraction of the quasi-dc bias is switched to the load. A perfectly efficient switch would be driven completely conductive and the bias voltage would appear across the load. No electric field would remain across the switch electrodes. If the electric field across the switch is imaged electro-optically, an electo-optic switching efficiency, η, can be defined:

$$\eta = \sum_N \eta_{ij} = (1/N) \sum_N (E'_{ij} - E_{ij}(t)/E'_{ij}) \tag{4.1}$$

where the summation is over the total number of active pixels (pixels outside the electrode gap have been ignored). E'_{ij} is the electro-optic image element with no IR light present and $E_{ij}(t)$ is the electro-optic image element at a time delay t as determined by Eq.(3.1). The restrictions on the summation are that if

$$E'_{ij} - E_{ij}(t) < 0 \tag{4.2}$$

corresponding to a field enhancement , η , was set equal to zero (i.e., it was considered to be an element that had not undergone switching) and if

$$E'_{ij} - E_{ij}(t) > E'_{ij} \tag{4.3}$$

implying a negative oscillation in the surface electric field, the efficiency at that point, η, was set equal to one. The parameter η is a measure of how much of the dc surface field has been switched, and would equal the real switch efficiency if it were possible to integrate through the entire switch volume. This is impossible for these experiments. The quantity η tells us what is happening at only one plane of a 3-D device, but is the best available measure of the internal dynamics of the switch. Fig.4.6 shows the electro-optic efficiency as a function of the optical delay line setting for several applied fields in the case of two-sided illumination. The most striking feature of this graph is that the switching efficiency drops as the field increases. Fig.4.7 shows that this trend continues with single-side illumination at two different IR intensities. For example, at an illumination intensity of 2.1 mJ/cm^2, there is sufficient light to switch a field of 6.6 kV/cm with 90% efficiency. At the same intensity, a field of 15 kV/cm is switched with only 40% efficiency. Fig.4.7(a) shows that increasing the intensity to 3.8 mJ/cm^2 increases the efficiency to only 50% at 15 kV/cm. The rise time of the switch also decreases as the light intensity is increased.

2. DISCUSSION OF BULK SWITCH DATA

A number of important features about how GaAs photoconductive switches operate can be discerned from this work. The first is that the electric field is enhanced at the negative high voltage electrode and collapses most slowly there. This type of behavior was seen in both types of contacts tested. In particular, the enhancement was strongest under the solid portion of the high voltage contact. A corresponding enhancement was not observed on the ground side electrode (positive with respect to the high-voltage pulse). This enhancement was reduced in the perforated region by

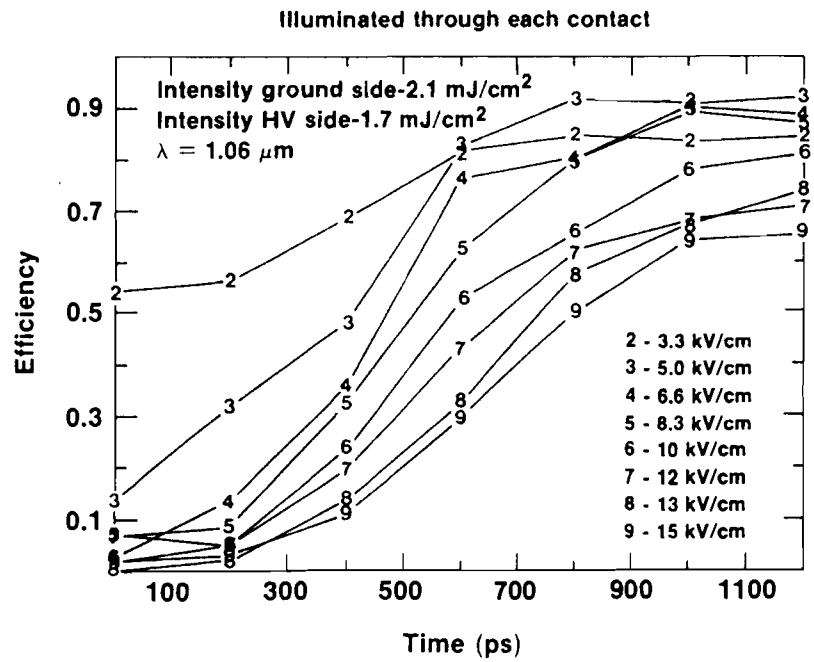

Fig.4.6 The electro-optic efficiency for a 6 mm bulk GaAs photoconductive switch illuminated through both contacts as a function of time. The efficiency decreased with increasing field.

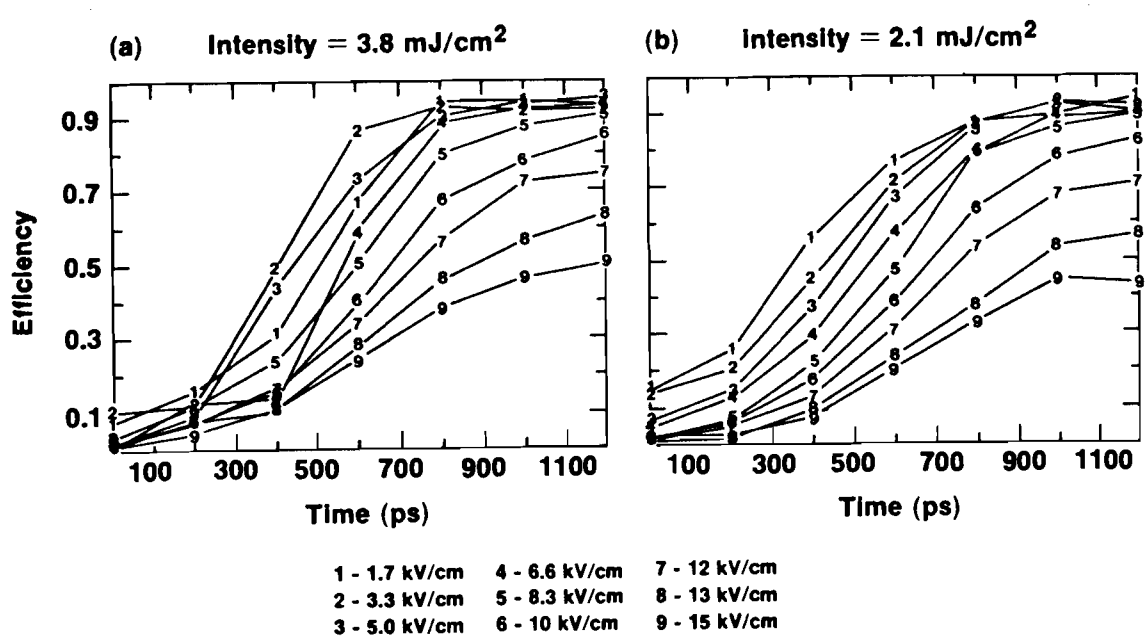

Fig.4.7 The electro-optic efficiency of a GaAs photoconductive switch illuminated through only the high voltage contact; (a) 3.8 mJ/cm^2 (b) 2.1 mJ/cm^2.

increasing the light incident on the high voltage contact and was seen in all samples; it showed some increase with the numbers of shots applied to the sample. Thus, some of the nonuniform enhancement is associated with the long term degradation of the contact (>2 x 10^4 laser shots) due to arcing from the perforated region to the solid region of the Ni:AuGe contact. This arcing only occurred if the GaAs was switched. These observed field enhancements are consistent with our simulations of bulk switches with through-the-contact illumination. Based on our simulations of the effects of non-ohmic contacts on bulk switch operation, we conclude that the persistent field enhancement at the cathode was due, in part, to the fact that the mesh electrode had alternating areas of ohmic and current-blocking contacts.

It was seen that the switching efficiency of GaAs decreased with increasing voltage out to a time ~1 ns after illumination. Increasing the number of carriers by increasing the IR illumination energy by a factor of ~2 does not significantly improve the electro-optic switching efficiency. This suggests that this is predominantly a field effect and not due to the illumination scheme. This is confirmed by the observation that, for a given bias voltage, the switching efficiency increases with increasing electrode spacing. The switching efficiency should not be a function of the bias voltage if the mobility is not a function of field. For a switch mounted in a transmission line geometry, the voltage switched to the load, V_L, is given by Eq.(1.8) as:

$$V_L = \frac{Z}{2Z + r} V_{BIAS} \tag{4.4}$$

where r is the switch resistance, V_{BIAS} is the bias voltage, and Z is the impedance of the matched bias and load cables (50 Ω). The switch resistance, r, is given by

$$r = \frac{\text{voltage across switch}}{\text{switch current}} = \frac{E\ell}{JA} \tag{4.5}$$

where J is the total current density, ℓ is the electrode gap spacing, and A is the illuminated area of the contact. J can be written $J = ne\mu E$, with n = the density of photogenerated carriers, e is the electronic charge, and μ is the sum of carrier mobility for bipolar conduction carrier mobility. The electrical switching efficiency, V_L / V_{BIAS}, is then:

$$\frac{V_L}{V_{BIAS}} = \frac{Z}{2Z + \frac{\ell}{Ane\mu}} . \tag{4.6}$$

There is no explicit field dependence in Eq.(4.6). Field dependence can only enter through the mobility, μ. Eq.(4.6) can be verified by measuring the current at the load, I_L, versus bias voltage. Since

$$I_L = \frac{V_L}{Z} = \frac{1}{2Z + \frac{\ell}{Ane\mu}} V_{BIAS} . \tag{4.7}$$

I_L should be a linear function of V_{BIAS} for a given optical pump energy, as the carrier density is proportional to the optical pump energy. Fig.4.8 illustrates results from measurements of I_L versus V_{BIAS} for various optical energies. The linear relationship between I_L and V_{BIAS} is verified for bias voltage up to 5 kV, as shown in Fig.4.8(a). Fig.4.8(b) gives I-V curves for bias voltages up to 9 kV. The I-V curves deviate from linear behavior at high bias (>6 kV): the switch on-state resistance increases as the bias increases. This deviation from linearity coincides with the onset of negative differential resistance (NDR) in GaAs. Above ~ 3.2 kV/cm, the electron drift velocity in GaAs decreases as the electric field increases. Since the current is proportional to the drift velocity, this represents an effective increase in switch on-state resistance as

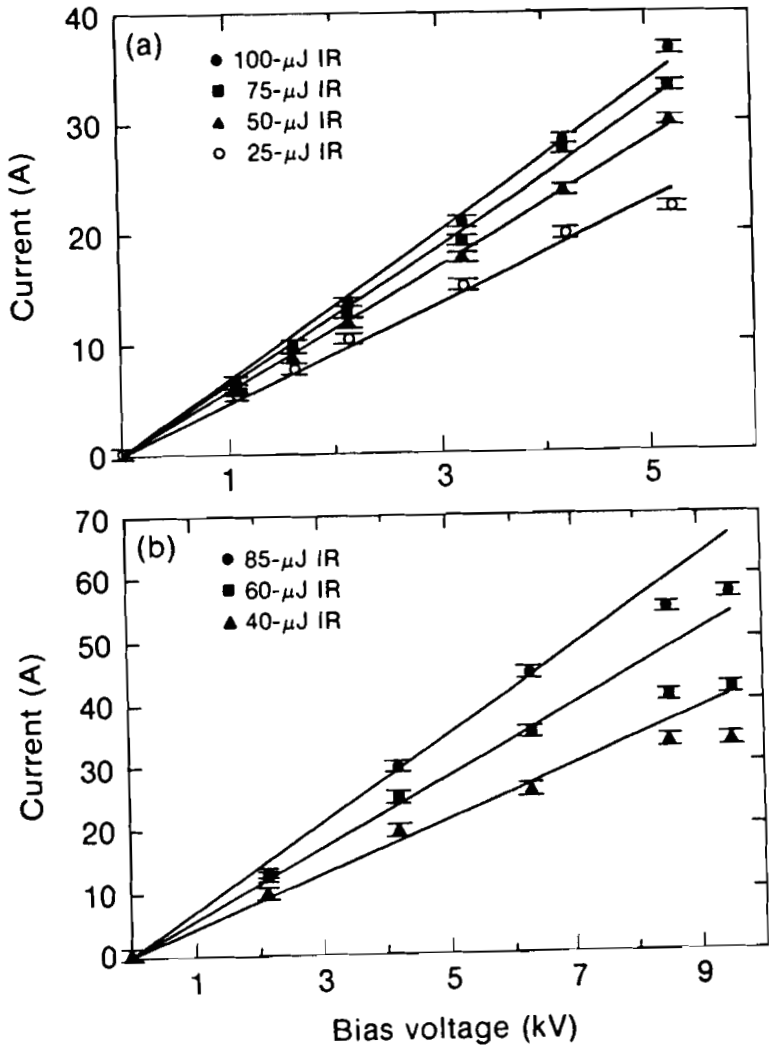

Fig.4.8 The load current versus bias voltage for various IR pump energies; (a) bias up to 5 kV; (b) bias up to 9 kV.

the field increases above ~ 3 kV/cm and, therefore, we should not expect and do not see a continuation of the linearity between voltage and current. Thus, we have evidence to suggest the observed decrease in switching efficiency with increasing voltage is due to NDR, although the I-V measurements lack the temporal resolution of the imaging data. This observation has important implications for the use of photoconductive switches in pulsed power applications. In many cases, the trend has been to push the breakdown limit in these devices to achieve the highest switch electrical energy for the minimum optical energy. Our results indicate that switches with longer gaps, and lower field may be more efficient in terms of switched voltage to pump energy, at least in the purely photoconductive mode of switching for pulse durations of the order of 1 ns.

II. PLANAR SWITCH STUDY

1. MOTIVATION

GaAs surface switches were also investigated using the surface field probe geometry of Fig.3.10; the principal focus of this work was the investigation of lock-on behavior in GaAs [5]. As discussed in Chapter 1, in GaAs the photo-generated electron hole pairs should recombine in about 1 ns. This should limit the duration of electrical pulses delivered with GaAs switches. Lock-on is the phenomenon where GaAs switches remain in the conducting state for a long time (hundreds of nanoseconds) after the optical excitation. This phenomenon was first reported by G. Loubriel *et al* in 1987 [6,7]. It was observed that GaAs has two modes of operation. There is a low-field, or linear mode, where the voltage across the switch drops to zero as the laser pulse is applied, and after the laser pulse, the voltage recovers as the photogenerated carriers recombine at their characteristic rate. There is also a high-

field, or nonlinear mode, where the switch voltage drops to zero during the laser pulse duration and tries to recover but does not regain its initial value. Instead, it locks on to some intermediate value, called the "lock-on" voltage, which is independent of the bias voltage for a given sample. This is a field dependent effect. The bias field has to be greater than a threshold value of 3 to 8 kV/cm for lock-on to occur. This threshold depends on the material preparation. In the lock-on state the voltage dropped across the sample is linearly proportional to the distance across which the voltage is dropped, the electrode spacing. Lock-on behavior has several interesting features, as reported by Zutavern : it can be triggered with very low light levels, ~1/500 the amount required to switch the same samples in the linear mode, therefore requiring some carrier gain mechanism; it requires light triggering, as biasing GaAs up to 140 kV/cm in the dark does not result in significant conduction; it persists for as long as the external circuit can provide current, maintaining the lock-on field across the switch [8].

The mechanism for lock-on is not understood. The threshold bias field for lock-on, 3 - 8 kV/cm, roughly corresponds to the threshold field for negative differential resistivity (NDR) in GaAs, and this suggests some connection between the two effects. Also, lock-on has been reported in Fe:InP, another semiconductor exhibiting NDR, and lock-on is not observed in Si or Au:Si, materials which do not exhibit NDR [9]. The Gunn effect alone can not be responsible for lock-on as it does not create carriers. An unknown carrier-generating process somehow connected to the Gunn effect may be responsible for lock-on. It is known that NDR can result in the formation of high-field regions (or Gunn domains) in GaAs which repeatedly traverse the sample from the cathode to the anode [10]. For a given sample length, ℓ, the carrier density, n, in the sample must reach a critical value before domain

formation occurs. The product of the sample length and carrier density, $n\ell$, obeys the relationship [11]

$$n\ell > 10^{12}\,\mathrm{cm}^{-2} \tag{4.5}$$

Propagating domains have been observed in samples of GaAs that were heavily doped to reach the critical carrier concentration, and domain formation is the basis for the well known Gunn diode [12]. Carriers can be generated in these high-field regions through impact ionization whereby electrons are accelerated by the high fields to sufficient energy (~2 eV) to create more electron-hole pairs and seed an avalanche, if the domain field is high enough (100-200 kV/cm). This effect can be explained by a phenomenological argument if we assume that at sufficient average field, a low light level trigger pulse supplies the critical carrier concentration for high-field domain formation. Avalanching produces the carriers which explain the trigger gain. If too many carriers are created, the resistance of the switch drops too low for the circuit to supply the lock-on field across the switch. Then the domains disappear and normal carrier recombination occurs [8].

This model does explain qualitatively some of the observed features of lock-on, including light trigger dependence, field dependence, and onset of lock-on during recovery of switch. It is dependent on the formation of Gunn domains in a GaAs photoconductive switch, an effect which had not previously been experimentally observed or predicted by a detailed theory. There is also some circumstantial evidence for the repeated formation of Gunn domains in GaAs switches in reports of current oscillations during switch operation [13], a behavior similar to a Gunn diode. We used the e-o imaging system to investigate the dynamic behavior of the electric field of a GaAs switch in the lock-on regime, one goal being to establish the existence of high-field regions during switch operation.

2. PLANAR SWITCH DATA AND DISCUSSION

The GaAs switches used in the lock-on study were supplied by Sandia National Laboratory. They had two rectangular Ni:AuGe contact pads, 2.5 mm wide, and had an electrode spacing of 2.5 mm. The switches had an electron mobility of 7000 cm^2/volt-sec, an impurity concentration of 10^7 cm^{-3}, and an expected lock-on threshold of 4 kV/cm. To eliminate any complicating effects due to impurity concentrations, the photoconductive switching was done with 532-nm laser pulses (FWHM ~140 ps),which have an energy greater than band gap allowing for direct band-to-band photoexcitation. The e-o probe pulses were infared. The switches were installed in the switch holder used for the Si imaging discussed in Chapter 3. All switching experiments were performed with the switch under a pressure of ~50 psi SF_6.

The lock-on behavior of the switch is seen clearly in Fig.4.9, which shows oscilloscope traces of the switched output for bias voltage close to the lock-on threshold, 2.0 kV, and above the lock-on threshold, 3 kV. At 2.0 kV bias, the switch exhibits linear behavior, switching voltage only for a time consistent with normal recombination. At 3 kV bias, lock-on behavior is observed, with the switched output decaying normally until, at the onset of lock-on, the output voltage "restarts" for a second period of conduction lasting as long as the charging circuit supplies charge. Note that the lock-on effects occur several nanoseconds after the optical trigger pulse. To image the field during this period, the measurements were taken out to 6 ns after the trigger. A 6 ft optical rail was used in the pump delay line and the retroreflector was moved manually to obtain imaging data at this long delay. It was extremely difficult to maintain consistent illumination of the sample for delays longer than 6 ns due to the extremely long optical path.

a)

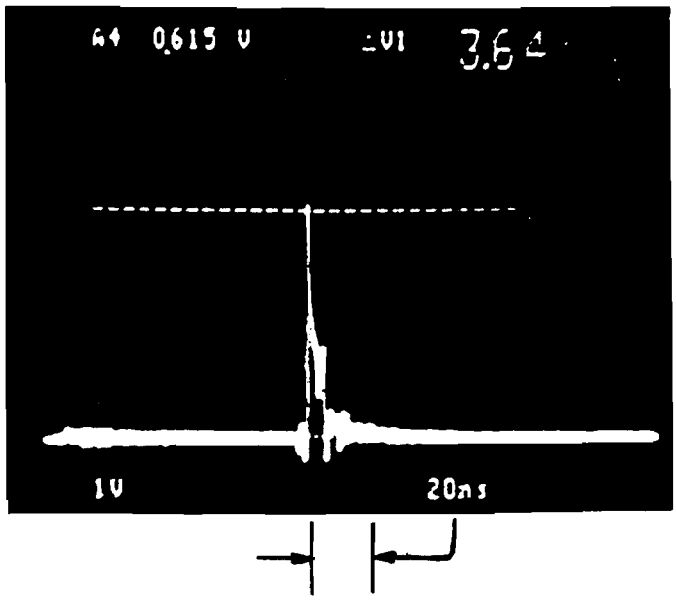

b)

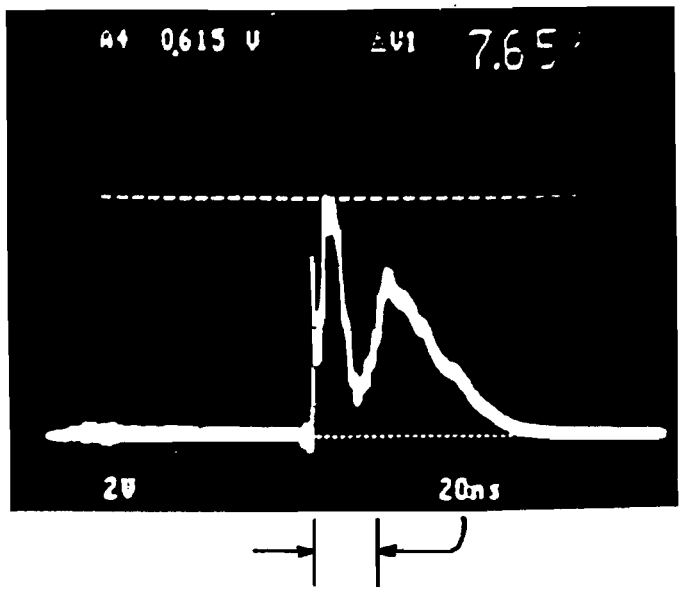

Fig.4.9 Oscilloscope traces of switched output waveform of planar GaAs switch monitored at the load using current probe for (a) -2.0 kV bias, just at lock-on threshold; and (b) -3.0 kV, above lock-on threshold. The time scale is 20 ns/div.

The e-o imaging measurements reveal a very complicated behavior. If one looks at the electric field averaged over the whole active area of the switch, two distinct patterns emerge. Below the threshold for lock-on, the field collapses uniformly in roughly the full width half maximum (FWHM) of the laser pulse. The rapid collapse is followed by a rapid recovery of the order of a few hundred picoseconds followed by a slower recovery to the initial bias field in about 5 ns. This trend is illustrated in Fig.4.10, which shows the average electric field along a line parallel to the contacts at the center of the contact gap for a switch bias of 2.5 kV (10 kV/cm).

Above the threshold for lock-on the behavior is more complicated. The field collapses and starts to recover as in the below-threshold case. However, at about 1 ns after the pump pulse, the field begins to collapse again. The second collapse of the electric field across the switch is much slower than the first, optically induced, collapse. It is also not monotonic. An oscillatory structure is superimposed on the decay of the electric field. Fig.4.11, which is similar to Fig.4.10, illustrates the gross features described above, switch bias 6 kV (24 kV/cm). This second decrease in the electric field is apparently associated with the lock-on state. Oscilloscope traces for a current probe at the output of the switch biased at 6 kV were similar to Fig.4.9(b), indicating that conduction through the switch continued longer than would be expected from that determined by the recombination of the electron-hole pairs. The data shown in Fig.4.11 represents the first measurement of the timescale for the onset of lock-on in a photoconductive switch, which is ~ 1 ns.

The temporal evolution of the spatial profile of the electric field above the switch is shown for bias voltages of 2.5 kV and 6 kV in Figs.4.12 and 4.13, respectively. In both figures, the field collapses in about the 140 ps FWHM of the

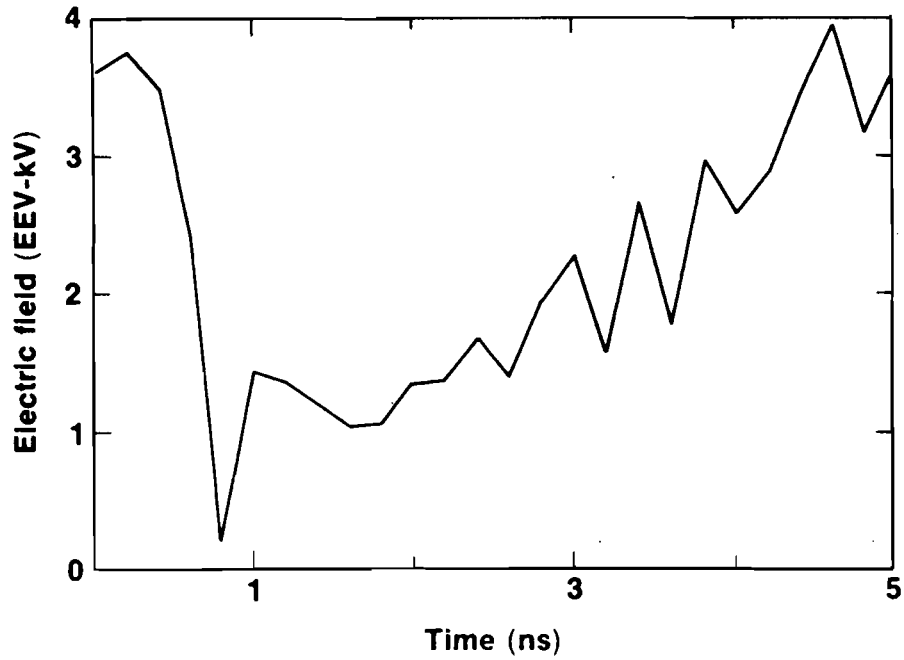

Fig.4.10 Average electric field above active area of planar switch as a function of time at -2.5 kV bias voltage, just below lock-on threshold for this sample. Each data point in this plot is an average over all pixels in the active region of the electro-optic field image.

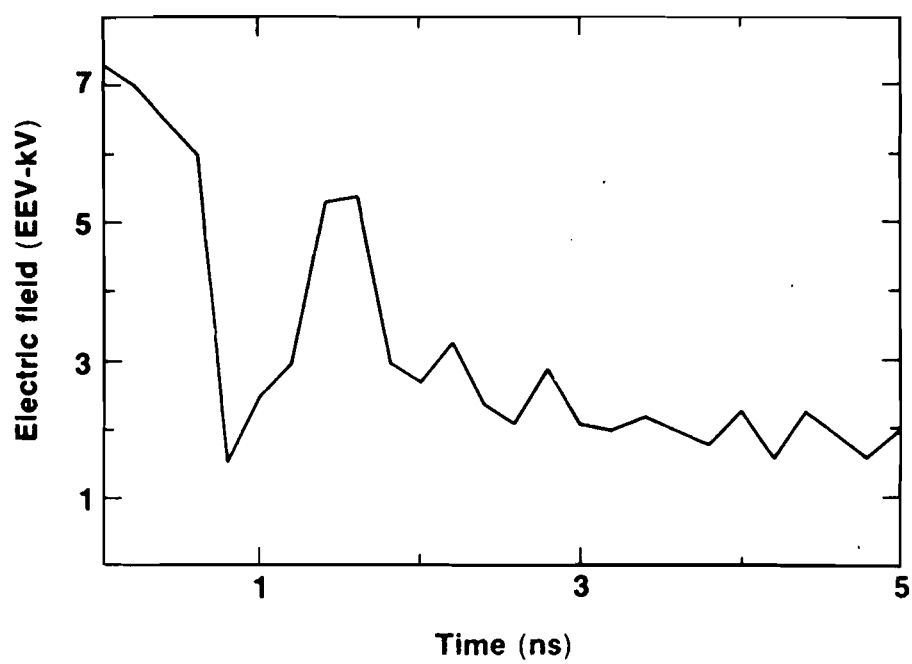

Fig.4.11 Average field versus time , as in Fig.4.10, at bias of -6 kV, above lock-on threshold.

pump pulse, collapsing most rapidly in the center of the gap. This rapid collapse in the switch center is much more than would be expected from the ~10% contact-to-contact spatial variation in pump energy due to the Gaussian profile of the pump. As the field recovers due to carrier recombination, the field at the negative high-voltage contact (the cathode) rises most quickly, forming a local region of high field. This is most pronounced at 6 kV bias (above lock-on), where the high-field domain can be seen to be extending from the cathode, propagating across the switch.

These graphs reveals only a small portion of the complex behavior of these devices. Fig.4.14 shows three different electro-optic images at different times after illumination. The images have been manipulated so that a dark region in the active switch area indicates the absence of an electric field greater than 16 kV/cm. A white region indicates the presence of an electric field greater than 16 kV/cm. Fig.4.14(a) shows the electric field at the peak of the photo-induced conductivity. The active area of the switch is uniformly black, indicating complete switching, and the edges of the contacts are clearly delineated. At time beginning about 1 ns after complete switching has occurred the electric field develops a 2-D structure. In some places the field has collapsed and in other places it has increased to values which may even be greater than the original applied field. In Fig4.14(b), which occurs .8 ns after Fig.4.14(a), the electric field is concentrated near the high voltage contact. This image is 400 ps in time after the lineout in Fig.4.13 at 1200 ps showing the propagating domain. This then evolves into the state shown in the last image, Fig.4.14(c). A region of low field, which indicates the presence of carriers in the underlying semiconductor, extends out from the low voltage contact. This corresponds to a local region of high conductivity extending across the switch. Note that this region is only about 25% of

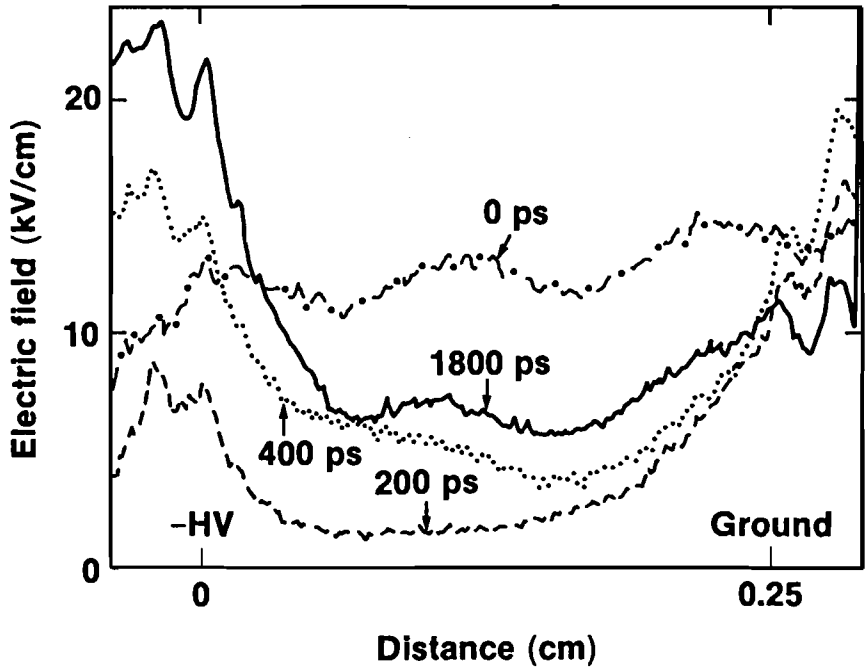

Fig.4.12 Electric field spatial profiles above planar switch along a line between the switch contacts at different times during switch operation. This plot was obtained from the full electro-optic image by averaging over 100 pixels along a direction parallel to the contact edge. The switch bias was -2.5 kV (10 kV/cm). 0 ps is just before pump pulse arrival. Note field enhancement at contact edges at 0.0 cm and .25 cm.

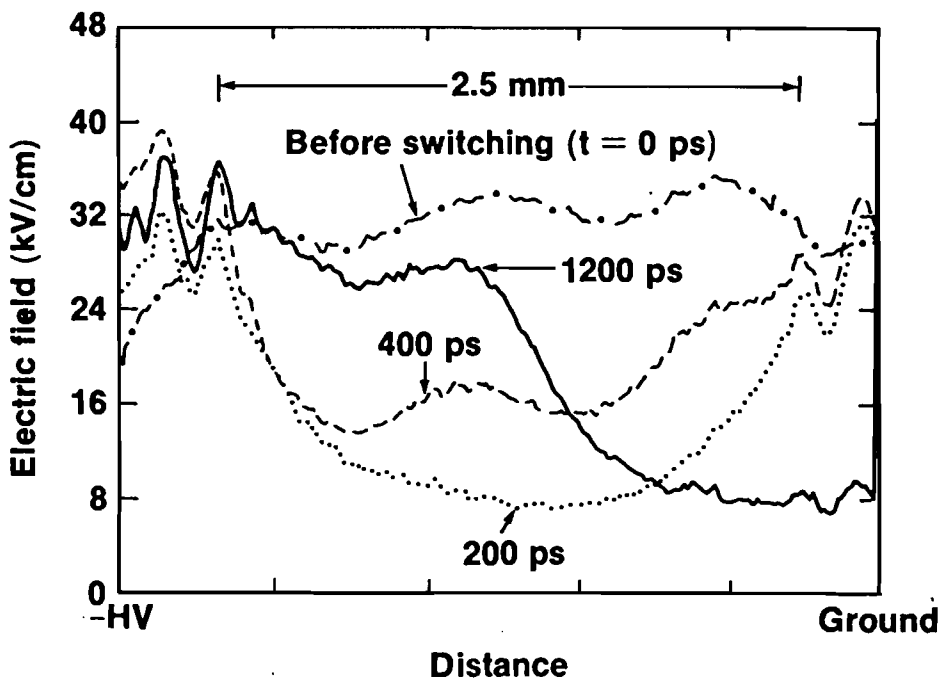

Fig.4.13 Electric field profiles at different times, as in Fig.4.12, switch bias -6 kV (24 kV/cm). Note high-field domain extending from cathode.

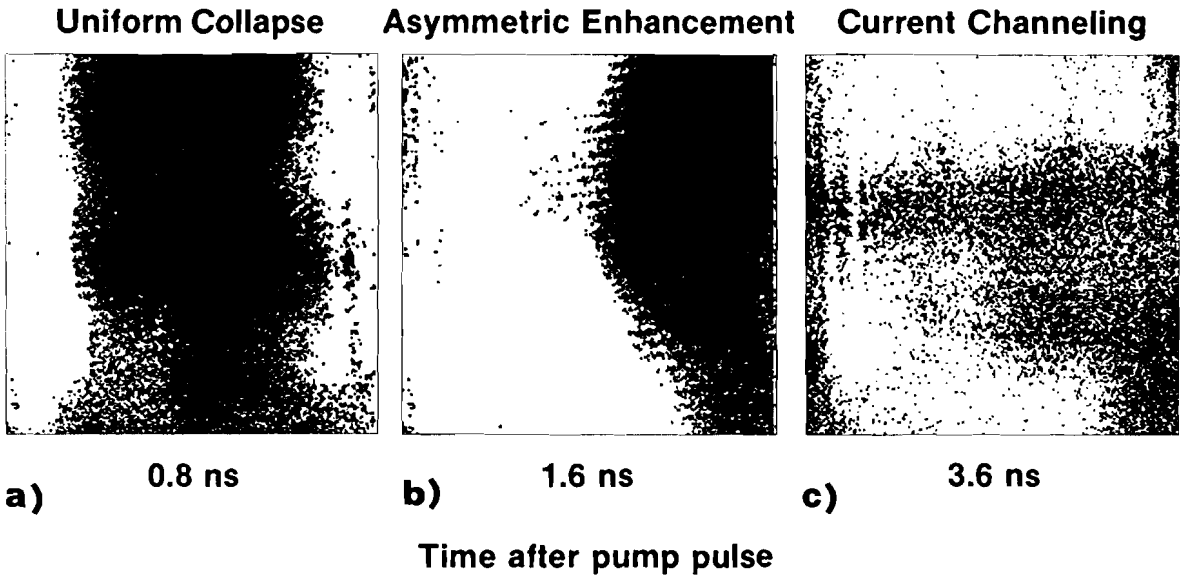

Black < 16 kV/cm; white > 16 kV/cm

d) contact layout

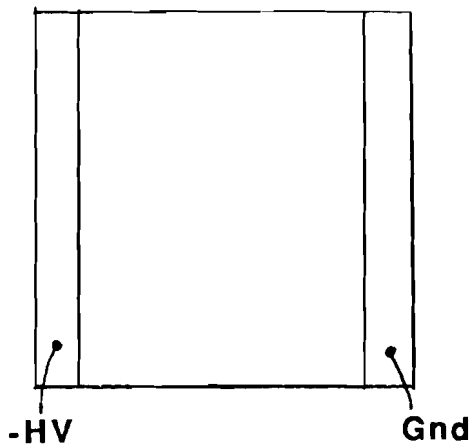

Fig.4.14 Electro-optic images at different times during planar switch operation. The images have been processed so that white corresponds to field >16 kV/cm and black is < 16kV/cm. Time is relative to pump pulse arrival. The image progresses from complete switching in (a), to formation of high-field domain (b), to channels of low field (c). The contact layout is also shown, (d).

the active area of the switch and may indicate that the current is being carried in channels through the switch in the lock-on regime.

The images in Fig.4.14 are representative of the many images taken of the GaAs switch operation. A survey of all the images show that the field is changing everywhere in the switch gap, with a preponderance of the images showing field domains at the cathode and indications of current channeling. As previously discussed, high-field domain formation is associated with NDR in GaAs. Current channeling, also, is a manifestation of NDR [12]. From the imaging data, we observe that above the lock-on threshold bias voltage (the 6 kV data), high-field domains develop at the switch cathode during the switch recovery and there are indications that the switch current is being carried in channels. We conclude that these effects are caused by the NDR in GaAs, which is verified by the computer-assisted analysis discussed in Chapter 5.

CHAPTER 4

REFERENCES

[1] L.E. Kingsley and W.R. Donaldson, "Electro-Optic Imaging of Surface Electric Fields in High-Power Photoconductive Switches," *IEEE Trans. Elect. Dev.*, **ED-37** (12) 2449 (1990).

[2] W.R. Donaldson, L.E. Kingsley, M. Weiner, A. Kim, and R. Zeto, "Electro-optic Imaging of the Internal Fields in a GaAs Photoconductive Switch," *Jour. Appl. Phys.* **68** (12) 6453 (1990).

[3] L.E. Kingsley and W.R. Donaldson, "Optical Probing of Semiconductor Carrier Dynamics," *Conference on Lasers and Electro-optics Technical Digest Series 1990, Vol.7* (Optical Society of America, Washington, D.C.,1990) p.150.

[4] L. Bovino, T. Burke, R. Youmans, M. Weiner, and J. Carter, "Recent Advances in Optically Controlled Bulk Semiconductor Switches," *Digest of Technical Papers*, 5th IEEE Pulse Power Conf., edited by P.J. Turchi and M. F. Rose (IEEE, New York, NY, 1985), p.242-245.

[5] W. Donaldson and L. Kingsley,"Optical Probing of Field Dependent Effects in GaAs Photoconductive Switches," SPIE Symposium on Laser Science & Optical Applications, OE/Boston '90, 4-9 November 1990 (proceedings to be published).

[6] G.M. Loubriel, M.W. O'Malley, and F.J. Zutavern, "Toward Pulsed Power Uses for Photoconductive Switches: Closing Switches," *Digest of Technical Papers,* 6th IEEE Pulsed Power Conf., edited by P.J. Turchi and B.H. Bernstein (IEEE,New York, 1987) pp.145-148.

[7] F.J. Zutavern, G.M. Loubriel, M.W. O'Malley, "Recent Developments in Opening Photoconductive Semiconductor Switches," *Digest of Technical Papers,* 6th IEEE Pulsed Power Conf., edited by P.J. Turchi and B.H. Bernstein (IEEE,New York, 1987) pp.577-580.

[8] F.J. Zutavern, G.M. Loubriel, B.B. McKenzie, M.W. O'Malley, R. A. Hamil, L.P. Schanwald, H.P. Hjalmarson, "Photoconductive Semiconductor Switch (PCSS) Recovery," 7th IEEE Pulsed Power Conf., edited by R. White and B.H. Bernstein (IEEE, New York, 1989) pp.412-417.

[9] G.M. Loubriel, F.J. Zutavern, H.P. Hjalmarson, and M.W. O'Malley "Closing Photoconductive Semiconductor Switches" *Digest of Technical Papers,* 7th IEEE Pulsed Power Conf., edited by R. White and B.H. Bernstein (IEEE, New York, 1989) pp.365-367.

[10] H. Kroemer, "Theory of the Gunn Effect," *Proc. IEEE,* **52**, 1736 (1964).

[11] S.M. Sze, *Physics of Semiconductor Devices*, 2nd ed., (John Wiley and Sons, New York, 1981) p.652.

[12] Ibid, Chapter 11, pp.637-678.

[13] R. Pastore and M. Weiner, "RF Oscillations in Optically Activated Semi-Insulating GaAs" *Digest of Technical Papers,* 7th IEEE Pulsed Power Conf., edited by R. White and B.H. Bernstein (IEEE, New York, 1989) pp.872.

CHAPTER 5

COMPUTER-AIDED ANALYSIS OF PHOTOCONDUCTIVE SWITCHING

In this chapter, we present a model of photoconductive switch behavior that is based on the time-dependent, drift-diffusion equations and carrier continuity equations. The equations were appropriately modified to represent a photoconductor in operation and then solved numerically with boundary conditions and operating parameters that are consistent with high-speed switching of a practical, high-voltage, photoconductive switch in an external circuit. High-field, non-linear effects, such as negative differential resistivity in GaAs and impact ionization, are included in the model. The results of the experiments reviewed in previous chapters are discussed in terms of this computer model.

I. MODEL FORMULATION

On the time scale of ultrafast, high-power photoconductive switch operation, picoseconds to nanoseconds, transient photoconductivity is governed by the generation, recombination, and transport of carriers. Hot electron effects, drift velocity overshoot, and other non-equilibrium processes such as inter-valley transfer of electrons are significant on a subpicosecond, or femtosecond time scale, and need not be included in a model of high-voltage switch operation on a multipicosecond time scale. On this timescale, the carrier mobility, μ, for example, is assumed to have reached its steady-state value so that DC measurements that depend on the drift

velocity versus field relationship, e.g., an I-V curve, are valid. The spatial and temporal variations of the carrier densities, electric field, and potential in the switch on a picosecond time scale are given by the solutions to the coupled system of equations commonly refered to as the drift-diffusion equations, without requiring Monte Carlo type calculations for the electron energy distribution. A study of femtosecond transient photoconductivity utilizing Monte Carlo calculations has been presented by Meyer [1].

Using the drift-diffusion/carrier continuity model, Iverson has previously modeled photoconductors operating in a non-switching, or small-signal, mode where the potential across the switch does not vary appreciably [2,3], and the switching, or large-signal mode, where the bias voltage across the photoconductor is quickly switched to an external load [4]. This photoconductive switching model dealt with large-scale, practical high-power switches, but did not include non-linear carrier mobility. Weiner *et. al.* have also presented a solution to the semiconductor equations in high-bias switches for the constant mobility, or linear, regime [5]. This model did not include carrier diffusion. White *et. al.* [6] have constructed a computer model of high-bias photconductive switching, numerically solving the drift-diffusion/carrier continuity relations, that includes non-linear mobility, but this model deals only with micron-scale device lengths and relatively low bias voltages (< 1 kV) and is not capable of simulating a more realistic, cm-scale device with multikilovolt bias voltage. Sano and Shibata have presented a very complete, three-dimensional model of ultrafast switches in microstrip lines [7], but this model is limited by computer memory requirements to 100 μm size devices and total simulation times of only a few ps; results were only presented for a 2.5 V bias voltage. The model presented here is the first numerical solution of the semiconductor device equations capable of

simulating ultrafast photoconductive switches under operating conditions consistent with realistic pulsed-power applications that includes non-linear carrier mobility.

1. SEMICONDUCTOR DEVICE EQUATIONS

The basic equations needed to describe the behavior of carriers in semiconductors are Maxwell's equations, current density equations, and carrier continuity relations. A comprehensive review has been given by Selberheer [8].

A. Maxwell's Equations

For macroscopic media, Maxwell's equations, describing the dynamical response of materials to electric and magnetic fields, are written in MKS units as:

$$\nabla \times \frac{\mathbf{B}(\mathbf{r},t)}{\mu} = \mathbf{J}(\mathbf{r},t) + \varepsilon \frac{\partial \mathbf{E}(\mathbf{r},t)}{\partial t} \tag{5.1}$$

$$\nabla \times \mathbf{E}(\mathbf{r},t) + \frac{\partial \mathbf{B}(\mathbf{r},t)}{\partial t} = 0 \tag{5.2}$$

$$\nabla \cdot \mathbf{E}(\mathbf{r},t) = \frac{\rho(\mathbf{r},t)}{\varepsilon} \tag{5.3}$$

$$\nabla \cdot \mathrm{B}(\mathbf{r},t) = 0 \,. \tag{5.4}$$

Eq.(5.1) is Ampere's Law with the addition of the displacement current. Eq.(5.2) is Faraday's Law. Coulomb's Law is Eq.(5.3), and Eq.(5.4) states the absence of magnetic monopoles. μ is the magnetic permeability (not to be confused with the carrier mobility). ε is the electric permittivity. μ and ε are, in general, tensors, but for isotropic media they reduce to scalar quantities. Semiconductors currently used in device fabrication do not show significant anisotropy or exhibit significant inhomogeneity effects. μ and ε will be treated as scalars in all further calculations.

With the introduction of the scalar potential, $\Psi(\mathbf{r},t)$, and the vector potential, $\mathbf{A}(\mathbf{r},t)$, we can write the following equations

$$\nabla^2\mathbf{A}(\mathbf{r},t) - \varepsilon\mu\frac{\partial^2\mathbf{A}(\mathbf{r},t)}{\partial t^2} = -\mu\mathbf{J}(\mathbf{r},t) \tag{5.5}$$

and

$$\nabla^2\Psi(\mathbf{r},t) - \varepsilon\mu\frac{\partial^2\Psi(\mathbf{r},t)}{\partial t^2} = -\frac{\rho(\mathbf{r},t)}{\varepsilon} \quad . \tag{5.6}$$

These equations are inhomogeneous wave equations for the vector and scalar potentials and are equivalent to the four Maxwell's equations. The quantity $\varepsilon\mu$ is related to the propagation velocity for a disturbance in the medium, c, by

$$c = \frac{1}{\sqrt{\varepsilon\mu}} \tag{5.7}$$

c can be written in terms of the relative permittivity, $\varepsilon_r = \varepsilon/\varepsilon_o$, and relative permeability, $\mu_r=\mu/\mu_o$, as

$$c = \frac{1}{\sqrt{\varepsilon_r\mu_r}}\, c_o \tag{5.8}$$

where $c_o=\sqrt{1/\mu_o\varepsilon_o}$ is the speed of light in free space. μ_r is very close to unity for most semiconductors, while $\varepsilon_r \sim 10$. The speed of light in semiconductors is $\sim \frac{1}{3}\, c_o$.

Eq.(5.6) is the complete form of Poisson's equation. If the time scale of interest for a particular device's operation is longer than the propagation time, $t = \ell/c$, for an electromagnetic disturbance to travel the length of the device, then the second time derivative term in Eq.(5.6) can be neglected. For the devices we wish to model, we are approaching the limit where this approximation is valid. We have neglected the time derivative in Eq.(5.6) to avoid computational complexity, so Poisson's equation can be written

$$\nabla^2\Psi(\mathbf{r},t) = -\frac{\rho(\mathbf{r},t)}{\varepsilon} \tag{5.9}$$

Eq.(5.9) is the form of Poisson's equation which will be used in device modeling.

B. Current Density Equations

The conduction current, $\mathbf{J}(\mathbf{r},t)$, in a semiconductor device results from the flow of electron-hole pairs and can be written as the sum of an electron component, $\mathbf{J}_n(\mathbf{r},t)$, and a hole component, $\mathbf{J}_p(\mathbf{r},t)$, or

$$\mathbf{J}(\mathbf{r},t) = \mathbf{J}_n(\mathbf{r},t) + \mathbf{J}_p(\mathbf{r},t) \quad . \tag{5.10}$$

Without loss of generality, the current density of charged particles is the product of the particle charge, particle density, and particle drift velocity. So, with $n(\mathbf{r},t)$, $\mathbf{v}_{dn}(\mathbf{r},t)$ and $p(\mathbf{r},t)$, $\mathbf{v}_{dp}(\mathbf{r},t)$ equal to the electron and hole densities and drift velocities, respectively,

$$\mathbf{J}_p(\mathbf{r},t) = e\, p(\mathbf{r},t)\, \mathbf{v}_{dp}(\mathbf{r},t) \tag{5.11}$$

$$\mathbf{J}_n(\mathbf{r},t) = -e\, n(\mathbf{r},t)\, \mathbf{v}_{dn}(\mathbf{r},t) \tag{5.12}$$

The major problem is to find an expression relating the carrier drift velocities to the carrier densities and electric field in the device. The derivation of this relationship will not be given here and the result will be presented without proof. Reviews of this derivation have been presented by Selberheer [7] and Iverson [8] . The results, relating $\mathbf{J}_n(\mathbf{r},t)$ and $\mathbf{J}_p(\mathbf{r},t)$ to the field and density, are

$$\mathbf{J}_n(\mathbf{r},t) = e\mu_n(\mathbf{r},t)\, n(\mathbf{r},t)\, \mathbf{E}(\mathbf{r},t) + e\, D_n(\mathbf{r},t)\, \nabla n(\mathbf{r},t) \tag{5.13}$$

$$\mathbf{J}_p(\mathbf{r},t) = e\mu_h(\mathbf{r},t)\, p(\mathbf{r},t)\, \mathbf{E}(\mathbf{r},t) - e\, D_p(\mathbf{r},t)\, \nabla p(\mathbf{r},t), \tag{5.14}$$

These are the familiar drift-diffusion equations for the conduction current density. The current density consists of a drift term, driven by the electric field, and a

diffusion term, driven by the gradient of the carrier density. $D_n(\mathbf{r},t)$ and $D_p(\mathbf{r},t)$ are the electron and hole diffusion coefficients, given by the Einstein relations as

$$D_n(\mathbf{r},t) = \mu_n(\mathbf{r},t)\,\frac{kT}{e} \tag{5.15}$$

$$D_p(\mathbf{r},t) = \mu_p(\mathbf{r},t)\,\frac{kT}{e}. \tag{5.16}$$

C. Carrier Continuity Relations

The carrier continuity relations, governing the time evolution of the carrier densities, can be derived from Ampere's Law, Eq.(5.1). Taking the divergence of Eq.(5.1),

$$\nabla \cdot [\, \nabla \times \frac{\mathbf{B}(\mathbf{r},t)}{\mu} \,] = \nabla \cdot \mathbf{J}(\mathbf{r},t) + \varepsilon\frac{\partial}{\partial t}[\, \nabla \cdot \mathbf{E}(\mathbf{r},t) \,] = 0 \ . \tag{5.17}$$

Using Eq.(5.3),

$$\nabla \cdot \mathbf{J}(\mathbf{r},t) + \frac{\partial \rho(\mathbf{r},t)}{\partial t} = 0 \ . \tag{5.18}$$

Writing the charge density, $\rho(\mathbf{r},t)$, as the sum of the electron and hole charge densities, assuming for the moment there are no other charges present, yields

$$\rho(\mathbf{r},t) = e[\, p(\mathbf{r},t) - n(\mathbf{r},t)] \tag{5.19}$$

Eq.(5.18) is then written,

$$\frac{\partial}{\partial t}[\, p(\mathbf{r},t) - n(\mathbf{r},t) \,] = -\frac{1}{e}\nabla \cdot [\, \mathbf{J}_n(\mathbf{r},t) - \mathbf{J}_p(\mathbf{r},t) \,] \ . \tag{5.20}$$

This equation is easy to interpret. It relates the sources and sinks of the total conduction current to the time variation of mobile charge. Defining the function $G(\mathbf{r},t)$ as the generation rate describing the creation of electron-hole pairs, and $R(\mathbf{r},t)$ as the reduction rate, describing the loss of electron-hole pairs , Eq.(5.20) can be separated into

$$\frac{\partial n(\mathbf{r},t)}{\partial t} = G(\mathbf{r},t) - R(\mathbf{r},t) + \frac{1}{e}\nabla \cdot \mathbf{J_n}(\mathbf{r},t) \tag{5.21}$$

$$\frac{\partial p(\mathbf{r},t)}{\partial t} = G(\mathbf{r},t) - R(\mathbf{r},t) - \frac{1}{e}\nabla \cdot \mathbf{J_p}(\mathbf{r},t) \quad . \tag{5.22}$$

2. MODEL EQUATIONS

Although we have seen in the images in Chapter 4 showing current channeling that photoconductive switches can display two-dimensional behavior, for simplicity, we have modeled photoconductive switches as one-dimensional devices in terms of current flow and assumed effects perpendicular to the applied bias field are of second order and may be neglected. It is, then, only necessary to pose the problem in one spatial variable and in one spatial direction along the applied bias field. Call this variable x, $x \in (0,\ell)$, where ℓ is the switch electrode gap. Also, as the photogenerated, or excess densities, are typically many orders of magnitude greater than the thermal equilibrium densities, the carrier densities in the previous equations can be considered to be the excess densities, with the small thermal equilibrium values of the electron and hole densities neglected. Fig.5.1 shows the photoconductive switch and circuit, illumination schemes, and variables used in this model. The one-dimensional forms of the semiconductor device equations are given in Table 5.1.

Eqs.(5.23-30) are a system of nonlinearly coupled, parabolic /elliptic partial differential equations. This system is solved for the particular functions, R(x,t) and G(x,t), and initial values and boundary conditions appropriate for photoconductive switch operation.

Diffusion of carriers can be included in the model even though the applied bias voltage is vastly greater than the thermal voltage, $\frac{kT}{e}$, which is $\cong$.03 V at room temperature. It would appear that the drift component of the current would

Table 5.1

One-Dimensional Drift-Diffusion Model Equations

$$\frac{\partial n(x,t)}{\partial t} = G(x,t) - R_n(x,t) + \frac{1}{e}\frac{\partial}{\partial x}J_n(x,t) \tag{5.23}$$

$$\frac{\partial p(x,t)}{\partial t} = G(x,t) - R_p(x,t) - \frac{1}{e}\frac{\partial}{\partial x}J_p(x,t) \tag{5.24}$$

$$J_n(x,t) = e\mu_n(x,t)n(x,t)E(x,t) + e\, D_n(x,t)\frac{\partial}{\partial x}n(x,t) \tag{5.25}$$

$$J_p(x,t) = e\mu_h(x,t)p(x,t)E(x,t) - e\, D_p(x,t)\frac{\partial}{\partial x}p(x,t) \tag{5.26}$$

$$\frac{\partial^2}{\partial x^2}\Psi(x,t) = -\frac{e}{\varepsilon}[\, p(x,t) - n(x,t)] \tag{5.27}$$

$$E(x,t) = -\frac{\partial}{\partial x}\Psi(x,t) \tag{5.28}$$

$$D_n(x,t) = \mu_n(x,t)\frac{kT}{e} \tag{5.29}$$

$$D_p(x,t) = \mu_p(x,t)\frac{kT}{e} \tag{5.30}$$

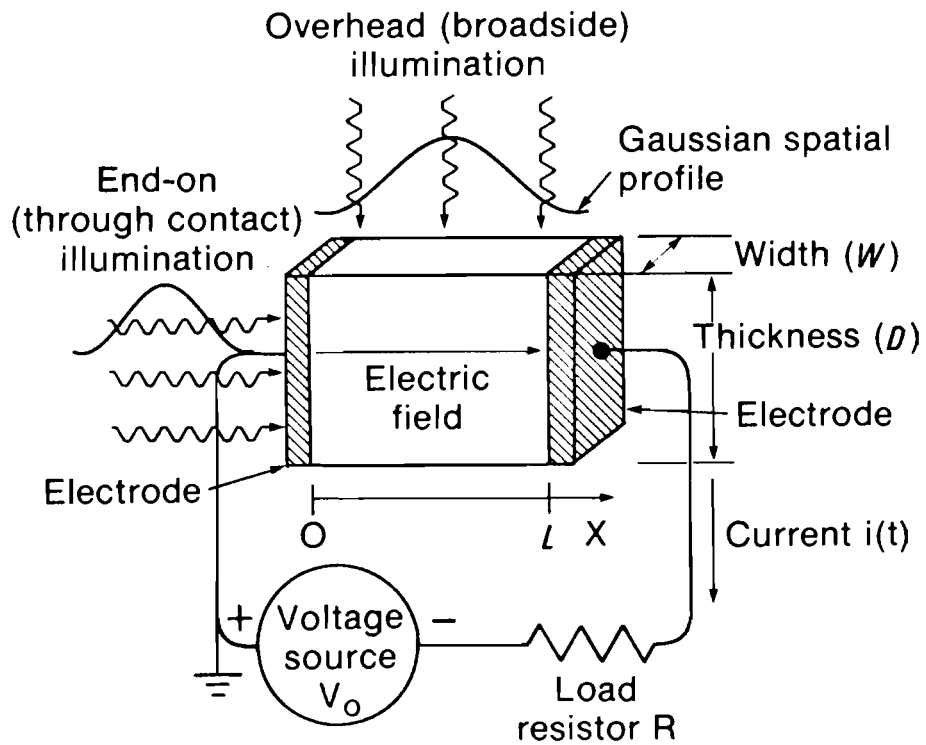

Fig.5.1 Photoconductive switch and external circuit as modeled in computer simulation. Model variables, parameters, and illumination schemes shown.

dwarf the diffusion term. However, as the electric field collapses to a very low value when the switch closes, the diffusion current may become comparable to the drift current. Also, diffusion can be significant if very large carrier density gradients develop. The inclusion of diffusion also completes the model mathematically. We can choose to run simulations without diffusion, as well.

A. Carrier Generation Functions

The function G(x,t) represents the generation of carriers. G(x,t) can be written as the sum of two parts

$$G(x,t) = G_{opt}(x,t) + G_{imp}(x,t) \tag{5.31}$$

$G_{opt}(x,t)$ is the electron-hole pair generation rate due to photoexcitation by laser light and $G_{imp}(x,t)$ is the generation rate due to the excitation of electron-hole pairs through impact ionization.

The form of $G_{opt}(x,t)$ depended on the particular illumination scheme that was simulated. In all cases, the number of carriers created was assumed proportional to the optical energy absorbed and the optical pulse was assumed to have a normalized Gaussian temporal profile. In general, $G_{opt}(x,t)$ can be written

$$G_{opt}(x,t) = \phi(x) \frac{N_o}{a\sqrt{2\pi}} e^{-\frac{(t-t_o)^2}{2a^2}} \tag{5.32}$$

where N_o is the total number of photons in the optical pulse, a is the temporal variance of the optical pulse ($a = \frac{FWHM}{2\sqrt{\ln(4)}}$), and $\phi(x)$ will depend on the particular spatial illumination scheme. Overhead, or broadside, illumination, and end-on, through the contact, illumination were simulated. For end-on illumination, t in Eq.(5.32) is replaced by $t \rightarrow t - x/c$ to represent a Gaussian pulse propagating through

the switch from x= 0, or $t \rightarrow t - (\ell - x)/c$ for a light pulse propagating from $x = \ell$. The amount t_o is subtracted from t to shift the peak optical intensity away from t = 0 so that illumination begins t_o before the peak of the optical pulse (typically at ~1% of the peak intensity). For uniform overhead illumination, $\phi(x)$ is given by

$$\phi(x) = \frac{1}{\ell wd} \tag{5.33}$$

where A = wd is the area of the conducting region of the switch, and ℓA is equal to the conducting volume. For a normalized Gaussian spatial laser beam profile,

$$\phi(x) = \frac{1}{b\sqrt{2\pi}} \frac{1}{A} e^{-\frac{(x-ctr)^2}{2b^2}} \tag{5.34}$$

where b is the spatial variance of the optical beam, and ctr is the center of the illumination. Asymmetric illumination can be simulated by giving ctr a value other than $\ell/2$. For end-on illumination through x=0, $\phi(x)$ is written

$$\phi(x) = \frac{\sigma}{wd} e^{-\sigma x} \tag{5.35}$$

where σ is the absorption coefficient of the semiconductor for the optical pulse. For illumination through $x = \ell$, x in Eq.(5.36) is replaced by $x \rightarrow \ell - x$.

Intrinsic impact ionization occurs when a carrier gains enough energy through acceleration in an electric field to directly generate an electron-hole pair through collision. The electron-hole generation rate due to impact ionization is given by

$$G_{imp}(x,t) = \alpha_n n(x,t) v_{dn}(x,t) + \alpha_p p(x,t) v_{dp}(x,t) \tag{5.36}$$

where α is defined as the number of electron-hole pairs generated by a carrier per unit distance traveled. α_n and α_p are strongly dependent on the electric field. The forms of α used in this model were obtained by fitting expressions given by Sze to

Table 5.2

Model Impact Ionization Parameters

GaAs

Electrons $\alpha_n(E) = 0.173\ V^{-1}\ E\ e^{\frac{-3.64 \times 10^{11}\ V^2/cm^2}{E^2}}$

Holes $\alpha_p = \alpha_n$

Silicon

Electrons $\alpha_n(E) = 1.1016\ V^{-1}\ E\ e^{\frac{-9.242 \times 10^5\ V/cm}{E}}$

Holes $\alpha_p(E) = 3.420\ V^{-1}\ E\ e^{\frac{-1.766 \times 10^6\ V/cm}{E}}$

E is the electric field in V/cm

(after ref.[10])

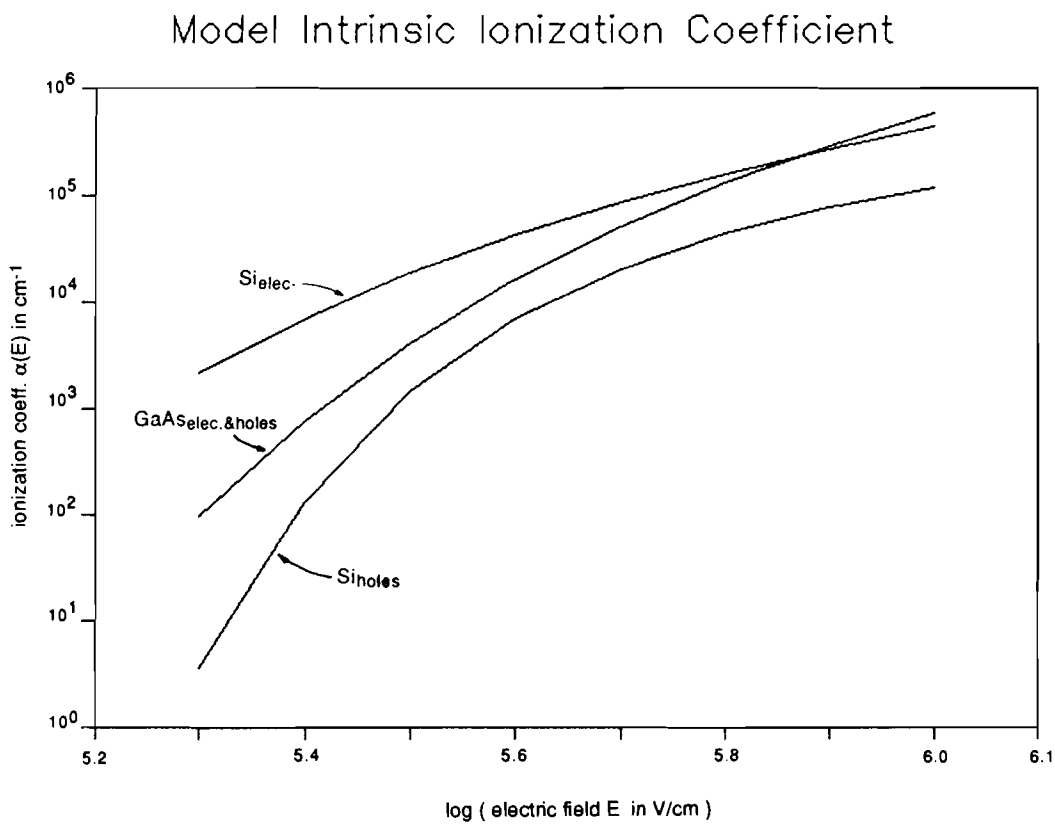

Fig.5.2 Plot of the impact ionization coefficient functions for Si and GaAs used in the switch simulation model.

experimental data also presented in Sze [10]. The model expressions for α are given in Table 5.2 and are plotted in Fig.5.3.

B. Reduction Function

The function R(x,t) represents the reduction of carriers through recombination processes. Only direct recombination of electrons with holes is considered, leading to the simple expressions for the hole and electron recombination rates

$$R_n(x,t) = R_p(x,t) = \frac{\text{minimum of } \{ p(x,t) ; n(x,t) \}}{\tau} \qquad (5.37)$$

where τ is the carrier recombination time. The minority carrier density determines the recombination rate as more electrons, for example, cannot recombine than there are holes with which to recombine. It was chosen to write R(x,t) as Eq.(5.37) as this form is symmetric and does not create charge. It is possible to use more complex forms for R(x,t), such as trap-assisted Schockley-Read-Hall recombination, which would provide more fitting parameters, but Eq.(5.37) proved adequate for our simulations.

C. Carrier Mobility

The electric field dependence of the carrier mobility is included in the model. It is necessary to include this non-linear effect to properly simulate photconductive switching at high-bias fields. The field-mobility relation for GaAs used by Horio *et. al.* [11] was used. For Si, the relationship given by Sze was used [12]. The mobility functions are given in Table 5.3. The drift velocities implied by the model mobility functions are plotted in Fig.5.32.

3. BOUNDARY AND INITIAL VALUES

Table 5.3

Model Mobility Functions

	Equations	Parameters
GaAs		
Electrons	$\mu_n = \mu_{no}\dfrac{1 + (v_{ns}/\mu_{no})(E/E_o)^4}{1 + (E/E_o)^4}$	$\mu_{no} = 8000\ cm^2/Vs$ $V_{ns} = 8.5 \times 10^6\ cm/s$ $E_o = 4000\ V/cm$
Holes	$\mu_p = \mu_{po}\dfrac{1}{1 + \mu_{po}E/v_{ps}}$	$\mu_{po} = 400\ cm^2/Vs$ $V_{ps} = 1 \times 10^7\ cm/s$
Silicon		
Electrons	$\mu_n = \mu_{no}\dfrac{1}{1 + \mu_{no}E/v_{ns}}$	$\mu_{no} = 1500\ cm^2/Vs$ $V_{ns} = 1 \times 10^7\ cm/s$
Holes	$\mu_p = \mu_{po}\dfrac{1}{1 + \mu_{po}E/v_{ps}}$	$\mu_{po} = 450\ cm^2/Vs$ $V_{ps} = 1 \times 10^7\ cm/s$

(after refs.[11]&[12])

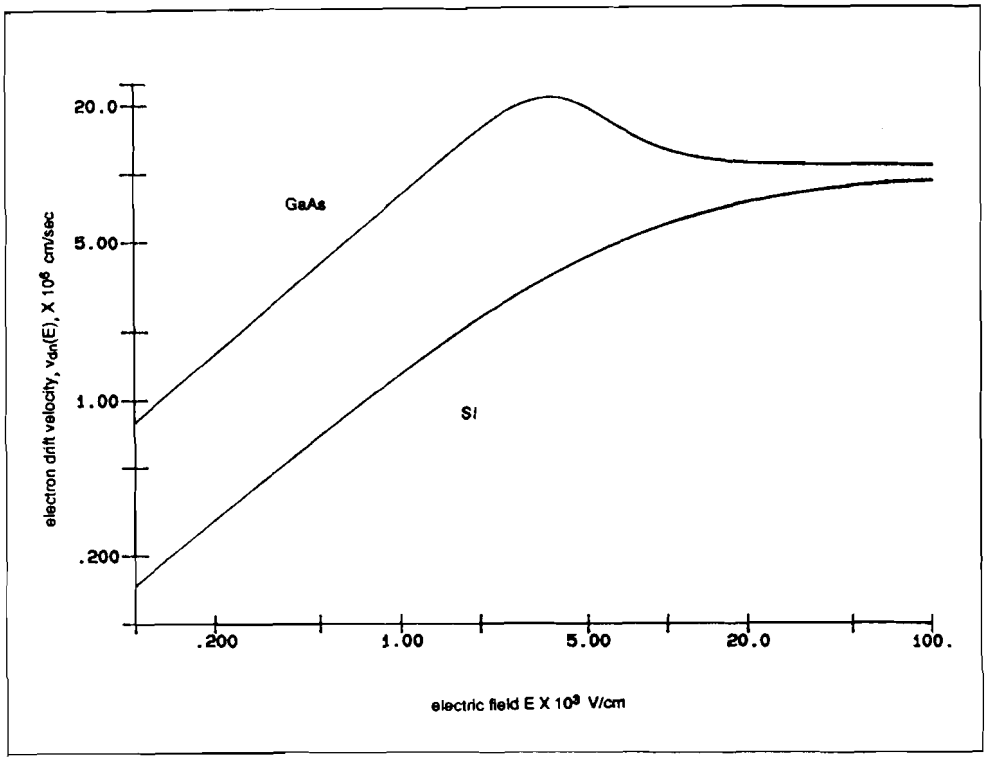

Fig.5.3 Plot of electron drift velocity for GaAs and Si versus electric field using the mobility expressions from the simulation model.

A. Carrier Densities

The switch electrodes are located at $x = 0$ and $x = \ell$. The contact at $x = 0$ is connected to ground. The negative high-voltage bias is applied at $x=\ell$. The contacts are assumed to be perfectly ohmic, with infinite surface recombination velocity. The carrier densities at ohmic contacts will be the thermal equilibrium values; the excess densities will be zero [13]. The switch is assumed to be in thermal equilibrium before illumination at $t = 0$, so the excess densities are zero at $t = 0$. These conditions can be summarized

$$n(0,t) = n(\ell,t) \equiv 0 \tag{5.38}$$

$$p(0,t) = p(\ell,t) \equiv 0 \tag{5.39}$$

$$n(x,0) = p(x,0) \equiv 0. \tag{5.40}$$

B. Electric Potential

The electric field is assumed to be continuous across the contact boundary, as is the current density. For special simulations of non-ohmic contacts, the current density at the contact is set equal to zero.

The electric potential boundary conditions are somewhat more complicated. A derivation of boundary conditions on the electric potential, $\Psi(x,t)$, is now presented which accurately represents the operation of a high-speed photoconductive switch. This derivation follows closely that given by Iverson [4].

The left-hand contact, at $x = 0$, is grounded, so the applied bias voltage, V_o, is felt at the right-hand contact, $x = \ell$, at $t = 0$.

$$\Psi(0,t) = 0. \tag{5.41}$$

$$\Psi(\ell,0) = V_o. \tag{5.42}$$

The potential at the right-hand contact will vary as the switch is driven conductive by the optical pulse and the bias voltage is switched to the load. To derive a boundary condition for the potential at $x = \ell$ for $t > 0$ requires a relationship for the total current density.

The total switch current density, $J_T(t)$, is that which is delivered to the external circuit and must obey the conservation law, $\nabla \cdot J_T(t) = 0$, or in one dimension

$$\frac{\partial}{\partial x} J_T(t) = 0, \tag{5.43}$$

so that $J_T(t)$ is a spatial invariant. By taking the time derivative of Eq.(5.27) and substituting Eq.(5.23) and Eq.(5.24) into the right-hand side, the resulting expression is

$$\frac{\partial}{\partial x}\{J_n(x,t) + J_p(x,t) + \varepsilon \frac{\partial E(x,t)}{\partial t}\} = 0. \tag{5.44}$$

Comparing Eqs.(5.43) and (5.44) leads to the definition of the total current density as

$$J_T(t) = J_n(x,t) + J_p(x,t) + J_D(x,t) \tag{5.45}$$

where

$$J_D(x,t) = \varepsilon \frac{\partial E(x,t)}{\partial t} \tag{5.46}$$

is the electromagnetic displacement current density. Because of the spatial invariance of the total current density,

$$\frac{1}{\ell} \int_0^{\ell} J_T(t) \partial x = J_T(t). \tag{5.47}$$

Substituting Eq.(5.45) into Eq.(5.47) and making use of Eqs.(5.25-26), and Eq.(5.28) yields

$$J_T(t) = \frac{1}{\ell}\{e\int_0^{\ell} E(x,t)[\mu_n(x,t)n(x,t)+\mu_p(x,t)p(x,t)]\partial x$$

$$+e[D_n(x,t)n(x,t)\Big|_0^{\ell} - D_p(x,t)p(x,t)\Big|_0^{\ell}] - \varepsilon\frac{\partial}{\partial t}[\Psi(\ell,t)-\Psi(0,t)]\}. \qquad (5.48)$$

Applying the boundary conditions given in Eqs.(5.38-39) and Eq.(5.41) to Eq.(5.47) gives

$$J_T(t) = \frac{1}{\ell}\{e\int_0^{\ell} E(x,t)[\mu_n(x,t)n(x,t)+\mu_p(x,t)p(x,t)]\partial x - \varepsilon\frac{\partial}{\partial t}[\Psi(\ell,t)\}. \qquad (5.49)$$

The circuit current i (t) is

$$i\,(t) = J_T(t)\,A.$$

The circuit equations give the potential at $x = \ell$, $\Psi(\ell,t)$, as

$$\Psi(\ell,t) = J_T(t)\,AR + V_o, \qquad (5.50)$$

where R is the load resistance.

Substituting Eq.(5.49) into Eq.(5.50) gives a differential equation for $\Psi(\ell,t)$ as

$$\frac{\partial}{\partial t}\Psi(\ell,t) = \frac{e}{\varepsilon}\{\int_0^{\ell} E(x,t)[\mu_n(x,t)n(x,t)+\mu_p(x,t)p(x,t)]\partial x\ \}$$

$$-\frac{\ell}{\varepsilon AR}[\Psi(x,t) - V_o]\ . \qquad (5.51)$$

Eq.(5.51) gives a mixed, global boundary condition for $\Psi(\ell,t)$ which must be integrated with the system given in Table 5.1. This boundary condition correctly accounts for the displacement current and is, thus, valid for high-speed switching simulation.

II. NUMERICAL SOLUTION METHOD

The practical units of high-power switching are picoseconds, centimeters, and volts. It was chosen to dimensionalize all equations in these units. All independent variables and constants of Table 5.1 and Eq.(5.51) were normalized to picoseconds, centimeters,and volts.

The redimensionalized model equations were then solved numerically. The equations were first put into a discrete form using a finite difference representation. Centered difference representations [14] are used for the density gradients in Eqs.(5.25-26), second derivative of the potential in Eq.(5.27), and potential gradient in Eq.(5.28). The divergence of the current density in the continuity equations is represented using an upwind-differencing scheme [15]. The spatial discretization is carried out on a uniform mesh, dividing the domain $(0,\ell)$ into equally spaced mesh points. Both 500 point and 250 point meshes were used. A fully explicit, forward time finite difference scheme is used for the time derivatives in the continuity equations.

A computer program, written in FORTRAN, was used to solve the system of finite difference equations. First, at the start of each time step, the carrier generation function for that time step is calculated. Then, using the density values calculated in the last time step or from the initial conditions, the electric potential at each mesh point is determined. This is done by using the Thomas algorithm [16] to solve the tri-diagonal system of simultaneous algebraic equations resulting from the discretization of Poisson's equation The electric field is then determined from the potential, and the carrier mobilities from the field-mobility relations. Next, the current densities are evaluated at each mesh point. The carrier continuity equations are integrated forward in time determining the new carrier densities, which will be used in the next time step.

The differential equation for the potential at the right-hand endpoint is also integrated forward in time, yielding a new value to be used in calculations in the next time step. The integral required by the boundary condition equation was evaluated using a Simpson's rule quadrature scheme. All variables are renewed and the process is iterated until the desired device operation time has been simulated.

The fully explicit time integration scheme, while requiring relatively little storage, places a severe restriction on the discrete timestep that may be used. Stability was achieved using time and space steps, Δt and Δx, that satisfy the Courant stability criterion, $\Delta x < v\Delta t$, where v is the speed of the fastest phenomenon in the modelled system [17]. v was taken to be the speed of light in the semiconductor. Timesteps four times smaller than those demanded by the Courant condition were typically used to obtain accurate results. Program accuracy was determined by comparing numerical results for simple test cases with the analytical solutions.

III. COMPUTATIONAL RESULTS

Simulations were run for operating parameters consistent with the experiments that were carried out. The illumination schemes, optical pulse intensities, device dimensions, bias voltages, and boundary conditions were set to recreate the actual conditions as closely as possible. A Digital Equipment VAX and a CYBER 990 computer were used to run the simulations. In the course of the computations it was found that carrier diffusion did not play a significant role in photoconductive switch operation and could actually lead to instabilities in the numerical results. This is due to an instability inherent in equations containing both convection and diffusion terms. There is a special numerical technique for dealing with this instability, namely the upwind differencing scheme of Scharfetter and Gummel [18], although this finite-

difference formulation obscures the physics of the problem. We eliminated carrier diffusion from our model after establishing its relative unimportance.

1. GALLIUM ARSENIDE SWITCHING

A. Coplanar Switches

The operation of the coplanar GaAs switches discussed in Chapter 4 was simulated. For these switches, ℓ = .25 cm, w = .25 cm, and d = .05 cm. A value of ε = 13.1 was used for the the permittivity of GaAs [19]. The simulation carrier lifetime was 600 ps. The optical pulse FWHM was 140 ps. Overhead illumination by Gaussian spatial profile optical beams was modeled, using model parameters matching experimental conditions. The spatial profile of the optical beam had ~10% energy imbalance between the ends of the switch and the switch center. The optical pulse energy was 50 μJ and the pump wavelength was 532 nm, resulting in carrier densities of ~10^{16}/cm^3. The negative high voltage is applied at x = .25 cm. The electric field is positive if it is in the positive direction of x: the bias field is positive.

Computed values of the electric field spatial profile are shown in Figs.5.4, 5.5, and 5.6. Calculated profiles are shown for bias voltages of -1 kV, -3 kV, and -6 kV. The corresponding experimentally obtained profiles for -2.5 kV and -6 kV from Chapter 4 are also shown. The simulated and observed profiles are in excellent qualitative agreement. The -1 kV bias voltage field profile, corresponding to a bias field of 4 kV/cm, displays linear behavior: the initial bias field collapses in time effectively to zero and then recovers as the carrier density decreases due to recombination. The slight , symmetrical increase in field at the contacts is the result of the Gaussian spatial profile of the pump beam. As the bias voltage in the

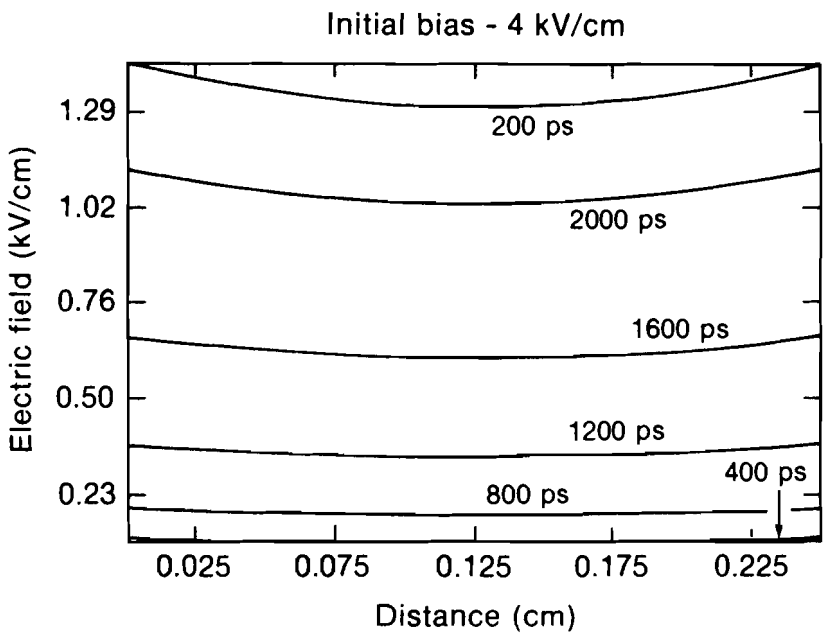

Fig.5.4 Calculated spatial profile of electric field in GaAs switch biased at -1 kV at different times during switch operation. The electric field displays uniform collapse and recovery at this bias voltage.

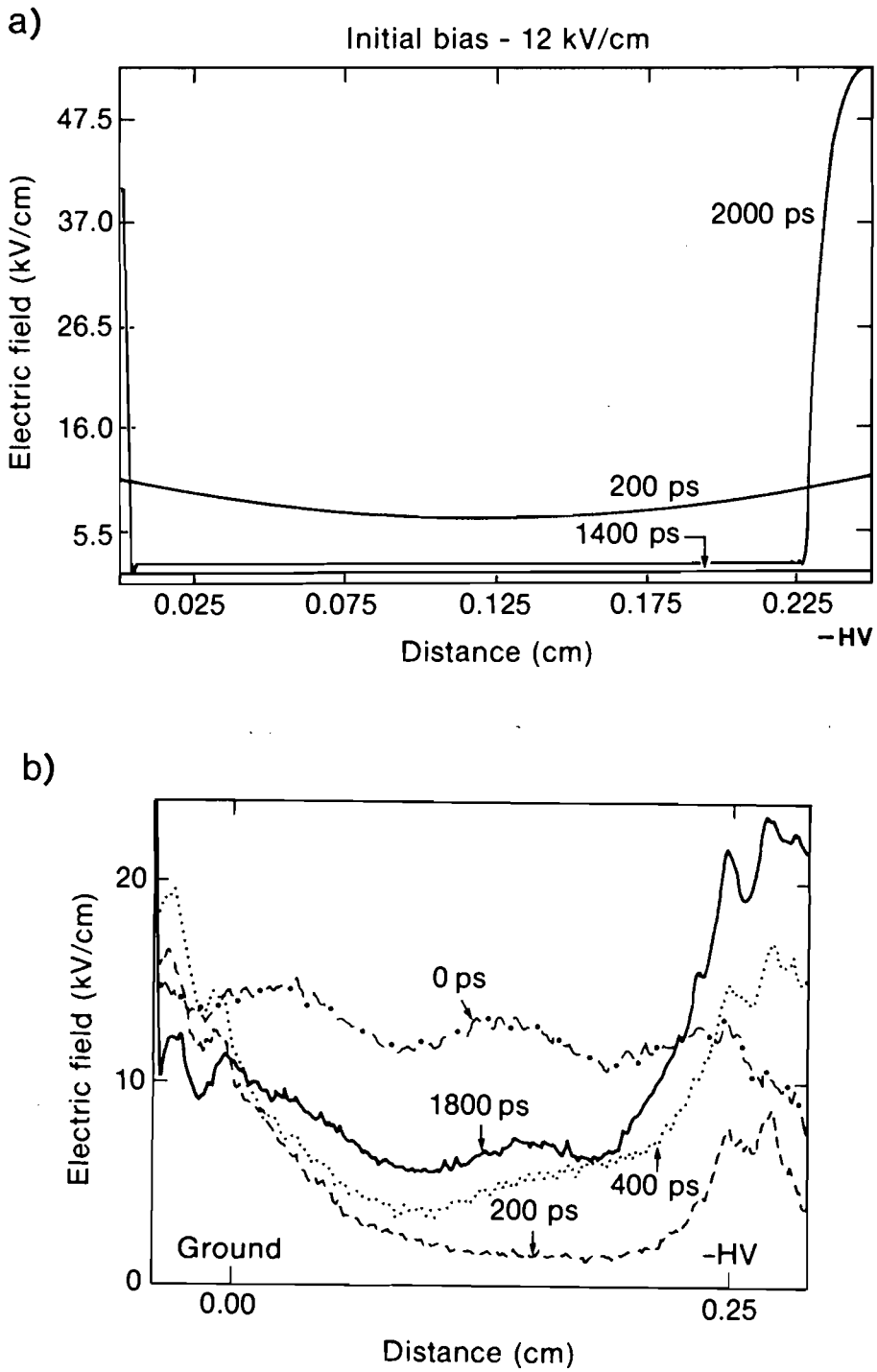

Fig.5.5 Electric field spatial profiles for GaAs switch: (a) calculated profile for -3 kV bias; (b) profile obtained with e-o imaging system for -2.5 kV bias.

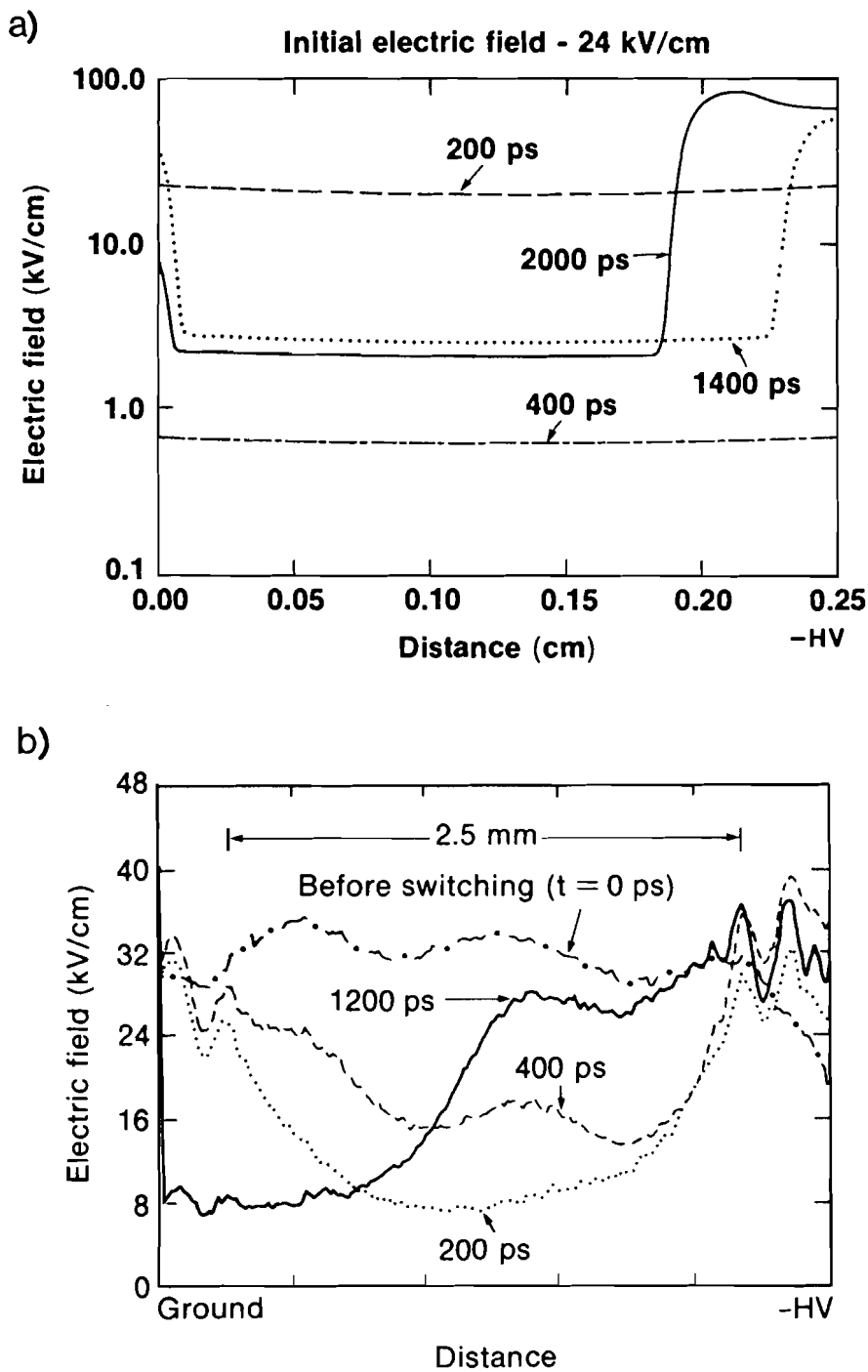

Fig.5.6 GaAs switch electric field spatial profiles for -6 kV bias: (a) calculated profile ; (b) measured profile. Note the high field region near the cathode in both (a) and (b).

simulation is increased to -3kV, the field becomes strongly enhanced at the contacts, with a field spike beginning to form at the cathode as the carrier density decreases due to recombination. This field enhancement is displayed in the e-o image lineout, as well. As the voltage is increased, this field enhancement at the cathode becomes the salient feature of the field profiles. At -6 kV bias, the simulated field at the cathode is higher than the initial bias field of 24 kV/cm. This high field domain can be seen to be moving toward the ground contact. The domain velocity is ~1 x 10^7 cm/s. Simulations for longer times show a second domain will nucleate the cathode. The formation of a high-field domain at the cathode is also observed in the experimental profile, although the field enhancement is not the same magnitude as in the simulations. Fig.5.7 shows the simulated electric field profile for -6 kV bias on an expanded time scale, emphasizing the initial optically-induced collapse of the field. The simulated profile shows the same rapid collapse in the switch center, not directly related to the pump spatial profile, as is observed in the experimental lineouts in Figs.5.5(b) and 5.6(b) for t < 400 ps.

The calculated switch output waveform for -6 kV bias is shown in Fig.5.8. The average electron density in the switch is also shown. Lock-on effects, such as persistent output current, are not recreated in simulated GaAs output waveforms. On the basis of this model's results, intrinsic impact ionization is not responsible for lock-on. Some other carrier gain mechanism, whose effects are appreciable at lower fields, may be appropriate. Impact ionization of traps is a possibility.

The corresponding electron density profile for the simulated -6 kV bias profile in Fig.5.6 is shown in Fig.5.9. There is a propagating density disturbance which corresponds to the high-field domains in the electric field profile. Figs.5.6 & 5.9 are consistent with previous calculations [20] and experiments [21] for GaAs Gunn

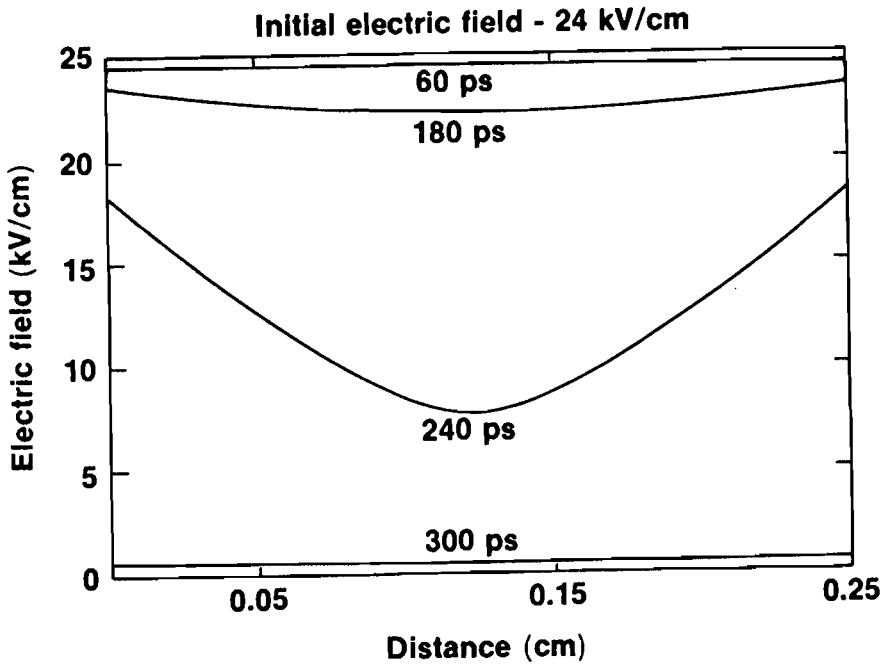

Fig.5.7 Calculated Electric field profile at -6 kV bias as in Fig.5.6(a) with emphasis on early collapse of field. Note the field collapses most rapidly in the switch center.

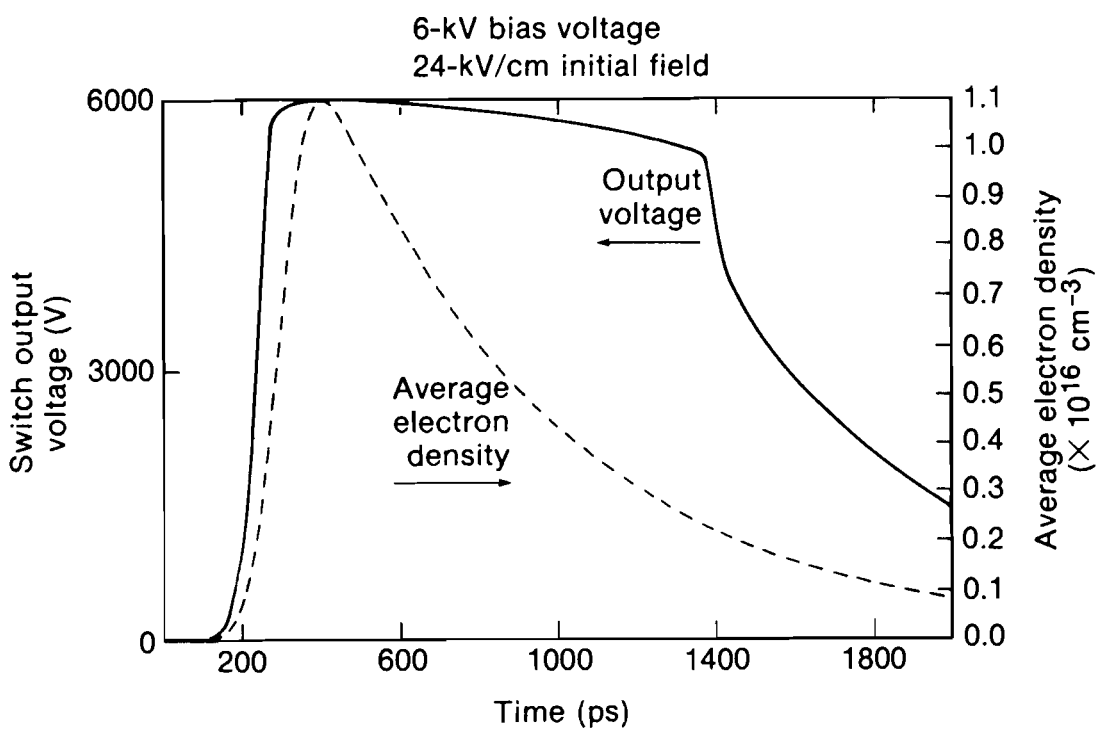

Fig.5.8 Simulated GaAs switch output waveform at -6 kV bias. The average electron density in the switch is also shown.

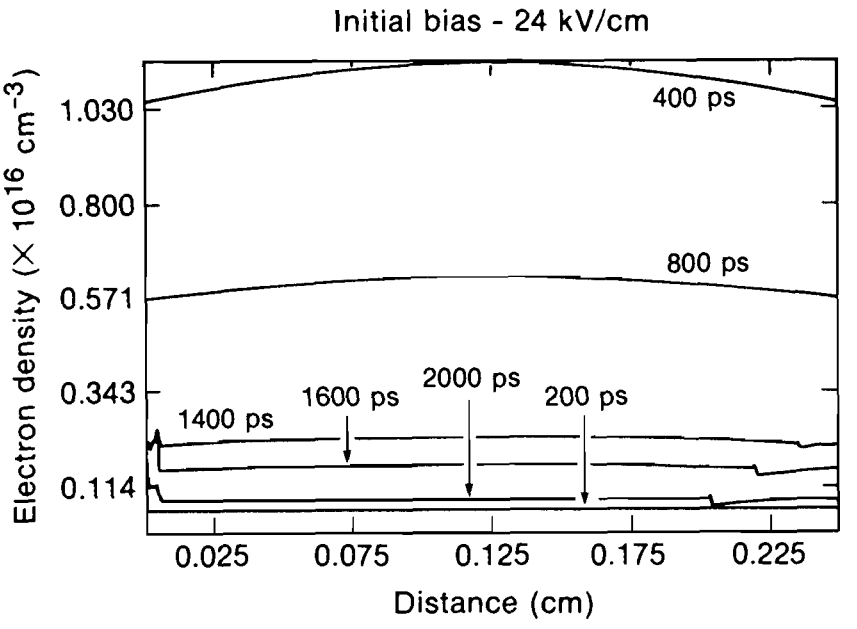

Fig.5.9 Calculated electron density spatial profile in GaAs switch at different times during switch operation, bias - 6 kV. Note the propagating density disturbance for times ≥ 1400 ps moving from the cathode on the right.

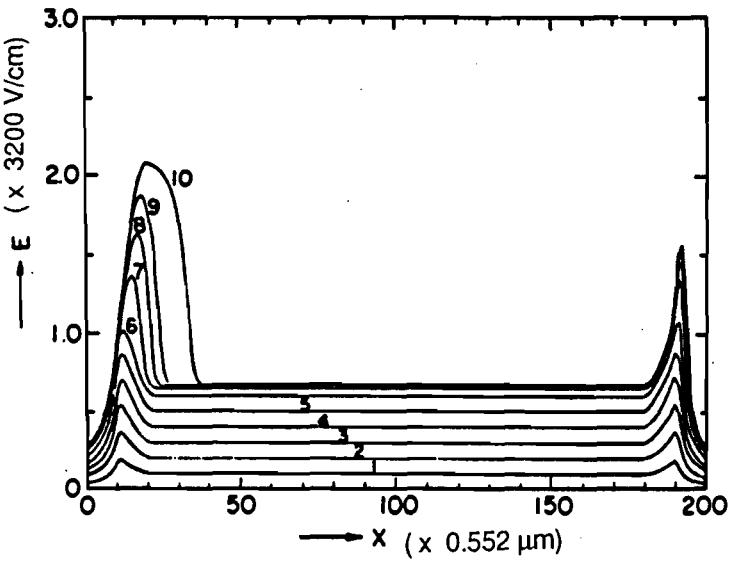

Fig.5.10 Calculated electric field profile at various times during operation of a GaAs Gunn diode as reported by Ohtomo. Time increases with each successive lineout, numbered from 1 to 10. Note the high-field domain forming at the cathode at the left. (after ref.[20])

diodes . Electric field profiles in a Gunn diode calculated by Ohtomo [20] are shown in Fig.5.10. The similarity to Fig.5.6 is striking: simulation indicates that a GaAs photoconductive switch displays behavior similar to a Gunn diode during the field recovery period at sufficiently high bias.

To determine the cause of the high-field domains, numerous simulations were run, including various non-physical situations, such as constant mobility, extremely long carrier lifetimes, etc. Only those simulations including nonlinear carrier mobility exhibited high-field formation. The formation of domains in the calculated data was influenced by the illumination profile parameters and the simulation recombination time, and occured only during the recovery of the switch. Gunn domains are not observed in the modeling of switching in Si for any combination of parameters. The formation of high-field domains is a result of negative differential resistance in GaAs.

B. Bulk Switches

The switching of the bulk GaAs switches with gridded electrodes was simulated. For these switches, illumination through the electrode grid was modelled by a propagating Gaussian optical pulse. The program parameters were : ℓ = .6 cm; the conducting area , A = .1 cm; ε_r = 13.1; and the absorption coefficient,σ = 1.39 cm. These parameters were chosen to represent the actual switches that were used in experiments. The value of A was the measured optical beam size. σ was measured at LLE for the samples provided. The applied optical pulse energy was 100 μJ resulting in carrier densities of ~10^{16} /cm^3. The optical pulse variance was 200 ps.

A spatial profile of the electric field for an applied bias voltage of -9 kV is shown in Fig.5.11(a) for illumination through the ground contact only. The electric field collapses in time from the ground contact to the negative high-voltage contact as the optical pulse propagates through the switch. The field is seen to "compress" as it

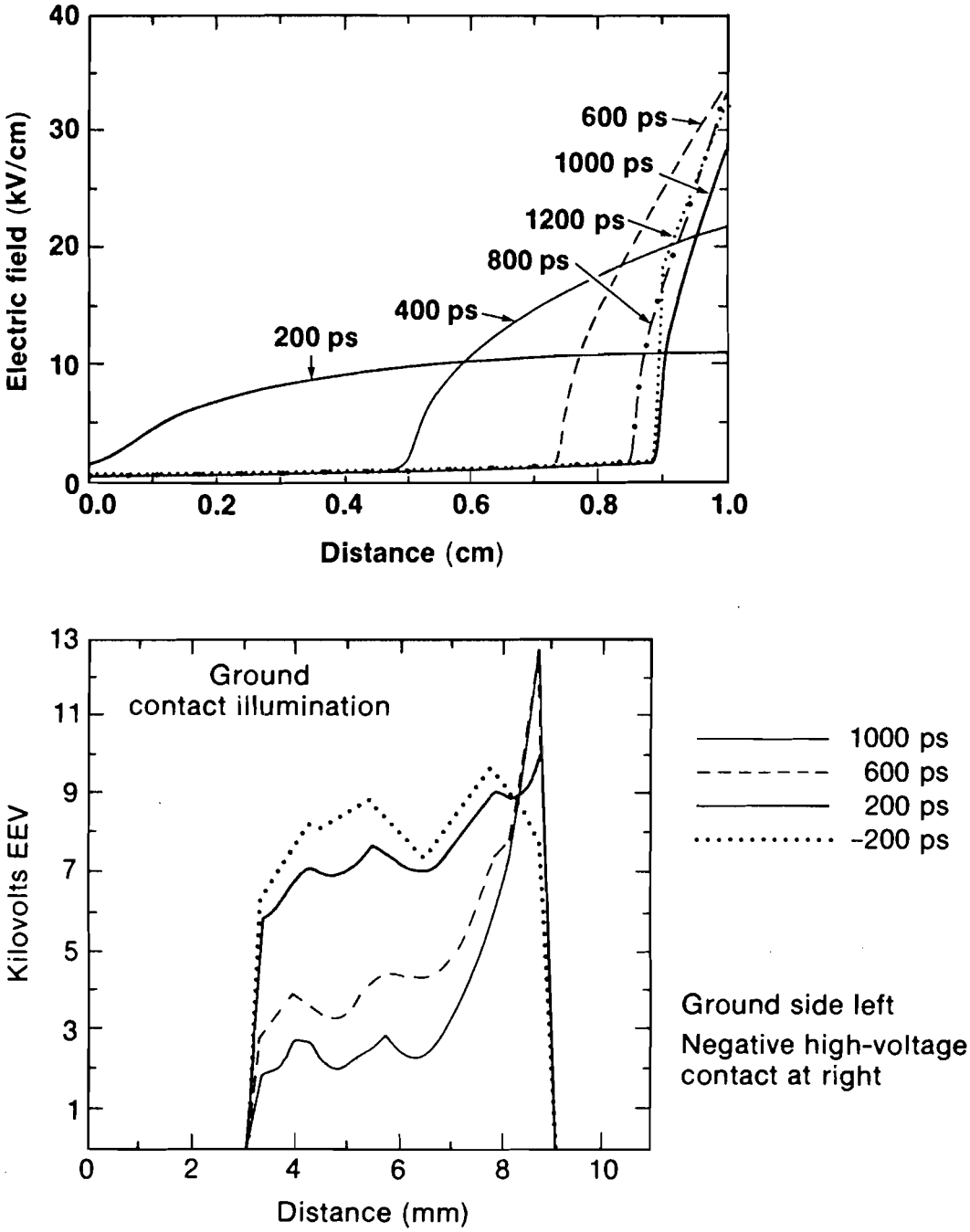

Fig.5.11 Electric field profiles during bulk switch operation with illumination through the ground contact at x=0: (a) simulation profiles; (b) experimental profiles. In each case, the field can be seen to collapse from the ground side, forming a peak at the opposite contact.

collapses, forming a field peak at the contact opposite illumination. The field is compressed until, at 1200 ps, NDR effects take over. This sharpens the field gradient and rise in the field at the contact. Excellent qualitative agreement is obtained with the electric field profiles obtained experimentally for this illumination scheme, which is shown in Fig.5.11(b).

Simultaneous illumination through both the ground and negative high-voltage electrode was also simulated. The calculated electric field profiles showed surprisingly uniform collapse. The simulated switching with two-side illumination was considerably more efficient than one-side illumination, with more complete field collapse and faster rise time, in agreement with experiment. The observed field peaking at the contacts (~1.2 times the bias field) is not reproduced in the two-side illumination modelling for ohmic contacts.

As mentioned in Chapter 4, it was observed that the gridded contacts on the switch were physically deteriorating as the experiments progressed. There was arcing from the metal segments of the mesh contacts to the bare GaAs in the mesh holes. The contacts become less and less uniform and less ohmic. To simulate this, the boundary conditions on the current density were altered to represent contacts that would not pass current. Two-side illuminated switches with non-injecting contacts were simulated. The calculated electric field profiles for this case showed the same uniform field collapse as the ohmic case except for an extreme field peak at the negative high-voltage electrode. This peak is ~20 times the applied bias field. As the electrode is gridded, there will be some areas of the electrodes that are metallized and pass current and open areas that do not. The simulations suggest that there will be a significant potential difference between the injecting and non-injecting regions. This explains the observed arcing between the non-metallized and metallized areas. Some

average between the non-injecting and injecting simulations would explain the observed profiles for the two-side illumination case.

The observed decrease in the electro-optic switch efficiency is not recreated in the simulations. Simulations do not show significant field remaining across the switch after several nanoseconds. It is not possible to conclude, on the basis of this computer model, that the observed decrease in electro-optic switch efficiency is due to negative differential resistance in the photoconductive switch.

The failure of the program to recreate exactly the observed field profiles is most probably due to the fact that the gridded electrode switches do not lend themselves completely to a one-dimensional analysis. To properly simulate the bulk switches with gridded electrodes, it would be necessary to model the conducting and non-conducting channels created by the electrode grid. There is probably considerable vertical structure that affects the field profile, as well. Simulation of these effects would require a much more advanced, three-dimensional model. Also, the field probe can only access the switch field at the switch surface and the surface field may not be a true measure of the internal field structure for switches with such considerable vertical structure.

2. SILICON SWITCHING

Silicon switch operation was also modeled. Si switches with the same physical dimensions as the planar GaAs switches, ℓ = .25 cm, w = .25 cm, and d = .05 cm, were simulated with overhead illumination by Gaussian spatial profile laser pulses. Fig.5.12 shows calculated electric fields for -20 kV bias (80 kV/cm) and 150 ps FWHM, 1064 nm laser pulse with pulse energy of 100 μJ. τ was taken to be 73 μs, a representative measured value, and ε_r was 11.9 [19]. The field collapse is quite

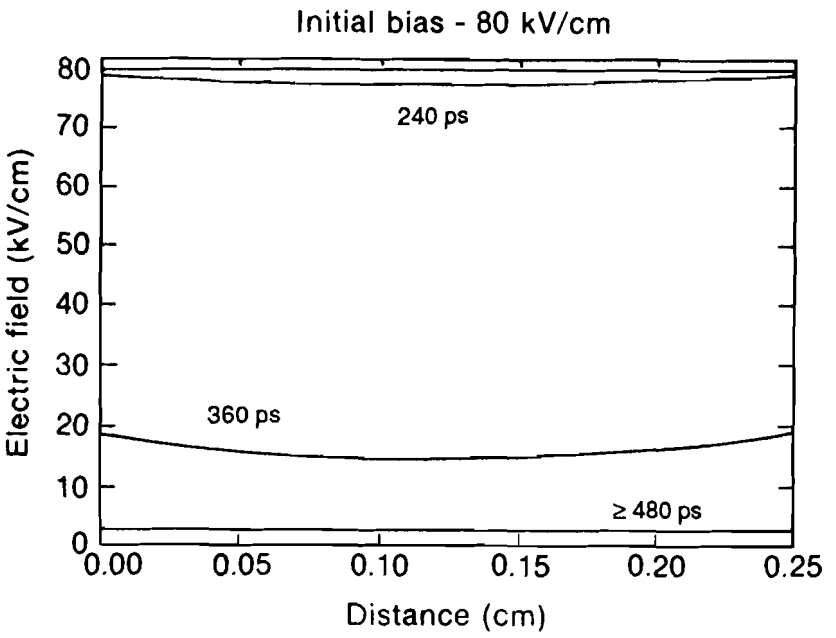

Fig.5.12 Calculated electric field profiles for Si switch at bias of -20 kV. The field collapse is uniform. Switch recovery is not seen due to long recombination time of Si.

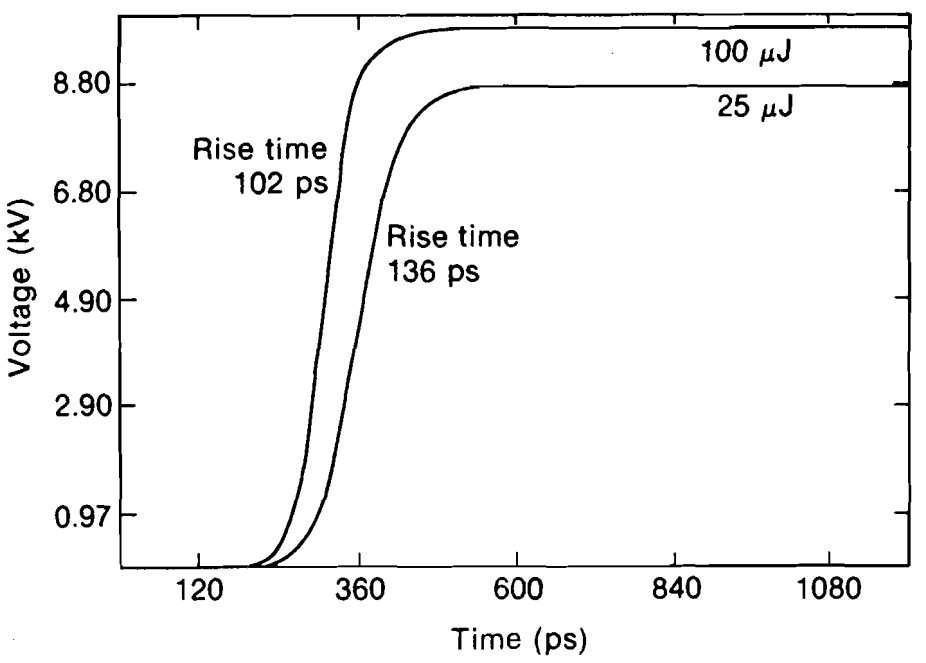

Fig.5.13 Calculated Si switch output waveform at -10 kV bias. Note the decrease in switch efficiency and increase in switch risetime for decreasing optical energy. Compare to experimentally obtained results in Chapter 2, Fig.2.18.

uniform, with a direct relationship between the field profile and the density profile. This is typical of all the Si simulations run. Propagating domains, as in the GaAs simulations, are never seen, although simulations show high-field regions form in Si at the electrodes for tightly focused pump beams, similar to Fig.3.16(b). Impact ionization acts to limit the field in these regions. The e-o images obtained with planar Si switches, reviewed in Chapter 3, are in excellent qualitative agreement with profiles calculated using the experimental parameters.

The e-o measurements of the coaxial Si switch output waveform, discussed in Chapter 2, were compared to calculated waveforms. The comparison is not direct, as the model simulates a switch which is a rectangular solid, not a cylinder as in the experiments. Also, the 1064 nm laser excitation pulse can only penetrate ~1 mm into the cylinder, so there is only a limited region of conduction whose shape is not easily defined. The cylindrical switch is a three-dimensional device, and is only approximated by a one-dimensional analysis. To model the cylindrical switch, a rectangular switch with a volume equivalent to the approximate conducting volume of the Si cylinder was used. Despite the limitations, the model accurately predicts some of the trends observed in the experimental waveforms. Fig.5.13 shows calculated waveforms for a Si switch biased at -10 kV. The degradation of switch rise time and efficiency with decreasing optical energy is seen in this figure. The model will also reproduce the observed voltage overshoot and risetime variation with bias for the appropriate input parameters. Simulation shows that impact ionization plays a significant role in switch behavior at high-bias fields, for the case of focused pump beams. In particular, simulation indicates that the observed increase in the coaxial switch efficiency at -19 kV bias, as opposed to -13 kV bias, is related to the onset of impact ionization in regions of the switch. The field compression induced by

focusing leads to carrier gain by impact ionization. This reduces the final switch resistance at the higher bias, even though the total number of optically generated carriers is the same at either bias voltage.

CHAPTER 5

REFERENCES

[1] K. Meyer, "Study of Picosecond Electron Transport in GaAs Using Transient Photoconductivity and Transient Absorption Spectroscopy," Thesis(Ph.D.)-University of Rochester, Dept. of Physics and Astronomy, (1988).

[2] A.E. Iverson and D. L. Smith, "Mathematical Modeling of Photoconductor Transient Response," *IEEE Trans. Elect. Dev.* **ED-34** (10), 2098 (1987).

[3] A.E. Iverson, D.L. Smith, N.G. Paultier, and R.B. Hammond, "Transient Photoconductive Response of InP:Fe," *J.Appl.Phys.* **61** (1), 234 (1987).

[4] A.E. Iverson, "The Mathematical Modeling of Photoconductive Power Switches," *Trans. Soc. Comp. Simul.* **5** (3), 175 (1988).

[5] M. Weiner, L. Bovino, R. Youmans, and T. Burke, "Modeling of the Optically Conrolled Semiconductor Switch," *Jour. Appl. Phys.* **60** (2), 823 (1986).

[6] W.T. White, C.G. Dease, M.D. Pocha, and G.H. Khanaka, "Modeling GaAs High-Voltage Subnanosecond Photoconductive Switches in One Spatial Dimension," *IEEE Trans. Elect. Dev.* **ED-37** (12), 2532 (1990).

[7] E. Sano and T. Shibata, "Fullwave Analysis of Picosecond Photoconductive Switches," *IEEE Jour. Quant. Elect.* **26** (2), 372 (1990).

[8] S. Selberheer, *Analysis and Simulation of Semiconductor Devices,* (Springer-Verlag, Wien, Austria & New York, New York,1984) Chapter 1.

[9] A.E. Iverson, "The Mathematical Modeling of Time Dependent Photoconductive Phenomena in Semiconductors," Thesis(Ph.D)-University of Arizona, Department of Applied Mathematics, (1987); Los Alamos National Laboratory Report Number LA-11044-T.

[10] S.M. Sze, *Physics of Semiconductor Devices*, 2nd ed., (John Wiley and Sons, New York, 1981) pp.45-49.

[11] K. Horio, T. Ikoma, and H. Yanai, "Computer-Aided Analysis of GaAs n-i-n Structures with a Heavily Compensated Layer," *IEEE Trans. Elect. Dev.* **ED-33** (9), 1242 (1986).

[12] Sze, op. cit., p.325.

[13] Sze, op. cit., p.56.

[14] P.J. Roache, *Computational Fluid Dynamics* , (Hermosa, Albuquerque,New Mexico, 1982) p.20.

[15] Ibid, p.72

[16] Ibid, p.345-349.

[17] W.H. Press, *Numerical Recipes*, (Cambridge University Press, Cambridge, New York, Melbourne, 1986) pp.626-627.

[18] D.L. Scharfetter and H.K. Gummel, "Large-Signal Analysis of a Silicon Read Diode Oscillator," *IEEE Trans. Elect. Dev.* **ED-16** (1), 64 (1969).

[19] Sze, op. cit., pp.850-851.

[20] M. Ohtomo, "Nucleation of High-Field Domains in n-GaAs," *Japan. Jour. Appl. Phys.* **7** (11), 1368 (1968).

[21] J.S. Heeks, "Some Properties of the Moving High-field Domain in Gunn Devices," *IEEE Trans. Elect. Dev.* **ED-13** (1), 68 (1966).

CHAPTER 6

SUMMARY

This research project has made contributions to the field of ultrafast, high-voltage, photoconductive switching, both in the area of experimental diagnostics and fundamental understanding.

The electro-optic probes documented in this dissertation have made possible characterization of high-power switch operation on a picosecond time scale. The electro-optic measurement of the coaxial silicon switch output demonstrated the inadequacies of previous switch models and served as part of an experimental basis for our photoconductive switch model. The two-dimensional electro-optic imaging system can time-resolve the full spatial and temporal variations of the electric field over extended regions above semiconductor surfaces. This was not previously possible. The primary strength of this diagnostic is its ability to monitor events within the electrode gap itself. This is a distinct advantage over monitoring only the semiconductor device output waveform. Operating parameters can be measured with no electrical connection to the device circuit. Electric field profiles obtained with the imaging system have provided new and significant information about the behavior of GaAs photoconductive switches under high bias fields. In particular, some insight into the mechanism for lock-on has been obtained. The formation of high-field domains at the cathode of planar GaAs switches during lock-on has been observed experimentally. This lends credence to lock-on theories that depend on high-field domain formation. Evidence for current channeling, which was unexpected, was

obtained. Imaging of bulk GaAs switch operation showed electric field compression and variation with the applied bias field. The expected, relatively uninteresting, collapse of the electric field in silicon switches was also observed. This system can be used to image the field in other high-field devices, as well, providing a new diagnostic tool for the study of semiconductor devices. Extension of this work to integrated circuits could allow the characterization of devices without introducing connector or stripline effects. Integrated circuits, while low bias devices, require contacts to be closely spaced resulting in high fields between electrodes. Surface field maps of entire LSI circuits could be obtained with the electro-optic imaging system and be used to pinpoint possible breakdown points. Future work could center on improving the spatial resolution and sensitivity of the imaging system. Temporal resolution would be improved by using shorter optical pulses.

The computer-aided analysis of the photoconductive process agreed very well with the experimental data. The one-dimensional model, although simplistic, accurately simulates pulsed-power switching. Simulation data indicates that negative differential resistance is most probably the cause of the non-linear behavior in GaAs. Although lock-on effects are not observed in the simulation data, the computer model can used as an aid in determining the lock-on mechanism. Ionization of traps, for example, could be included in the model and suspect traps could be verified by experiment. Different recombination formulae could also be tried. The program could be modified to be applicable to a wider variety of semiconductor devices by using the appropriate numerical technique to deal with carrier diffusion. Although this was unnecessary for the simulation of high-voltage switches this would allow simulation of low-bias devices.

APPENDIX A

LASER SYSTEM

Ultrafast, high-power optical switching demands a source of clean, high-energy, short laser pulses. Special techniques are required to produce such laser pulses as these requirements are not readily met by commercially available laser systems. This appendix will discuss the custom laser system used in the experiments described in this dissertation. This laser system is based on a Nd:YAG regenerative amplifier seeded by a Nd:YAG oscillator and is shown schematically in Fig.A.1.

I. OSCILLATOR

The oscillator is an in-house built unit based on a commercial cw-pumped Nd:YAG laser head (Quantronix 114). Lasing is at λ = 1064 nm. The oscillator is amplitude-modulated with a commercial acousto-optic mode-locker (Quantronix 302). Approximately 10 W of 50 MHz RF power is supplied to the mode-locker by a specially built driver using a crystal frequency reference. The oscillator output is a 100 MHz train of ~150 ps pulses. The pulse width will vary from 100-300 ps depending on the alignment and operating conditions of the oscillator. The mode-locked output power is ~ 2 W. The average pulse energy is ~20 nJ. The oscillator is mounted on an invar slab for a high degree of length stability. A switchout, consisting of a Pockels cell and two polarizers, selects a single pulse from the 100 MHz oscillator output train at a variable repetition rate up to 2.0 kHz. This switchout protects the oscillator from optical feedback which would otherwise adversely effect the mode-locking stability. The single pulse selected is then amplified in the regenerative amplifier.

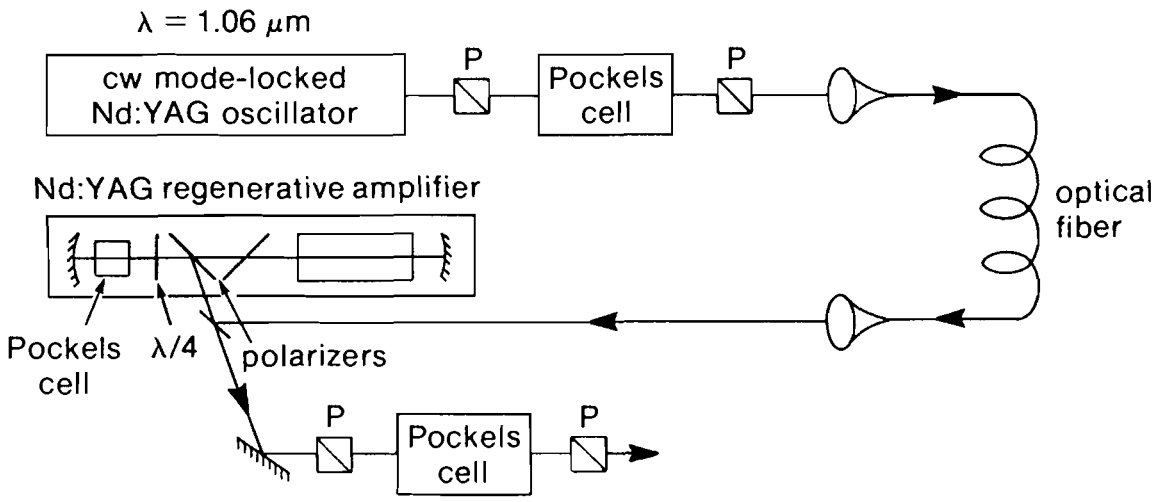

Fig.A.1 Schematic of laser system consisting of Nd:YAG regenerative amplifier seeded by a Nd:YAG oscillator. This set-up is also used without the use of the optical fiber.

II. REGENERATIVE AMPLIFIER

A regenerative amplifier is a solid state optical amplifier capable of producing high gain at kilohertz repetition rates [1]. The pioneering work was done by Lowdermilk and Murray [2,3]. In their scheme, a single laser pulse from a mode-locked Nd:YAG laser was seeded into a pulsed, flash-pumped Nd:YAG regenerative amplifier where the pulse made multiple passes through the laser rod, being amplified, before it was cavity dumped. A significant improvement in the repetition rate of regenerative amplifiers was made at LLE by Duling, *et. al.,* with the demonstration of cw-pumped operation of a Nd:YAG regenerative amplifier [4,5]. A similar system was used in this work, and its operation will now be described.

The oscillator pulse selected by the Pockel's cell switchout is coupled to a single-mode optical fiber and the fiber output coupled to the regenerative amplifier by a glass wedge with ~4 % reflection. The use of optical fiber coupling mechanically isolates the oscillator and amplifier and also decouples their optical alignment. It also allows the two lasers to be on separate tables, or even rooms. The low reflectivity of the glass wedge protects the optical fiber from damage by the amplifier output and couples the amplified pulse out of the amplifier. Alternatively, the amplifier has been seeded directly from the Pockel's cell switchout without the use fiber transport. The injected pulse typically has pJ-nJ energy.

The amplifier resonator cavity and timing sequence are shown in Fig.A.2. The regenerative amplifier operation has four steps: (1) a single pulse from the oscillator pulse train is trapped in the amplifier resonator cavity, (2) simultaneously Q-switching the amplifier resonator, (3) allowing the trapped pulse to undergo N (N > 2) round trips through the amplifier until at saturation, (4) the amplified pulse is cavity dumped [1]. The above four steps are all controlled by the quarter-wave plate and a

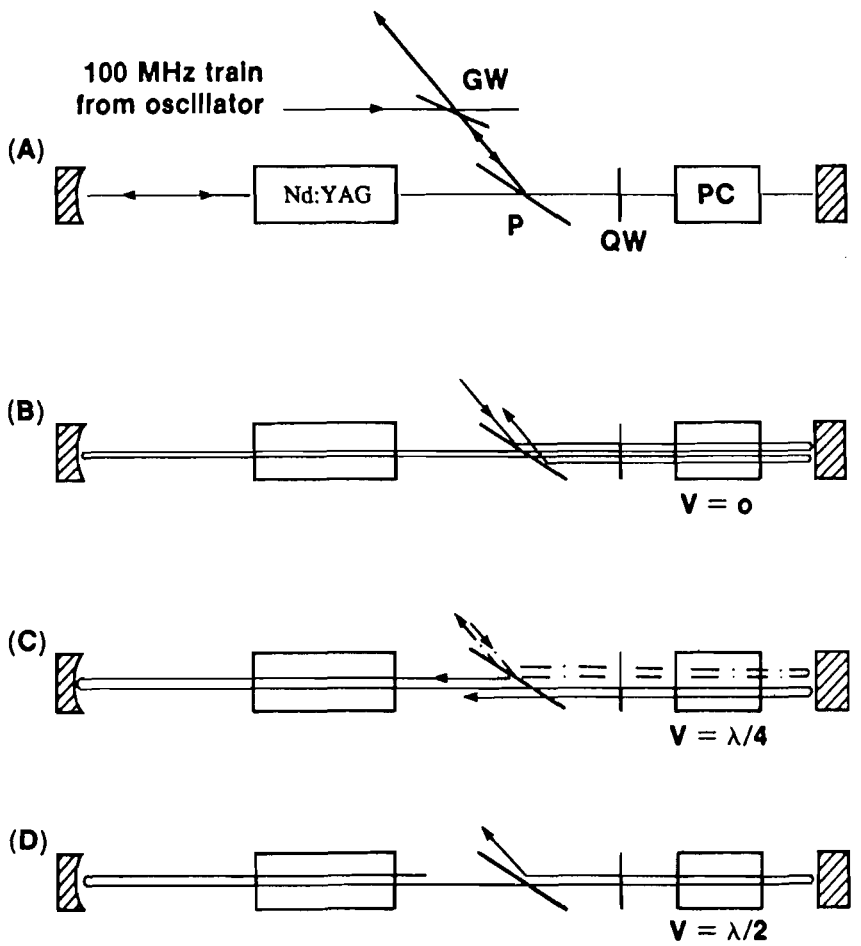

Fig.A.2 Regenerative amplifier timing sequence. (P=polarizer; QW= quarter waveplate; PC=Pockels cell; GW=glass wedge.) a) Regenerative amplifier layout. b) Before injection, the input pulses pass through the laser rod and exits the cavity before extracting any significant energy. c) At injection time, quarter-wave voltage is abruptly applied to the Pockels cell. The one pulse in transit between the Pockels cell and the opposite back mirror is trapped and regeneratively amplified. d) At the peak pulse energy, the Pockels cell is boosted to half-wave voltage and the pulse is cavity dumped. (after ref.[6])

single Pockels cell in the cavity [6]. The injected pulse must be *p*-polarized to enter the cavity. With no voltage applied to the Pockels cell, the quarter-wave plate will rotate the pulse polarization from *p* to *s*, and the pulse will remain in the cavity until a second pass through the quarter-wave plate rotates the the polarization back to *p* and the pulse is then rejected by the polarizer. Negligible energy is extracted from the amplifier in two passes. The quarter-wave plate also frustrates cw lasing. With a quarter-wave voltage applied to the Pockels cell, so that the cell acts as a quarter-wave plate, incoming *p*-polarized injected pulses will be rejected, but a pulse present in the amplifying medium will remain *s*-polarized and be trapped in the amplifier resonator. This quarter-wave voltage also Q-switches the cavity. At the peak of the pulse energy, a second voltage step is applied to the Pockels cell, so that the cell acts as a half-wave plate, and the amplified pulse is rotated back to *p*- polarization and is cavity dumped.

Typical regenerative amplifier pulse trains are shown in Fig.A.3. The typical output pulses from our regenerative amplifier have a pulse energy of 350 μJ at a repetition rate of 1 kHz for an average power of 350 mW. As seen in Fig.A.3.(c), the main amplified pulse is preceded by a series of pre-pulses. The finite extinction ratio of the polarizers, the limited contrast ratio of the internal Pockels cell, and thermal birefringence in the Nd:YAG rod places a limit on the efficiency of the *p*-*s* polarization selection process in the amplifier, allowing some energy to leak out of the cavity resulting in the pre-pulses. The amplifier output is sent through another Pockel's cell switchout to "clean-up" these prepulses. A main pulse to prepulse ratio of up to 10,000:1 is obtained with this switchout.

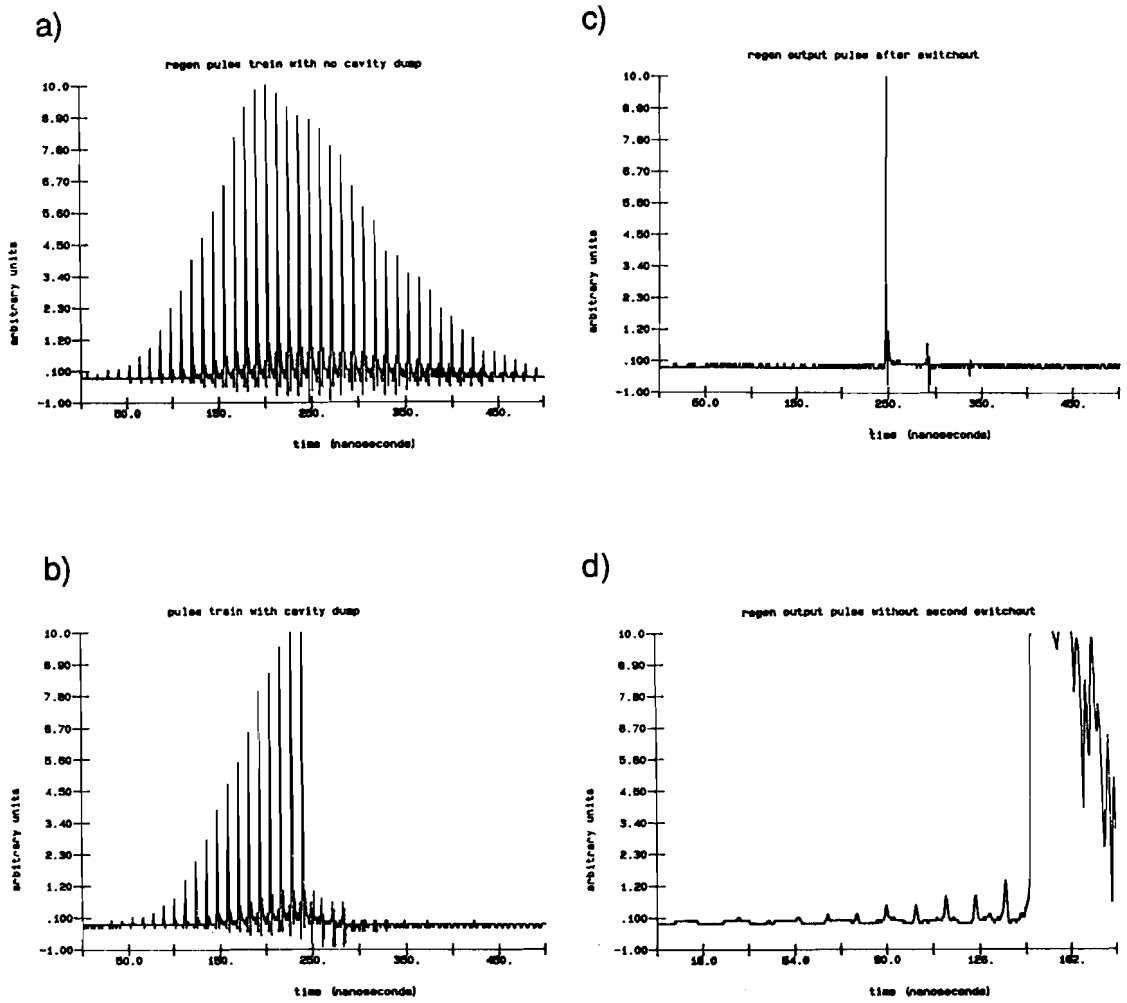

Fig.A.3 Regenerative amplifier pulse pulse trains measured with fast photodiode a) Leakage through end mirror showing pulse buildup inside amplifier cavity. The separation of pulses is the round trip time in the amplifier cavity, 10 ns. The temporal envelope is Q-switch buildup and decay time. b) Same as in a), but with cavity dumping. c) Output pulse after external switchout; d) Amplified pulse before external switchout on expanded scale with prepulses evident. The main pulse is off-scale.

APPENDIX A

REFERENCES

[1] M. Saeed, D. Kim, and L.F. DiMauro, "Optimization and Characterization of a High Repetition Rate, High Intensity Nd:YLF Regenerative Amplifier," *Appl. Optics* **29**(12), 1752 (1990).

[2] W.H. Lowdermilk and J.E. Murray, "Nd:YAG Regenerative Amplifier," *J. Appl. Phys.* **51**, 3548 (1980).

[3] W.H. Lowdermilk and J.E. Murray, "The Multipass Amplifier: Theory and Numerical Analysis," *J. Appl. Phys.* **51**, 2436 (1980).

[4] I.N. Duling III, P. Bado, S. Williamson, G. Mourou, and T. Baer, "A Stable Kilohertz Nd:YAG Regenerative Amplifier," in *Technical Digest, Conference on Lasers and Electro-Optics* (Optical Society of America, Washington, D.C., 1984), paper PD3.

[5] I.N. Duling III, T. Norris, T. Sizer II, P. Bado, and G.A. Mourou, "Kilohertz Synchronous Amplification of 85-femtosecond Optical Pulses," *J.Opt.Soc.Am B* **2**, 616 (1985).

[6] P. Bado, M. Bouvier, and J.S. Coe, "Nd:YLF Mode-Locked Oscillator and Regenerative Amplifier," *Opt.Lett.* **12**, 319 (1987).

[7] P. Bado, and M. Bouvier, "Multikilohertz Pockels Cell Driver," *Rev. of Sci. Instrum.* **56**, 1744 (1985).